UNIVERSITÉ DE MONTRÉAL

FABRICATION AND CHARACTERIZATION OF FIBER OPTICAL COMPONENTS FOR APPLICATION IN GUIDING, SENSING AND MOLDING OF THZ AND MID–IR RADIATION

ANNA MAZHOROVA

DÉPARTEMENT DE GÉNIE PHYSIQUE

ÉCOLE POLYTECHNIQUE DE MONTRÉAL

THÈSE PRÉSENTÉE EN VUE DE L'OBTENTION DU DIPLÔME DE

PHILOSOPHIAE DOCTOR

(GÉNIE PHYSIQUE)

AOÛT 2012

UNIVERSITÉ DE MONTRÉAL

ÉCOLE POLYTECHNIQUE DE MONTRÉAL

Cette thèse intitulée:

FABRICATION AND CHARACTERIZATION OF FIBER OPTICAL COMPONENTS FOR APPLICATION IN GUIDING, SENSING AND MOLDING OF THZ AND MID–IR RADIATION

présentée par: MAZHOROVA Anna

en vue de l'obtention du diplôme de : Philosophiae Doctor

a été dûment acceptée par le jury d'examen constitué de :

Mme BOUDOUX Caroline, Ph.D., présidente

M. SKOROBOGATIY Maksim A., Ph.D., membre et directeur de recherche

M. CALOZ Christophe, Ph.D., membre

M. COOKE David G., Ph.D., membre

DEDICATION

« Le travail éloigne de nous trois grands maux: l'ennui, le vice et le besoin » Voltaire

I'd like to dedicate this thesis to my family and friends, especially…

to Stepan for your faithful love, support, making me laugh when I needed it;

to my friend Andrey for his patience and understanding;

to Dad and Mom for instilling the importance of hard work and higher education;

to grandma, grandpa and my friend Olga for encouragement;

to the families of Francis, Mathieu, Denis and Victoria – may you also be motivated and encouraged to reach your dreams.

ACKNOWLEDGEMENTS

It's amazing to sit and think how many people over the past three years and four months, or around one thousand, two hundred and twenty days to be more precise, have contributed to, or supported my own motivation to complete this PhD, and it's even more difficult to attempt to acknowledge all those who have contributed to this process in other ways over that time, or even before it started. However, I would like to express my heartfelt gratitude to my supervisor and research director Prof. Maksim Skorobogatiy who was abundantly helpful and offered invaluable assistance, support and guidance during my PhD.

During the last two years, I had the pleasure of visiting the Ultrafast Optical Processing Research Group at INRS-EMT, Varennes. It was there where I met prof. Roberto Morandotti and had the chance to work with him and his people. I would like to thank him and his postdocs Marco Peccianti and Matteo Clerici for the help and collaboration with the composite film project.

It was a great pleasure to work with prof. Mohammed Zourob (Biosensors, BioMEMS and Bionanotechnology Research Group at INRS-EMT, Varennes). Thanks to collaboration with him, and his postdocs Andy Ng and Raja Chinnappan, in June 2012 I became award winner of the "Étudiants-chercheurs étoiles" (of the Fonds de Recherche du Quebec Nature et technologies) competition with my paper entitled "Label-free bacteria detection using evanescent mode of a suspended core terahertz fiber".

I have been surrounded by wonderful colleagues Stepan Gorgutsa, Andrey Markov, Bora Ung, Mathieu Rozé, Alexandre Dupuis, Hang Qu. I would like to thank them for the helpful discussions, fiber fabrication and simply mutual support.

Finally I would like to give a special acknowledgement to our ex-technician Francis Boismenu. He offered not only excellent technical assistance when I need it but also much appreciated moral support at any situation.

RÉSUMÉ

Le domaine du térahertz (THz) se réfère aux ondes électromagnétiques dont les fréquences sont comprises entre 0.1 et 10 THz, ou encore pour des longueurs d'onde entre 3 mm et 30 μm. Ce type de radiation, qui se situe entre les ondes radios et la lumière infrarouge, possède des propriétés uniques. Les ondes térahertz peuvent passer à travers diverses substances amorphes, plusieurs matériaux synthétiques et des textiles, mais aussi des diélectriques non polaires tels des matériaux à base de pâtes et papiers, qui sont aussi partiellement transparents aux ondes térahertz. Plusieurs biomolécules, protéines, explosifs ou narcotiques, possèdent aussi des lignes d'absorption caractéristiques (entre 0.1 and 2 THz) tels des « codes barres » permettant de les identifier. Il y a deux avantages principaux à l'utilisation des ondes THz: d'une part elles peuvent pénétrer des matériaux normalement opaques à d'autres fréquences, et d'autre part, et elles permettent une haute sélectivité chimique. Par ailleurs, les ondes THz possèdent une basse énergie (1 THz = 4.1 meV), soit un million de fois plus faible que les rayons X, et ne causent pas d'effets photo-ionisant néfastes aux tissus biologiques. Ceci offre un avantage majeur autant pour l'imagerie de tissus biologiques que dans un contexte médical opérationnel, pour lesquels diverses substances doivent être exposées à la radiation THz. Dans le cadre de cette thèse, j'ai travaillé sur trois sujets de recherche principaux.

Le premier sujet concerne le développement de nouvelles méthodes de fabrication et de caractérisation térahertz de couches minces composites contenant une matrice de microfils alignés en métal (alliage d'étain) ou en verres semi-conducteurs de chalcogénures (As_2Se_3). Les matrices de microfils sont fabriquées par la technique d'empilement-et-étirage de fibres employant de multiples étapes de co-étirage de métaux et verres semi-conducteurs à basse température de fusion, avec les polymères. Les fibres sont ensuite empilées et comprimées ensembles pour former des couches minces en composites (i.e. couches de métamatériaux). La transmission optique à travers ces couches minces de métamatériaux a été effectuée sur toute la plage des térahertz (0.1–20 THz) en combinant les mesures d'un spectromètre infrarouge à transformée de Fourier (FTIR) ainsi qu'un spectromètre térahertz résolu dans le temps (THz-TDS). Les couches de métamatériaux comportant des microfils de métal démontrent de fortes propriétés polarisantes, alors que ceux contenant des microfils semi-conducteurs permettent un large contrôle de l'indice de réfraction tout en étant insensibles à la polarisation incidente. Grâce

au formalisme théorique des matrices de transfert, j'ai démontré une approche permettant d'évaluer l'indice de réfraction complexe des couches de métamatériaux composites. J'ai par la suite développé l'algorithme employé pour extraire les propriétés optiques de l'alliage de métal utilisé dans la fabrication des couches de métamatériaux via l'approximation des milieux effectifs. Finalement, j'ai étudié les obstacles à surmonter dans la fabrication des métamatériaux avec des fils métalliques de dimensions sub-micrométriques, via un processus itératif d'empilement et étirage, en comparant les couches fabriquées après 2, 3 et 4 étirages successifs. Lorsqu'on utilise des alliages de métal on a observé des effets de séparation de phase et la formation de nano-grillages sur les microfils de métal.

La principale difficulté dans le design de guides d'onde térahertz réside dans le fait que pratiquement tous les matériaux connus sont hautement absorbants dans la région du térahertz. Puisque les milieux gazeux sont ceux offrant le moins de résistance à la propagation des ondes THz, une approche efficace pour le design de guides d'ondes est de maximiser la fraction de puissance THz guidée dans les régions gazeuses. Différents types de guides d'ondes THz ont été démontrés sur la base de ce concept. Par exemple, un guide d'onde sous-longueur d'onde comportant un cœur de taille beaucoup plus petit que la longueur d'onde de la lumière, et par conséquent, une large fraction de la puissance THz est guidée en dehors du cœur à hautes pertes.

Un guide d'onde opérant selon ce principe a récemment été démontré par notre groupe de recherche. Ce guide d'onde présente une fibre sous-longueur d'onde suspendue par des ponts étroits au milieu d'un grand tube. Les larges canaux créés par les ponts et le tube forment un système opto-fluidique offrant un accès facile pour l'insertion de substances liquides à analyser ou pour la purge avec des gaz sans humidité. Particulièrement, le guide d'onde THz sous-longueur d'onde employé dans nos expériences comporte un cœur de 150 μm suspendu par trois ponts de 20 μm d'épaisseur au centre d'un tube de 5.1 mm de diamètre et 4 cm de long. Ce type de guide d'onde présente des avantages majeurs pour des applications en biosensing. Premièrement, ce guide d'onde permet un accès direct et facile au cœur de la fibre et au champ évanescent guidé à son pourtour. Deuxièmement, la gaine externe permet d'isoler efficacement le mode guidé par le cœur, de l'environnement extérieur (*e.g.* supports à fibre), prévenant ainsi toute perturbation externe indésirable sur le signal térahertz se propageant dans le cœur.

Pour cette thèse, j'ai démontré pour la première fois un capteur de bactéries *E. coli* basé sur le champ évanescent du mode fondamental d'une fibre à cœur suspendu. Ce dispositif est capable de détecter des bactéries *E. coli* à des concentrations de l'ordre du 10^4-10^9cfu/ml. Le cœur de la fibre est rendu biofonctionnel par l'adsorption de bactériophages T4 qui se fixent aux bactéries cibles pour ensuite les lyser (*i.e.* détruire). À l'aide de microscopie électronique à balayage (MEB) nous avons démontré que les bactéries *E. coli* sont d'abord capturées par les phages et ensuite détruites en des fragments de taille ~1μm qui demeurent fixés sur les parois de la fibre. La fixation des phages aux bactéries et la lyse subséquente sont étroitement corrélées à une forte augmentation de l'absorption des ondes térahertz. Ce signal permet de détecter les bactéries et d'en mesurer la concentration. La technique de détection proposée ne repose pas sur le marquage des bactéries *E. coli* ni sur la signature d'absorption spectrale spécifique à ces bactéries dans le spectre térahertz.

Finalement dans le dernier sujet de recherche de ma thèse, j'ai étudié les performances d'un guide d'onde capillaire à base de verres en chalcogénures permettant une transmission couvrant les spectres de l'infrarouge moyen (IR-m) et du térahertz. Les verres de chalcogénures sont d'un grand intérêt pour des applications potentielles dans les régions de l'infrarouge proche (IR-p) et de l'infrarouge moyen (1−14 μm), et ce en raison des pertes relativement faibles et des non-linéarités optiques élevées. De plus, les fibres optiques microstructurées à base de verres de chalcogénures ouvrent la porte à de nombreuses possibilités pour le développement d'innovations dans le spectre IR-m où les applications émergentes en télédétection, génération de supercontinuum et propagation guidée de lumière IR, et la transmission de radiation laser CO et CO_2, ont été démontrées. Nous proposons ici que l'emploi des verres de chalcogénures représente aussi d'un grand intérêt pour le spectre THz, et ce pour différentes raisons. Plus particulièrement, ces verres offrent un haut indice de réfraction et leur absorption dans le THz présente plusieurs régions de transmission à relativement faibles pertes et haute non-linéarité optique.

En exploitant les propriétés uniques des verres de chalcogénures dans les spectres IR-m et THz, nous prévoyons la possibilité de créer une source de radiation THz cohérente à fibre pompée par une source laser dans l'IR-m. À cet effet, nous montrons que les capillaires en verres de chalcogénures $As_{38}Se_{62}$ peuvent agir en tant que guides d'ondes sur toute la région spectrale de l'infrarouge moyen et du térahertz. Ces capillaires sont fabriqués via une technique à double creuset. Cette approche permet la production de capillaires en verre avec des épaisseurs de l'ordre

de 12 µm à 130 µm. Ces capillaires montrent un guidage à faibles pertes sur toute la plage de l'IR-m et du THz. Nous démontrons expérimentalement que le guidage à faibles pertes avec de minces capillaires implique divers mécanismes physiques dont les réflexions de Fresnel à la parois des capillaires, un guidage anti-résonant (de type "ARROW") causé par l'interférence à l'intérieur des parois des capillaires, en plus du guidage par réflexion totale interne dans lequel les minces parois des capillaires agissent tel un guide d'onde poreux sous-longueur d'onde, ce dernier type de guidage pouvant être observé à de grandes longueur d'ondes dans la région du THz.

ABSTRACT

The terahertz (THz) range refers to electromagnetic waves with frequencies between 100 GHz and 10 THz, or wavelengths between 3 mm and 30 μm. Light between radio waves and infrared has some unique properties. Terahertz waves pass through a variety of amorphous substances, many synthetics and textiles, but also nonpolar dielectric materials, like paper-based materials and cardboard, are transparent to the terahertz waves. Many biomolecules, proteins, explosives or narcotics also have unique characteristic absorption lines, so-called spectral "fingerprints", at frequencies between 0.1 and 2 THz. There are two main advantages of the terahertz radiation: penetration of conventionally opaque materials on the one hand, and their non-ionising nature on the other hand. Particularly, THz waves have low photon energies (1 THz = 4.1 meV), one million times weaker than X-rays, and will not cause harmful photoionization in biological tissues. This has advantages both for imaging biological materials and in operational contexts where different objects have to be exposed to THz radiation. Within the scope of this work I would like to address three main research topics.

In Chapter 2, I describe fabrication method and THz characterization of composite films containing either aligned metallic (tin alloy) microwires or chalcogenide As_2Se_3 microwires. The microwire arrays are made by stack-and-draw fiber fabrication technique using multi-step co-drawing of low-melting-temperature metals or semiconductor glasses together with polymers. Fibers are then stacked together and pressed into composite films. Transmission through metamaterial films is studied in the whole THz range (0.1−20 THz) using a combination of FTIR and TDS. Metal containing metamaterials are found to have strong polarizing properties, while semiconductor containing materials are polarization independent and could have a designable high refractive index. Using the transfer matrix theory, it was shown how to retrieve the complex polarization dependent refractive index of the composite films. We then detail the selfconsistent algorithm for retrieving the optical properties of the metal alloy used in the fabrication of the metamaterial layers by using an effective medium approximation. Finally, we study challenges in fabrication of metamaterials with sub-micrometer metallic wires by repeated stack-and-draw process by comparing samples made using 2, 3 and 4 consecutive drawings. When using metallic alloys we observe phase separation effects and nano-grids formation on small metallic wires.

In Chapter 3, we have studied fabrication and bacteria detection application of the low-loss subwavelength THz microstructured fibers. This is the second research topic discussed in my thesis. In fact, in June 2012 I became one of the award winners of the "Étudiants–chercheurs étoiles" (of the Fonds de Recherche du Quebec Nature et Technologies) competition with my paper entitled "Label-free bacteria detection using evanescent mode of a suspended core terahertz fiber".

One of the key difficulties in the design of terahertz waveguides lies in the fact that almost all materials are highly absorbing in the terahertz region. Since the lowest absorption loss occurs in dry gases, an efficient waveguide design must maximize the fraction of power guided in the gas. Different types of THz waveguides have been proposed based on this concept including a subwavelength waveguide featuring a core with a size much smaller than the wavelength of light in which a large fraction of the guided light is found outside of the lossy core region. A practical design of such a waveguide was recently proposed in our research group and presents a subwavelength fiber suspended on thin bridges in the middle of a larger protective tube. Large channels formed by the bridges and a tube make a convenient opto-microfluidic system that is easy to fill with liquid analytes or purge with dry gases. Particularly, the THz subwavelength waveguide used in our experiments features a 150 μm core fiber suspended by three 20 μm-thick bridges in the center of a 5.1 mm diameter tube of 4 cm in length. This waveguide design presents several important advantages for bio-sensing applications. First, the waveguide structure allows direct and convenient access to the fiber core and to the evanescent wave guided around it. Second, the outer cladding effectively isolates the core-guided mode from the surrounding environment, (*e.g*. fiber holders), thereby preventing the undesirable external perturbations of the terahertz signal.

Next, for the first time an *E. coli* bacteria sensor based on the evanescent field of the fundamental mode of a suspended-core terahertz fiber was proposed. The sensor is capable of *E. coli* detection at concentrations in the range of 10^4–10^9cfu/ml. The fiber core is biofunctionalized with T4 bacteriophages which bind and eventually destroy (lyse) their bacterial target. Using environmental SEM we demonstrate that *E. coli* is first captured by the phages on the fiber surface. After 25 minutes, most of the bacteria is infected by phages and then destroyed with ~1μm-size fragments remaining bound to the fiber surface. The bacteria-binding and

subsequent lysis unambiguously correlate with a strong increase of the fiber absorption. This signal allows the detection and quantification of bacteria concentration. Presented bacteria detection method is label-free and it does not rely on the presence of any bacterial "fingerprint" features in the THz spectrum.

Finally, in Chapter 4, low-loss chalcogenide capillary-based waveguides that operate both in the mid-IR and THz spectral ranges are investigated. Chalcogenide glasses have attracted strong interest in a view of optical applications in the near-IR and mid-IR spectral ranges (1–14 μm) due to their relatively low losses and high nonlinearities. Furthermore, chalcogenide glass-based microstructured fibers open many interesting possibilities for a large number of applications in the mid-IR spectral range, where applications in optical sensing, supercontinuum generation and single-mode propagation of IR light, transmission of the CO and CO_2 laser radiation have already been demonstrated. We believe that chalcogenide glasses can be also of great interest to the THz spectral range for several reasons. Particularly, these glasses offer very high refractive index, and their absorption losses show several regions of relatively low loss and high nonlinearity.

By exploiting the outstanding performance of chalcogenide glasses in the mid-IR and THz spectral ranges one can envision building fiber-based THz light sources with pumping in the mid-IR. We show that chalcogenide glass $As_{38}Se_{62}$ capillaries can act as efficient waveguides in the whole mid-infrared – terahertz spectral range. The capillaries are fabricated using a double crucible drawing technique. This technique allows producing of the glass capillaries with wall thicknesses in the range of 12 μm to 130 μm. Such capillaries show low loss guidance in the whole mid-IR–THz spectral range. We demonstrate experimentally that low loss guidance with thin capillaries involves various guidance mechanisms including Fresnel reflections at the capillary inner walls, resonant guidance (ARROW type) due to light interference in the thin capillary walls, as well as total internal reflection guidance where very thin capillary walls act as a subwavelength waveguide which is especially easy to observe in the THz spectral range.

TABLE OF CONTENTS

LIST OF FIGURES

LIST OF SYMBOLS AND ACRONYMS

$\varepsilon(\omega)$	Permittivity
$\mu(\omega)$	Permeability
ARROW	Antiresonant reflecting optical waveguides
As_2Se_3	Arsenic triselenide
BSA	Bovine serum albumin
cfu	Colony-forming unit
E. coli	Escherichia coli bacteria
FTIR	Fourier transform infrared spectroscopy
FeF_2	Iron(II) fluoride
GHz	Gigahertz
MnF_2	Manganese fluoride
PBS	Phosphate buffered saline
PC	Polycarbonate polymer
pfu	Plaque-forming unit
PMMA	Poly (methyl methacrylate) polymer
PSU	Polysulfone polymer
PP	Polypropylene
SPR	Surface plasmon resonance
SRR	Split-ring resonator
SEM	Scanning electron microscope
THz	Terahertz
THz-TDS	Terahertz Time-Domain Spectroscopy

INTRODUCTION

Invention of the terahertz time-domain spectroscopy (THz–TDS) in the early 1990's opened a new chapter in terahertz science and simultaneously spawned numerous efforts to develop terahertz applications and tools. Terahertz (THz) radiation has big potential for such applications as biomedical sensing, noninvasive imaging and spectroscopy. More recently, much attention has been given to probing explosives and biological samples, which have unique terahertz spectral signatures. And efficient waveguide for THz radiation is a key element for many practical applications. Various designs of such waveguides have been already proposed. However, almost all materials are highly absorbent in the THz region making design of low loss waveguides very challenging. Even air might exhibit high absorption loss if the water vapor content in it is not controlled. In the same time a variety of THz components and devices based on THz metamaterials have been presented, including perfect absorbers, filters, polarizers, THz amplitude and phase modulators and etc. [1-3].

My thesis is dedicated to the fiber optics for guiding and molding of the THz and mid-IR radiation as well as for bio-sensing applications. And for the reader unfamiliar with the principles of THz-TDS, in the Introduction I would like to describe our experimental setup and procedure including basic methods of the THz generation and detection; data acquisition and interpretation; standard methods of the fiber loss characterization.

Terahertz Time-domain Spectroscopy

"Terahertz (THz) fields" is a generic term for waves with a spectrum between 0.1 and 10 THz. To get a better grasp of the frequency region we are referring to it is useful to mention that the frequency of 1 THz corresponds to a wavelength of 300 μm or 0.3 mm and to a wavenumber of 33 cm^{-1}. THz fields have wavelengths extending from 3 mm (0.1 THz or 100 GHz) up to 30 μm (10 THz); this wavelength interval ranges between the top edge of the millimeter wave spectrum to the bottom edge of the optical spectrum corresponding to the boundary of the far-infrared spectral region.

In order to study transmission properties of the developed waveguides, we require a setup that can accurately measure the THz transmission spectrum of the waveguides of different length. While spectroscopy setups are generally designed to measure very thin samples, thus a

conventional setup must be adapted for the samples of variable length. Additionally special care must be taken to insure proper coupling of the THz light into and out of the waveguide. Our THz Time Domain Spectroscopy setup consists of a frequency-doubled femtosecond fiber laser (MenloSystems C−fiber laser) used as a pump source and of two identical GaAs dipole antennae used as an emitter and a detector, respectively, yielding a spectrum ranging from ~0.1 to 3 THz. Contrary to standard THz-TDS setups where the configuration of parabolic mirrors is static, our setup has mirrors mounted on the translation rails, shown at Fig. 1.1. This flexible geometry facilitates mirrors placement, allowing measurement of waveguides up to 45 cm in length without the need of realigning the setup.

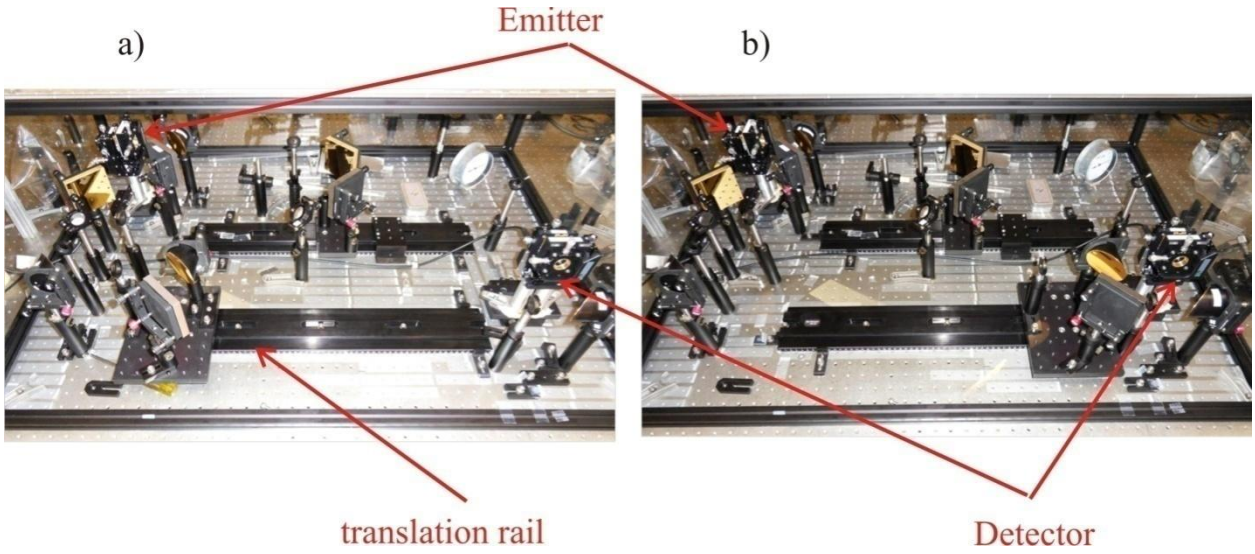

Fig. 1.1. Pictures of the adaptable-path-length THz-TDS setup for measuring the transmission of THz waveguides a) at 0 cm length, in the absence of a waveguide, the mirror assembly is translated to the far left so that the focal points of the input and output parabolic mirrors are in focus; b) at maximum length of 45 cm. In our setup, waveguides up to 50 cm in length can be measured by simply translating the position of these two mirrors along the rail, as illustrated.

A femtosecond laser is used in order to provide synchronization and repeatability between the measurements. This laser produces a train of pulses at a repetition rate around 100 MHz and pulse lengths around 120 fs. The pulse train then is split into two with a beam splitter, with one half utilized in generating the THz signal used to probe the sample and the other half employed in

gating the detector. Because the radiation is coherent, electric field $E(t)$ can be measured directly, instead of just intensity $I(t)$ $\left(I(t) \propto \left| E(t) \right|^2 \right)$

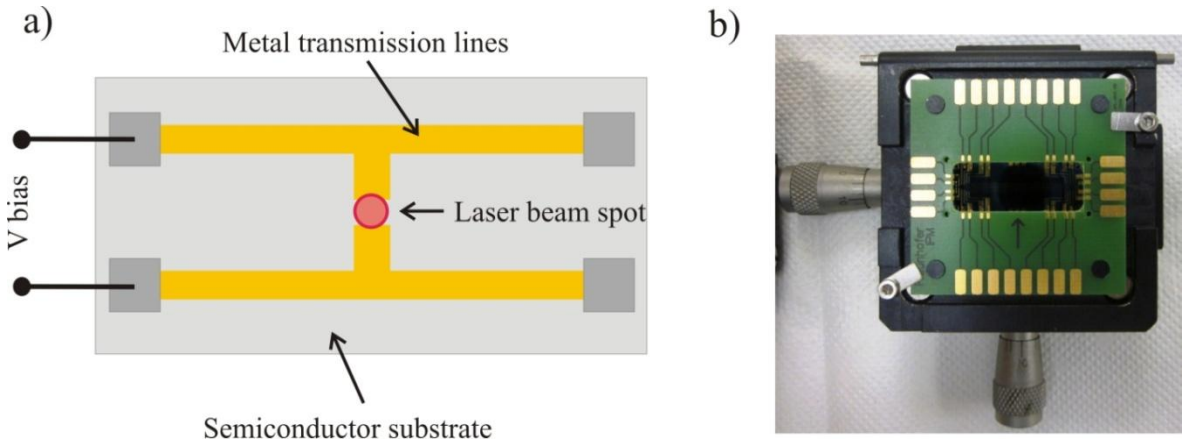

Fig. 1.2. a) The schematic diagram of a THz dipole photoconductive antenna, b) photograph of the chip with six antennas on it. It is based on low temperature-grown GaAs and optimized for the laser source at 780 nm emission wavelength with 120 fs pulse duration (which is used in our setup).

The schematic diagram of a dipole photoconductive antenna is shown at Fig. 1.2. The metal transmission lines are typically deposited on either a semi-insulating GaAs substrate or a low temperature-grown GaAs film on semi-insulating GaAs. The femtosecond laser pulse focused on the biased antenna gap (shown in the diagram) causes photogenerated electrons to rapidly traverse the gap, creating a transient photocurrent that produces a THz electromagnetic pulse. The change in current is extremely rapid so $I(t) \propto \left(\partial J / \partial t \right)$ as given by Maxwell's equations. Emitted THz radiation is then collected by the Silicon lens.

When photoconductive antenna is used as a detector, a time-varying current in the photoconductive antenna is provided by the time-dependent electric field induced by the THz pulse. A part of the excitation laser pulse is delivered to the detector and together with incident THz wave creates photo-electrons. The measured current at the electrodes relative to the timing of the laser pulse reproduces the THz waveform in the time domain (schematic is shown at Fig. 1.3).

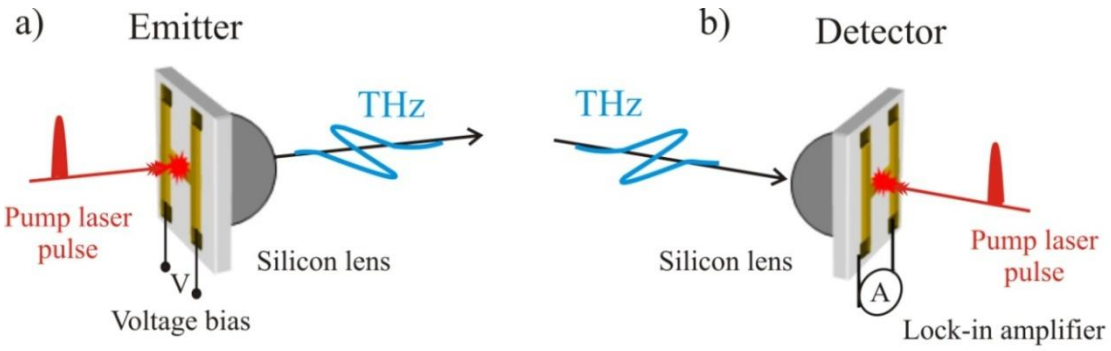

Fig. 1.3. a) Photoconductive antenna acting in the THz generation regime: photocarriers are accelerated by the voltage bias. b) Photoconductive antenna acting as a THz detector: photocurrent is proportional to $E_{THz}(t)$.

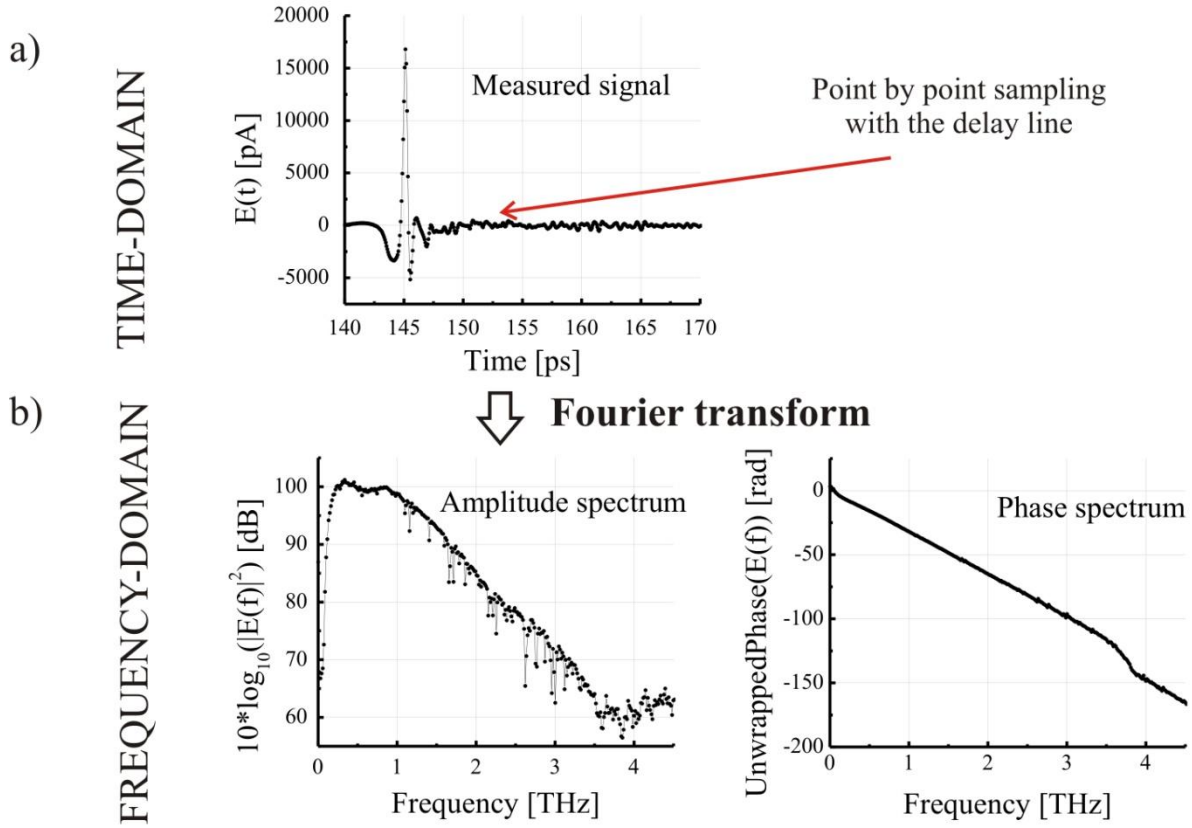

Fig. 1.4. The THz electric field is measured point-by-point in the time-domain ($E_{THz}(t)$) using a THz detector (photoconductive antenna). b) The Fourier transform of the time signal gives an amplitude ($|E_{THz}(f)|$) and phase ($phase(E_{THz}(f))$) information. Presence of water vapor absorption peaks in the amplitude spectrum could be observed.

All of the above can be summarized as follows. At the emitter, the optical pump beam stimulates THz pulsed radiation via charge transport. The diverging THz beam is collimated and focuses onto the sample by a Silicon lens and a pair of parabolic mirrors. After passing through the sample, the THz beam is re-collimated and focused onto the detector by an identical set of lenses and mirrors. At the detector, the initially divided probe beam optically gates the THz receiver with a short time duration compared with the arriving THz pulse duration. Synchronizing between the optical gating pulse and the THz pulse allows the coherent detection of the THz signal at a time instance. A complete temporal scan of the THz signal is enabled by the discrete micro-motion of a mechanical stage controlling the optical delay line.

THz-Time domain Spectroscopy setup is capable to provide both amplitude and phase information. Amplitude of the typical pulse ($E_{THz}(t)$) generated by a pulsed broadband THz source is achieved through by point by point sampling of the electric field with a time resolved measurements and is illustrated in Fig. 1.4 a). In general during the transmission measurements amplitude yields information about the absorption of the sample whereas the phase gives information about its refractive index see Fig. 1.4 b).

Basic data analysis in THz spectroscopy

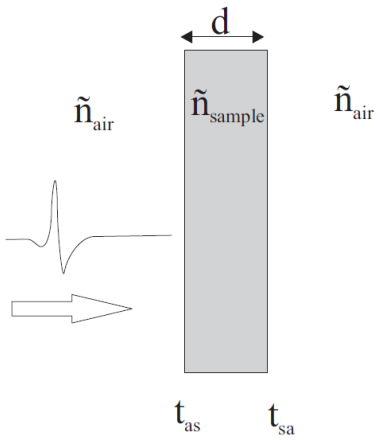

Fig. 1.5. Basic scheme of a THz-TDS transmission experiment: sample under study is a parallel plate with thickness d and complex refractive index $\tilde{n}$.

In a THz-TDS experiment one measures a signal that is proportional to the electric field of the THz pulse $E(t)$. To get the frequency information, a Fourier transform is applied:

$$E(\omega)=\frac{1}{2\pi}\int_{-\infty}^{+\infty}e^{-i\omega t}E(t)dt\,, \tag{1.1}$$

Let us consider a typical spectroscopic experiment: usually two signals are measured, one for the pulse propagating through the sample and one as a reference pulse (E_{sam}, E_{ref}). From these data it is possible to extract information about the dielectric constant of the sample, usually absorption coefficient α , and the real part of the refractive index n_{real}.

In the transmission spectroscopy, the sample is properly prepared with smooth surfaces and a well defined thickness. To analyze the data correctly, several assumptions about the geometry of the spectroscopic setup have to be made. First, when the THz pulse goes through the sample it undergoes reflections at the sample interfaces and gains a phase shift P_{sam} . In the simplest case we consider only reflection and transmission at the first and the second interfaces. If we assume normal incidence and planar surfaces without scattering, we can use the well known expressions for the Fresnel equations. Further, we assume that the medium surrounding the sample is the dry air so we can set its complex refractive index equal to 1. Thus for the signal transmitted through the sample we obtain:

$$E_{sam}(\omega)=E_0(\omega)\cdot t_{as}(\omega)\cdot P_{sam}(\omega,d)\cdot t_{sa}(\omega) \tag{1.2}$$

with

$$t_{as}=\frac{2}{1+\tilde{n}(\omega)}\,, \tag{1.3}$$

$$t_{sa}=\frac{2\tilde{n}(\omega)}{1+\tilde{n}(\omega)}\,, \tag{1.4}$$

where $\tilde{n}=n_{real}+in_{im}$ denotes the complex refractive index of the sample and d is the sample thickness. The phase shift accumulated by the pulse while crossing the sample is described by:

$$P_{sam}(\omega,d)=\exp\left(-i\frac{\tilde{n}\omega d}{c}\right), \tag{1.5}$$

For the reference pulse we have no reflections at the interfaces, only the phase shift accumulated during the propagation at distance d through the air:

$$E_{ref}(\omega) = E_0(\omega) \cdot P_{ref}(\omega, d) = E_0 \exp\left(-\frac{i\omega d}{c}\right), \tag{1.6}$$

If we make the quotient of $E_{sam}(\omega)$ and $E_{ref}(\omega)$ we get:

$$H(\omega) = \frac{E_{sam}}{E_{ref}} = \frac{4\tilde{n}(\omega)}{\left(\tilde{n}(\omega)+1\right)^2} \exp\left(-i\frac{\omega d}{c}\left(\tilde{n}-1\right)\right), \tag{1.7}$$

This quantity is also called transfer function $H(\omega)$ of the system

We are interested in the absorption coefficient $\alpha = 2n_{im} \cdot \omega / c$ and the real part of the refractive index n_{real}. Quantities available from the experiment are $E_{sam}(\omega)$ and $E_{ref}(\omega)$. So we have to solve Equation (1.7) for n_{real} and n_{im}. The ratio of the Fourier transforms is a complex number that we write as:

$$\frac{E_{sam}(\omega)}{E_{ref}(\omega)} = R(\omega) \cdot \exp\left(i\varphi(\omega)\right), \tag{1.8}$$

At this point we have to introduce a further assumption to make an Equation (1.7) analytically solvable. For the calculation of the t-factors (Eq. 1.3, Eq. 1.4) we assume that the material has no absorption, *i.e.* $\tilde{n} = n_{real}$, Equation (1.7) then simplifies to:

$$\frac{E_{sam}(\omega)}{E_{ref}(\omega)} = R(\omega) \cdot \exp\left(i\varphi(\omega)\right) = \frac{4n_{real}(\omega)}{(n_{real}(\omega)+1)^2} \exp\left(-i\frac{\omega d}{c}\left(n_{real}-1\right)\right) \exp\left(-\frac{1}{2}\alpha d\right). \tag{1.9}$$

Solving Equation (1.9) for n_{real} and α we get:

$$n_{real}(\omega) = 1 + \frac{c \cdot \varphi(\omega)}{\omega \cdot d}, \tag{1.10}$$

$$\alpha = \frac{2n_{im} \cdot \omega}{c} = \frac{2}{d} \ln\left(\frac{\left(n_{real}(\omega)+1\right)^2 \cdot R}{4n_{real}(\omega)}\right), \tag{1.11}$$

In THz-TDS, we are also interested in measuring $\varepsilon(\omega) = \varepsilon'(\omega) - i\varepsilon''(\omega)$, *i.e.* the real and imaginary part of the permittivity. Hence, the real and the imaginary parts of the dielectric constant are determined from the following equations:

$$\varepsilon'(\omega) = \left(n(\omega)\right)^2 - \left(\frac{c \cdot \alpha(\omega)}{2\omega}\right)^2, \tag{1.12}$$

$$\varepsilon''(\omega) = \frac{c \cdot n(\omega) \cdot \alpha(\omega)}{\omega}, \tag{1.13}$$

Cutback method

A standard technique for measuring the fiber transmission loss is the cutback method [4]. Within this method a direct power transmission through the fibers of different lengths is measured. The input end of the fiber under test remains fixed during the procedure, and all the cuts are performed at the fiber output end. By plotting the transmission intensity versus the fiber length on a log-log plot, one can extract the fiber loss coefficient. The main advantage of this procedure is that it eliminates the need to estimate the input coupling efficiency into the waveguide. While being a very powerful method for measuring losses in telecommunication fibers, the standard cutback method must be modified to be applicable in the case of the short fibers exhibiting high losses.

Assuming single mode propagation, the equation governing the input and output electric fields of the fiber can be written in the frequency domain as:

$$E_{out}(\omega) = E_{ref}(\omega) \cdot T_1 \cdot T_2 \cdot C^2 \exp\left(\frac{-\alpha_{eff} L}{2}\right) \exp\left(-i\beta_{eff} L\right), \tag{1.14}$$

where, $E_{out}(\omega)$ and $E_{ref}(\omega)$ are the complex electric fields at angular frequency ω on the entrance and exit ends of the fiber, respectively; T_1 and T_2 are the total transmission coefficients that take into account the reflections at the entrance and exit faces, respectively; C is the coupling coefficient, which is the same for the entrance and exit faces; β_{eff} is the propagation constant of the fundamental mode; α_{eff} is the effective material loss that the propagating mode experiences; and L is the fiber length.

At least two different lengths of the fiber are required for calculating its THz properties (α_{eff} and β_{eff}). Applying Equation (1. 14) to two different lengths (L_1 and L_2), the transfer function can be determined from the ratio of $E_{out1}(\omega)$ and $E_{out2}(\omega)$ which reads:

$$\frac{E_{out\,1}(\omega)}{E_{out\,2}(\omega)} = \exp\left(\frac{-\alpha_{eff}(L_1 - L_2)}{2}\right)\exp\left(-\beta_{eff}(L_1 - L_2)\right), \tag{1.15}$$

The C, T_1 and T_2 coefficients are cancelled, because the positions of the fiber and antenna do not change during the cut back measurement. Then α_{eff} and β_{eff} of the fiber are obtained from the amplitude and the phase of the transfer function. However, the cutback technique is a destructive method and is prone to errors due to variations in the cleave quality and realignment of the fiber output end.

SCIENTIFIC OUTCOMES OF MY DOCTORAL RESEARCH

Journal papers:

1. **A. Mazhorova**, A. Markov, B. Ung, M. Rozé, S. Gorgutsa, and M. Skorobogatiy, "Thin chalcogenide capillaries as efficient waveguides from mid-IR to THz," *J. Opt. Soc. Am. B* **29**, 2116-2123 (2012). http://www.opticsinfobase.org/josab/abstract.cfm?URI=josab-29-8-2116
2. **A. Mazhorova**, A. Markov, A. Ng, R. Chinnappan, O. Skorobogata, M. Zourob, and M. Skorobogatiy, "Label-free bacteria detection using evanescent mode of a suspended core terahertz fiber," *Opt. Express* **20**, 5344-5355 (2012). http://www.opticsinfobase.org/oe/abstract.cfm?URI=oe-20-5-5344
3. **A. Mazhorova**, J.-F. Gu, A. Dupuis, M. Peccianti, T. Ozaki, R. Morandotti, H. Minamide, M. Tang, Y. Wang, H. Ito, M. Skorobogatiy, "Composite THz materials using aligned metallic and semiconductor microwires, experiments and interpretation", *Opt. Express* **18**, 24632-24647 (2010). http://www.opticsinfobase.org/oe/abstract.cfm?URI=oe-18-24-24632
4. B. Ung, **A. Mazhorova**, A. Dupuis, M. Rozé, and M. Skorobogatiy, "Polymer microstructured optical fibers for terahertz wave guiding," *Opt. Express* **19**, 848-861 (2011). http://www.opticsinfobase.org/oe/abstract.cfm?URI=oe-19-26-B848
5. December issue OPN:
   B. Ung, M. Rozé, **A. Mazhorova**, M. Walther and M. Skorobogatiy, "Suspended Core Subwavelength Plastic Fibers for THz Guidance," *Optics Photonics News*, special December issue that highlights the most exciting peer-reviewed optics research to have emerged over the past 12 months, 41 (2011).
6. One of the Top 10 downloaded *Optics Express* articles in May 2011:
   M. Roze, B. Ung, **A. Mazhorova**, M. Walther, M. Skorobogatiy, "Suspended core subwavelength fibers: towards practical designs for low-loss terahertz guidance," *Opt. Express* **19**, 9127-9138 (2011). http://www.opticsinfobase.org/oe/abstract.cfm?URI=oe-19-10-9127
7. A. Dupuis, **A. Mazhorova**, F. Désévédavy, M. Rozé, and M. Skorobogatiy, "Spectral characterization of porous dielectric subwavelength THz fibers fabricated using a

microstructured molding technique," *Opt. Express* **18**, 13813-13828 (2010). http://www.opticsinfobase.org/oe/abstract.cfm?URI=oe-18-13-13813

Conference proceedings:

1. **A. Mazhorova,** A. Markov, B. Ung, M. Rozé, S. Gorgutsa, and M. Skorobogatiy "THz wave guiding using hollow capillaries", *Photonics North*, June 6-8 (2012)
2. **A. Mazhorova**, A. Markov, A. Ng, R. Chinnappan, M. Zourob, and M. Skorobogatiy, "Label-free bacteria detection using evanescent mode of a suspended core terahertz fiber," in *CLEO: Science and Innovations*, OSA Technical Digest (online) (Optical Society of America, 2012), paper CTu3B.6.
3. **A. Mazhorova**, M. Zourob, and M. Skorobogatiy, "Suspended core polyethylene fiber for bio-sensing applications in the terahertz region," in *Optical Sensors, OSA* Technical Digest (CD) (Optical Society of America, 2011), paper STuC3.
4. Invited Talk: M. Skorobogatiy, B. Ung, **A. Mazhorova**, M. Rozé, A. Dupuis, "Plastic fibers for terahertz wave guiding," *ECOC* 2011, Tu.6.LeCervin.1, Geneva, Switzerland, September 18-22, 2011.
5. B. Ung, M. Rozé, **A. Mazhorova**, M. Walther, and M. Skorobogatiy, "Suspended core subwavelength fibers for practical low-loss terahertz guidance," in *Optical Sensors*, OSA Technical Digest (CD) (Optical Society of America, 2011), paper STuC2.
6. **A. Mazhorova**, J.F. Gu, S. Gorgutsa, M. Peccianti, T. Ozaki, R. Morandotti, M. Tang, H. Minamide, H. Ito, M. Skorobogatiy, "THz metamaterials using aligned metallic or semiconductor nanowires," We-P.31, *Proceedings of IEEE34th International Conference on Infrared, Millimeter, and Terahertz Waves*, IRMMW-THz 2010
7. A. Dupuis, **A. Mazhorova**, F. Desevedavy, M. Skorobogatiy, "Loss and Spectral Measurements of Porous and Non-Porous Subwavelength THz Fibers," JWA117, *CLEO* (2010)

Award

June 2012 award winner of the "Étudiants–chercheurs étoiles" (Fonds de Recherche du Quebec, Nature et Technologies) competition with paper entitled "Label-free bacteria detection using evanescent mode of a suspended core terahertz fiber".

CHAPTER 1
MOTIVATION AND OBJECTIVES OF MY RESEARCH

1.1 Motivation and objectives of my research

The THz spectral range is extremely promising for a large number of possible applications, and is one of the less explored and exploited region of the electromagnetic spectrum, referring to electromagnetic waves with frequencies between 100 GHz and 10 THz, or wavelengths between 3 mm and 30 μm, *i.e.* in the gap between the realms of electronics and photonics. Much of the motivation to advance THz science and technology could be explained by the unique characteristics of THz radiation.

From the fundamental point of view this is the highest electromagnetic frequency at which the electric field vector and its time dynamics could be measured directly. It allows, for example, determining the complex refractive index of the sample without performing the Kramers-Kronig analysis, which is usually employed for mid-infrared spectroscopy and requires two independent measurements.

At the same time, THz radiation is very beneficial for the practical applications as it is non-ionizing one and most dry materials are transparent to few cm in depth. So that THz pulses have the ability to pass through such materials as clothing, foods and packing. Plus the THz region is also rich with vibrational signatures, enabling chemical sensing of illicit materials such as explosives and narcotics, thus offering a considerable potential for material characterization, biological sensing, security scanning, quality control.

Still there are some challenges that limit real-life implementation of the THz spectroscopy. First of all, THz emission systems are still bulk, as they consist of free-space optics together with a large nitrogen purged cage, that is needed to minimize the effects of absorption from the ambient water vapor (as an example, photograph of our THz-TDS setup is shown in Fig. 1.6). And in general such systems are very inconvenient to work with, especially in applications that require scanning, as the user has to bring the sample into the nitrogen purged cage, or even modify the whole system depending on the requirements (size of the sample, its dimensions). In response to this challenge we propose our solution: *THz fibers designed for flexible delivery of THz light.*

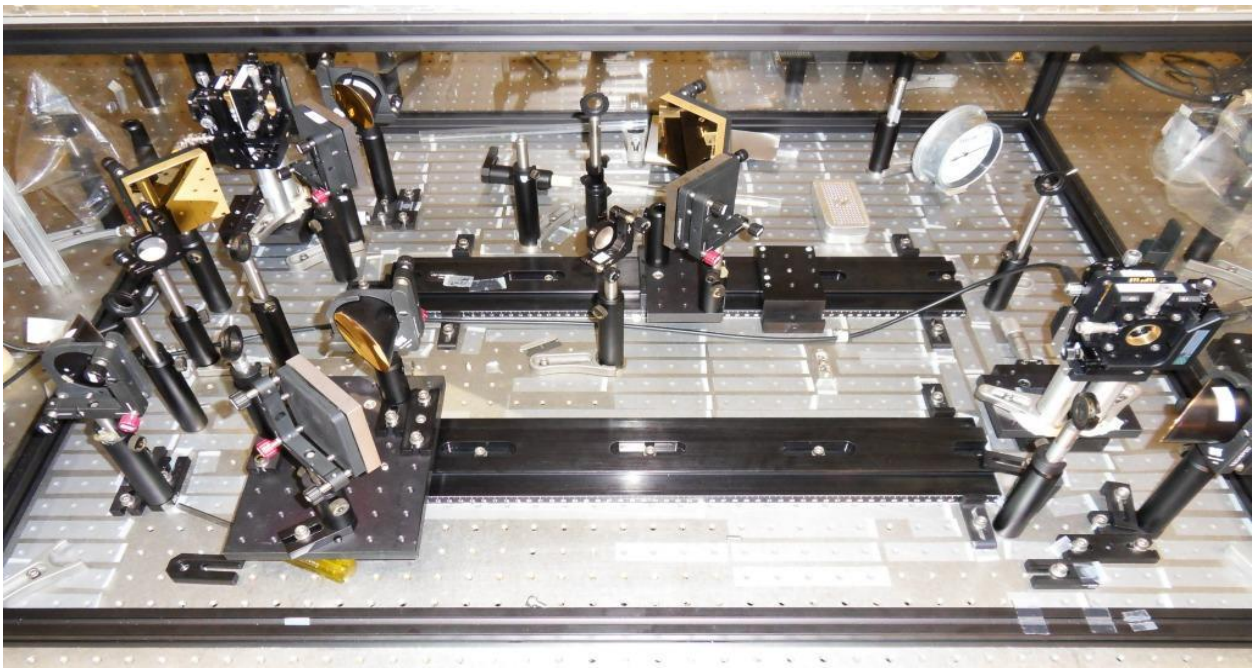

Fig. 1.6. Photograph of the THz Time Domain Spectroscopy setup built in our group.

Second, almost all materials are highly absorbing in the THz spectral range. For example, standard bulk material loss for Polyethylene is 0.2 cm^{-1}, which means that one can transmit only 10% and only up to ~23 cm with a solid core fiber made from Polyethylene. The same is valid for most plastics. Therefore using of solid core fibers is out of the question. Thus, our solution is *development of the hollow and porous core fibers, where THz light is guided mostly in the low-loss gas, filling the waveguide*.

Metamaterials and frequency selective surfaces attract constant significant attention as they allow designing materials with desirable optical properties, such as refractive index and permittivity that can be used for fabrication of the optical components for guiding and molding of the THz and mid-IR radiation, for example, wire-grid polarizers. However fabrication of 3D THz metamaterials is still quite challenging and labor-intense. Present-day fabrication methods typically involve fabrication of 2D metamaterials layers by the means of lithography, these layers are then stacked to the 3D multilayer structures. As a solution we *propose fiber based metal-containing structures*.

At a glance it may look like we deal with several completely different questions. *However the unifying factor is the usage of fiber drawing techniques* to find a fiber-based solution.

1.2 Origins and main project results

I've joined the Complex Photonic Structures and Processes group in 2009. At that time we have already presented subwavelength fiber with a porous core and had already performed theoretical simulations. *My goal was in general not only to be able to fabricate such fibers and improve fabrication techniques, but rather to find possible applications of them.*

Our original theoretical investigations have predicted that addition of an array of subwavelength holes into the crossection of a subwavelength fiber increases the fraction of power guided in the air, thus leading to a lower absorption loss [5-7]. The idea of adding holes into a subwavelength fiber was inspired by the earlier work of Nagel et al. [8]. The authors have demonstrated that addition of a single subwavelength hole into the center of the solid core can result in strong field confinement inside this hole. However, in their case diameter of the waveguide was comparable to the wavelength, and the central hole was very small. In contrast with our waveguide that features much smaller, comparing to the THz wavelength, fiber diameter along with big holes. In our case addition of several holes within the subwavelength fiber reduces the fiber absorption loss by forcing a greater portion of the radiation to guide in the dry low-loss gas filling the porous fiber core. Exploring this approach we were later able to make a waveguide with the subwavelength (150 μm) fiber core suspended on the thin bridges in the middle of large protective tube [9]. Such waveguide design provides several important advantages for bio-sensing applications. First, the waveguide structure allows direct and convenient access to the fiber core and to the evanescent wave guided around it. Second, the outer cladding effectively isolates the core-guided mode from the surrounding environment, (*e.g.* fiber holders), thereby preventing the undesirable external perturbations of the terahertz signal. Overall we have found that described waveguide is very well suited for biosensing applications.

At the same time we started to work on fibers with incorporated metal or semiconductor wires. As it was already mentioned, fabrication of 3D metamaterials is still challenging [10]. 2D metamaterials are typically fabricated by the means of lithography direct writing, or two-photon polymerization however all these techniques are only suitable for relatively small shapes of 1-2 μm [11]. Thus for the fabrication of 3D metamaterials the only choice is 3D printing or stereolithography, still the resolution of this method is about ±20 μm in XY plane and ±50 μm in Z-direction [12]. In our group we had investigated a new approach of co-drawing the metal wires

of low melting temperature alloys together with polymers into microstructured fibers that are then pressed into composite films. A process for the production of fine metal wire directly from the melt was first reported by Taylor in 1924 [13]. In this technique, which is called Taylor-wire or microwire process, the metal to be drawn is contained in a glass tube with the one end closed. Then this end is melted, softened and drawn into glass cladded microwire.

And recently we had an industrial collaboration with fiber manufacturer CorActive Inc. (Québec) within the CRD grant. During this collaboration we have fabricated the As_2Se_3 chalcogenide glass capillaries with different wall thickness in the range from 12 μm to 130 μm by double crucible glass drawing technique. Produced capillaries were extensively studied in the broad spectral range from mid-IR to THz and we found that to act as efficient waveguides.

According to the three main research objectives, during my PhD studies I was mainly working on the three general types of fibers presented above. *Each fiber concept resulted in the practical application as a solution to the currently existing challenges in THz research domain* and is described in details in corresponding section of the current thesis.

1.3 Structure of the thesis

This thesis is organized as follows:

Chapter 2 provides a literature review of the modern metamaterials and their applications in the THz spectral range, including basics of the metamaterial operation principles, description of their fabrication techniques, and characterization of their optical properties. Chapter 2.2 provides a literature review of the different methods for highly sensitive chemical and biological detection in the THz operation range. In Chapter 2.3, I review recent studies of the transmission characteristics of the hollow-core waveguides with resonant dielectric reflectors in the form of capillaries. In what follows we call such waveguides – pipe waveguides.

Chapter 3 represents my first paper "Composite THz materials using aligned metallic and semiconductor microwires, experiments and interpretation" published in *Opt. Express* in 2010. This paper is devoted to the experimental and theoretical work concerning THz composite films and includes detailed description of the fabrication and characterization techniques.

Chapter 4 represents my second paper "Label-free bacteria detection using evanescent mode of a suspended core terahertz fiber," also published in *Opt. Express* in 2012. In this chapter

I present the results on the development of the *E. coli* bacteria sensor based on the evanescent field of the fundamental mode of a suspended-core terahertz fiber.

Chapter 5 represents my third paper "Thin chalcogenide capillaries as efficient waveguides from mid-IR to THz," published in the *J. Opt. Soc. Am. B* in 2012. It is devoted to the investigation of low-loss chalcogenide capillary-based waveguides in mid-IR and THz spectral regions.

Finally, general discussion of the achieved results and future research perspectives are presented.

CHAPTER 2
LITERATURE REVIEW

2.1 Metamaterials in the THz spectral range

Metamaterials or left-handed media (*LH*) materials, where the electric field (*E*), magnetic field (*B*), and wavevector (*k*) form a left-handed coordinate system, were first studied by Russian physicist Veselagoin 1967 [14]. These left-handed materials, which are also called negative index materials, have both negative electrical permittivity (ε) and negative magnetic permeability (μ) inside a common frequency band [15, 16]. Within the definition of metamaterials we also include the so-called single-negative materials (*SNG*) [17], where either ε or μ is negative, which are used for the creation of a super-lenses with thin silver films [18] as well as devices based on controlling the resonances exhibited by sub-wavelength structures.

Metamaterials are a class of artificial materials and typically consist of periodic arrays of metal-dielectric resonant inclusions, which are properly tailored in shape and in size and are embedded within, or on top of, a dielectric substrate [19, 20]. The size and the distance of the individual inclusions in metamaterials are subwavelength. This allows one to describe the optical response of metamaterials by effective material parameters [21-24]. They enable a desired electromagnetic response that is difficult or impossible to obtain from naturally occurring materials. Recently metamaterials were investigated experimentally, starting with Pendry [25], who suggested a design consisting of concentric metallic rings with gaps, called split-ring resonator (SRR), which exhibits $\mu<0$. Although it was well known how to obtain a $\varepsilon<0$ material by using metallic wire arrays [26], the realization of $\mu<0$ response (especially at high frequencies) has been a challenge, due to the absence of naturally occurring magnetic materials with negative μ. However at THz frequencies, it has long been known that antiferromagnets such as FeF_2 or MnF_2 exhibit a resonant magnetic response [27]). The first experimental realization of LH-materials was achieved soon after, by separately constructing $\varepsilon<0$ and $\mu<0$ components, and then by combining them together [28].

Since then, metamaterials have emerged as versatile tools for the implementation of optical components. The main advantage of metamaterials as compared with conventional materials is that by changing the size and shape of the subwavelength constituents, the optical

response of a metamaterial can be easily designed to whichever values are desired for an application.

2.1.1 Effective medium approaches

Propagation of the electromagnetic waves in heterogeneous media like metamaterials can be analyzed using various effective medium approaches [21-24]. Among these approaches, there are three major ones that are used most frequently, including Maxwell-Garnett theory [23], Bruggeman effective medium model [24], and the simple effective medium approximation. All of these theories assume that inclusions (*e.g.* spheres, discs, rods) have been dispersed into a host matrix, that these inclusions are much smaller than the wavelength in the host material ($<0.1-0.2\lambda$), and that the material can, therefore, be treated like an effective dielectric medium. In what follows, we consider composite materials in the form of a parallel wire arrays. The simplest effective medium approach for such a material is the one that uses linear interpolation, and relies on the filling factor $f = S_2/S_1$ which defines the volume fraction of the particles embedded into the matrix, where S_1 is the active area of the matrix and S_2 is the total cross-sectional area of the particles:

$$\varepsilon_{eff}(\omega) = f\varepsilon_i(\omega) + (1-f)\varepsilon_h(\omega), \tag{2.1}$$

in which ε_i is the dielectric constant of the inclusions and ε_h is the dielectric constant of the host material. The constitutive parameters of the base material and inclusions can depend on frequency. Another model that is frequently used is called the Maxwell-Garnett effective medium theory, developed more than 100 years ago. Within this model, electric permittivity is:

$$\left(\frac{\varepsilon_{eff}(\omega)-\varepsilon_h(\omega)}{\varepsilon_{eff}(\omega)+k\varepsilon_h(\omega)}\right) - f\left(\frac{\varepsilon_i(\omega)-\varepsilon_h(\omega)}{\varepsilon_i(\omega)+k\varepsilon_h(\omega)}\right) = 0 \tag{2.2}$$

This typical approximation holds at low values of the filling factor $f < 0.05-0.15$. For higher values of the filling factor, the theory developed by Bruggeman must be used to achieve an accurate determination of the effective dielectric constant. In this case, this effective electric permittivity is given by:

$$f\left(\frac{\varepsilon_i(\omega)-\varepsilon_{eff}(\omega)}{\varepsilon_i(\omega)+k\varepsilon_{eff}(\omega)}\right)+(1-f)\left(\frac{\varepsilon_h(\omega)-\varepsilon_{eff}(\omega)}{\varepsilon_h(\omega)+k\varepsilon_{eff}(\omega)}\right)=0, \tag{2.3}$$

where k is a screening parameter. The value for k is 1 if the inclusions are an array of cylinders with their axes collinear with the incident radiation and the value for k is 2 if they are spherical particles. Parameter k is determined by the shape and orientation of the inclusions with respect to the external electric field. Screening parameter is directly related to the Lorentz depolarization factor L as:

$$k=\frac{1}{L}-1 \tag{2.4}$$

Formulas for calculating depolarization factors of ellipsoids and the table of depolarization factors for canonical spheroids (*i.e.* spheres, disks, and cylinders) can be found in papers [29, 30]. Effective medium theory models allow that within the same composite material, particles can have different depolarization factors. However, in reality it is almost impossible to have perfect ellipsoidal or spherical particles, so, for any arbitrary shape a reasonable approximation is needed. If the inclusions are thin rods (cylinders), two of their depolarization factors are close to $L\sim 1/2$, and the third depolarization factor can be calculated as $L\sim(1/b)^2\ln(b)$ [31]. Where, $b=l/d$ is the aspect ratio of an inclusion of length l and diameter d. The sum of all three depolarization factors is always unity.

2.1.2 Wire grid theory

One of the simplest example of metamaterials is metal-dielectric composite called "wire array medium" as shown in Fig. 2.1. It consists of thin metallic wires embedded into a dielectric matrix or suspended in vacuum. For the polarization of incident field with electric field parallel to the wires (along X axis at Fig. 2.1), the effective permittivity of such a composite in the Maxwell-Garnett approach is then given by:

$$\varepsilon_{eff}(\omega)=\varepsilon_h\left(\frac{\varepsilon_h(1-f)+\varepsilon_i(1+f)}{\varepsilon_i(1-f)+\varepsilon_h(1+f)}\right) \tag{2.5}$$

The value for k is taken as 1 because the inclusions are an array of cylinders, whose axes are collinear with the direction of electric field of the incident radiation, f is a filling factor. The

medium in this case behaves in a similar manner as the surface of a metal sheet. Since electrons are free to move along the wires, the incident field induces electric currents in the wires (like the microwave dipole receiver antenna) and medium reflects light, with some energy lost due to Joule heating of the wires. For wire grids made of good conductors, absorption is usually negligible.

For electromagnetic waves with electric fields perpendicular to the wires (electric field along Y axis in Fig. 2.1), the flow of the electric current is limited by the width of the wire; therefore, for deeply subwavelength-size wires, little energy is lost or reflected, and the incident wave is able to travel through the wire array, thus, resulting in a considerable transmission of the incident wave. In this respect, the wire grid behaves as a dielectric rather than a metal sheet. For perpendicular polarization, the effective electric permittivity of the wire array is described by simple effective medium approximation:

$$\varepsilon_{eff}(\omega) = f\,\varepsilon_i(\omega) + (1-f)\,\varepsilon_h(\omega) \tag{2.6}$$

From the presented arguments it follows that polarization sensitivity of the wire arrays (wire grid polarizers) is due to widely different effective permittivities for the electric field components along the wires and perpendicular to them.

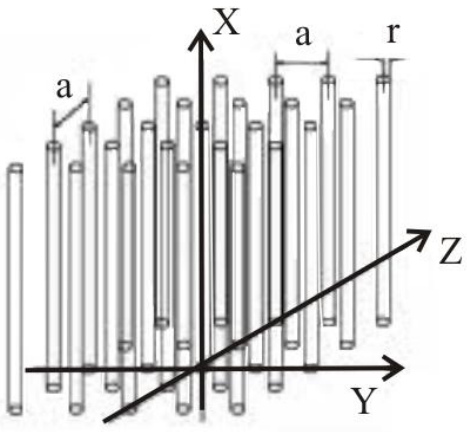

Fig. 2.1 Wire array medium

An alternative interpretation for the operational principle of the wire grid polarisers is in terms of the effective plasma frequency of a metamaterial. This was proposed by Pendry et al [32] to explain wave propagation through a 2D array of wires. He demonstrated that

such an array behaves like a Drude metal with effective plasma frequency which is only a function of the geometrical parameters of a wire array:

$$\omega_p^2 = \frac{2\pi c_0^2}{a^2 \ln(2a/d)} \tag{2.7}$$

where c_0 – the vacuum light speed, a – is the spacing between wires and wire diameter d. Several more complicated but precise derivations of the effective plasma frequency for the wire medium have been developed [33] and a comparison between the models has been conducted [34]. Since the effective plasma frequency in a wire medium can be tuned by adjusting the medium's geometrical parameters, the spectral region for the desired permittivity values can be engineered to occur at practically any frequency.

2.1.3 Metamaterials for THz optical components

Metamaterials play a potentially important role in creating necessary functional devices for THz applications. A variety of THz components/devices based on THz metamaterials have been presented [1-3]. This includes perfect absorbers [35], filters [36], polarizers [37, 38], THz amplitude and phase modulators [39]. In this section, I present a brief review of some recent progress regarding novel THz metamaterial devices for manipulating THz radiation.

Polarization optics

Many metamaterials have a polarization-sensitive response because of the symmetry properties of their constituent elements. This renders them good candidates for construction of efficient terahertz polarization optics such as polarizers and wave plates.

Probably the best-known metamaterial component for polarization control of terahertz waves is the wire-grid polarizer, which provides broadband behavior, low loss and a high extinction ratio [40, 41]. Currently, a host of wire-grid structures composed of uniformly spaced metal wires are employed as polarizers and filters for THz applications. Although these exhibit high extinction coefficients at THz wavelengths, they have drawbacks of fragility and high cost. Conventional THz polarizers are made by mechanically winding thin metallic strings, such as tungsten wires, on rigid frames under physical tension. Such widely used and commercially available THz polarizers are typically free-standing, with function efficiencies highly reliant on

wire spacing constants. Nowadays there are also THz polarizers in the form of micrometer-pitch metal grating on a Si substrate fabricated by photolithography and wet etching. This method allows to create uniform pitch and hereby to increase extinction ratio [42].

Liquid-crystal polarizers are also widely used. They have a high extinction ratio; however, their working frequency range is limited between 0.2 and 1.0 THz [43]. Birefringent negative-index metamaterial was proposed as phase retarder. However, owing to the intrinsic resonant properties of metamaterial, the absorption of energy was severe and the working frequency band was narrow [44, 45]. Also, birefringence from electric resonance of metamaterial, as well as scaled double-layer meanderline structure, were used to fabricate terahertz quarter-wave plate working in narrow bandwidth [46, 47]. Combining six quartz plates together, a quarter-waveplate operating from 0.25 to 1.75 THz was designed and fabricated [48]. However, with the bulk thickness of 31.4 mm, the device was not compact. In the study of generation of elliptically polarized terahertz pulses, Amer [49] proposed a rough "quarter-wave plate" by simply assembling a wire-grid polarizer with a metal mirror, whereas the achromaticity was not achieved.

THz absorbers

Metamaterial-based absorbers can be conceived which exhibit a terahertz reflectance of almost zero in a certain frequency range. The basic idea in the design of a metamaterial absorber is to minimize the reflection through impedance matching, and minimize the transmission by maximizing the absorption, which are determined by the permittivity $\varepsilon(\omega)$ and permeability $\mu(\omega)$ of the designed structure [50]. After a first theoretical investigation by Landy et al in 2008 [51], the first metamaterial-based terahertz absorber was fabricated and experimentally characterized in 2008 by Tao et al. [52]. The metamaterial consisted of two metallic layers separated by a polyimide spacer layer. The top layer comprised an array of electric resonators, while the bottom layer employed cut wires. With this design, a maximum absorption of 70% was measured at a frequency of 1.3 THz. In the same year, this design was significantly improved by exchanging the layer of cut wires with a continuous metal sheet [53]. In 2012 metamaterial absorbers with nearly 100% absorption have been designed and fabricated using a periodic array of aluminum (Al) squares and an Al ground plane separated by a thin silicon dioxide (SiO_2)

dielectric film [54]. The entire structure is less than 1.6 mm thick. Films with different dielectric layer thicknesses exhibited resonant absorption at 4.1, 4.2, and 4.5 THz with strengths of 98%, 95%, and 88%, respectively.

THz filters

Functionality of most metamaterials is explained by the resonances of their constituent elements. Therefore transmission and reflection characteristics of the metamaterials generally exhibit strong frequency dependence. Hence, it is not surprising that wavelength-filtering devices were among the first metamaterial optical components for terahertz radiation. Metamaterial-based filters are very versatile because it is easy to adapt their designs to a desired operating frequency range by simple scaling of their geometric structure.

Terahertz filters consisting of thin structured/perforated metal sheets have been well-known. Among the earliest reported designs are single- or multi-layer wire arrays and their complements [55] and arrays of metallic crosses or cross-shaped holes [56]. Until today, numerous THz filter designs have been proposed using variations of these early concepts. These include photonic band gap filters constructed from metallic meshes [57], arrays of holes of different shapes in metallic sheets [58], and a closely-spaced composite of a metallic mesh/ wire arrays and a complementary mesh [59]. Technologically different approach for THz filters, microfabricated pillar arrays have been demonstrated [60] with a low-pass behavior in reflection and a high-pass characteristic in their transmission spectrum.

2.1.4 Fabrication methods

Owing to the relatively large wavelengths of terahertz radiation (λ = 300 μm at1 THz), terahertz metamaterials can be easily fabricated with standard microfabrication techniques such as UV lithography [61], with the smallest feature size typically in the order of few micrometers. Lithographic or direct-laser writing techniques are versatile, however, their biggest disadvantage is in a fairly slow processing time, which results in the 2-4 hours per square millimetre sample production rate.

Recent technological advances allow metamaterials via super-fine ink-jet (SIJ) printing technology to be produced [37, 38, 40]. A silver film is fabricated using an SIJ printer with silver

paste ink, allowing simple THz metamaterials such as metal wire-grid structures and split-ring resonators to be printed on high-resistivity silicon substrates. The main limitation of such a fabrication process remains the limited resolution of the printer head, which is difficult to reduce below ~10 microns.

Fiber drawing technique

The idea of an alternative technique suitable for the mass-production of metamaterials was taken from the fabrication principle of photonic crystal fibers. Particularly, fabrication of metamaterials employs co-drawing of the low-melting-temperature metal wires in a polymer matrix [13, 62, 63]. During drawing process, the cross-section of the preform can be preserved so that the array of relatively thick wires is simply scaled down to micro- or even nano-dimensions. A process for the production of fine metal wire directly from the melt was first reported by Taylor [13] in 1924. In Taylor's inherently simple technique, subsequently known as the Taylor-wire or microwire process, the metal to be drawn is contained in a glass tube which is closed at one end. The metal is then melted and the end of the glass tube softened and drawn down to produce a fine glass-encapsulated metal filament. Since then many different metals and alloys have been produced in microwire form using this basic method [62].

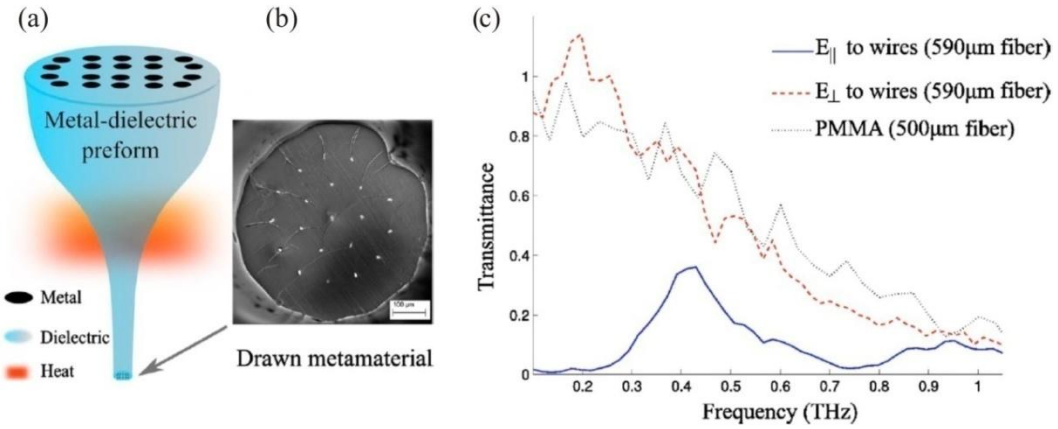

Fig. 2.2. (a) Schematic of a metal-dielectric preform, drawn into a metamaterial via heating. (b) SEM micrograph of a fabricated 590 μm indium-filled PMMA fiber cross-section. (c) Experimentally measured metamaterial transmittance, the electric field *E* is either parallel (solid line) or perpendicular (dashed line) to the wires. A measurement for an array of 500 μm PMMA fibers is also shown (dotted line) [Reprinted from Ref. [63]].

First use of the fiber-drawing techniques for production of electric metamaterials was based on the adaptation of the Taylor-wire process to indium wires in (PMMA) tubes [63]. Produced fibers comprised a hexagonal array of indium wires measuring 10 μm in diameter and 100 μm separation in a polymer fiber, and were designed to operate at terahertz frequencies as high-pass filters and polarizers [this technique shown in Fig. 2.2].

Shortly after, in our research group we have demonstrated the integration of similarly drawn metamaterials into a substrate [64]. The microwire arrays are made by stack-and-draw fiber fabrication technique using multi-step co-drawing of low-melting-temperature metals or semiconductor glasses together with polymers. Fibers are then stacked together and pressed into composite films. Optical micrographs of the fabricated films containing metal and semiconductor microwires are shown in Figure 3.2 in the Chapter 3.

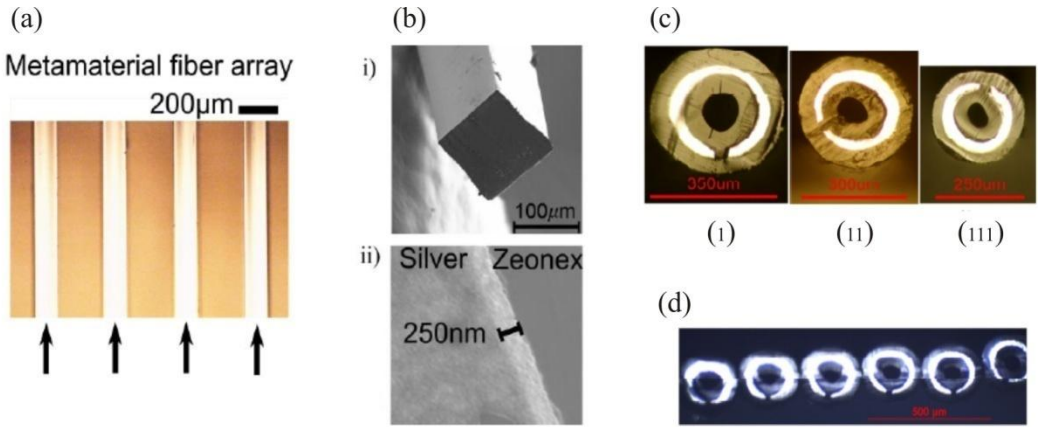

Fig. 2.3. (a) Optical microscope image of the metamaterial array. (b) SEM micrograph of i) the cross section of the metamaterial fiber and ii) of its 250 nm silver coating. (c) Optical microscope image of the cross section of (i) 350 μm, (ii) 300 μm and (iii) 250 μm fiber originating from the same preform. (c) Cross-sectional image of the spooled 250 μm fibers. [Adapted from Ref.[65]]

Recently, magnetic metamaterials were also demonstrated by fiber drawing [65, 66]. Such materials are more challenging to fabricate as they require non-circular metallic wires. The first method was based on drawing a pure dielectric fiber and then sputtering the fiber with silver from one side, creating split ring resonators (SRRs) [65] (Figure 2.3 (a, b)). These fibres have a magnetic resonance, resulting in negative relative permeability. The second method was to create

a non-circular indium shape within a polymer preform and draw this preform into a fiber [66]. Figure 1.3 (c, d) shows a resulting fiber, which also demonstrated a magnetic resonance in the THz.

2.2 Chemical or biological detection methods that operate in the terahertz spectral range

The selectivity and sensitivity of optical biosensors have put them into the class of most popular biosensors [67-70]. A large number of methods for highly sensitive chemical or biological detection that operate in the THz range were developed [68, 71, 72].

Among these methods, metamaterials and frequency selective surfaces have been employed [71, 72]. Sensing based on resonant metamaterials represents a promising direction, particularly for high sensitivity detection. As stated earlier, metamaterials are made of a collection of subwavelength resonators whose resonant frequency can be tailored according to their shape and/or geometrical dimensions. This means that metamaterials can easily be made resonant at terahertz frequencies by simple scaling of their geometry. A systematic experimental study of metamaterial sensing was performed by O'Hara et al. [71] using an array of double split ring resonators. It has been shown that even a small quantity of material deposited on THz metamaterial can shift its resonance frequency.

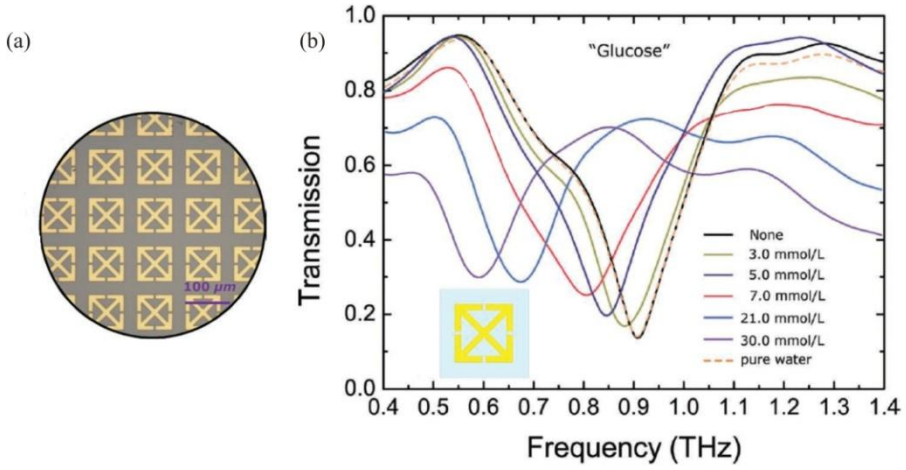

Fig. 2.4. (a) Optical microscopy image of one portion of an as-fabricated paper metamaterial sample. (b) Experimentally measured transmission spectra of the paper metamaterial sample coated with a series of glucose solution [Reprinted from Ref. [72]].

More recently, Tao et al. [72] demonstrated the use of paper metamaterials as sensors. Planar metallic resonators with minimum features of less than 5 μm have been fabricated on paper, using a photoresist-free shadow mask deposition technique. Glucose solutions with concentrations varying between 3 and 30 mmol/l were then deposited on the paper. A maximum shift of about 300 GHz was observed in measuring the 30 mmol/l glucose solution coated sample [these results are shown in Fig. 2.4].

In addition, techniques based on THz vibration spectra characterization have become available for biological materials in the form of the diluted water solutions and pressed pellets [73, 74].

The concept of using waveguides for sensing is well-established in other frequency ranges, but has only recently started maturing in terahertz systems [68, 75-78]. Notably, a significant amount of work has been done on guided-wave sensors with a focus on the novel THz waveguide geometries and sample preparation in the form of thin layers or films, which are then introduced into the waveguide structure. The propagation characteristics of a guided wave depend on several factors including frequency of operation, waveguide geometry and composition, and the nature of analyte. All of these factors influence phase and amplitude of the propagating wave. Likewise, changes in a thin sample (*e.g.*, analyte) introduced onto or into the waveguide, alter the frequency dependent phase and amplitude of the guided wave. Up to now, numerous materials have been characterized using different types of waveguides. Notably, parallel plate waveguides (PPWG) have been used extensively in THz guidance and sensing experiments [68, 75]. The PPWG is typically composed of two parallel, smooth metal plates separated with an air gap as shown in Fig. 2.5.

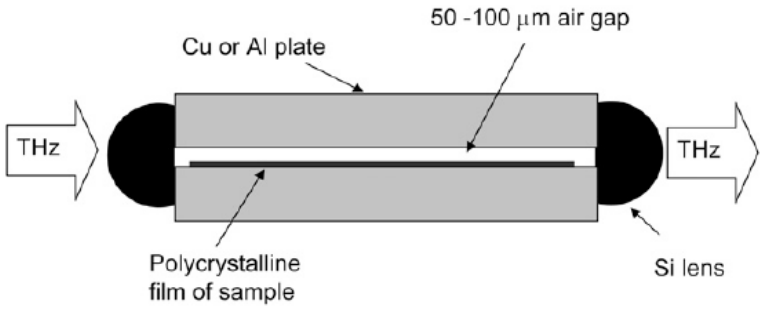

Fig. 2.5 Parallel plate waveguide (PPWG) [Reprinted from Ref.[68]].

The molecular sample is usually deposited on one of the plates in the form of polycrystalline film. Different film preparation techniques, such as drop-casting or sublimation, are employed to obtain an ordered polycrystalline film. This technique was used to obtain high-resolution THz absorption spectra of many biological molecules. This includes the nucleobase thymine, the nucleoside adenosine, the deoxynucleoside deoxycytidine, the sugar *D*-glucose, and the amino acids tryptophan, glycine, and *L*-alanine [68].

Recently, molecular spectroscopy of the polycrystalline lactose powder dispersed on the top of metal wire was demonstrated [76]. An 11-cm-long platinum/iridium wire was used in the experiments with a diameter of 254 μm and with a sharp tip on one side and a flat end on the other. Metal-wire THz-TDS combines the advantages of waveguide spectroscopy for measuring small sample amounts in close proximity to the confined THz field with the capability to increase the interaction region by simply extending the propagation length along the wire. This potentially allows either the investigation of even weakly absorbing materials such as biomolecules or extremely thin films deposited on the metal wire.

A related technique [77] measured the absorption properties of liquids in the THz wave range, based on the interaction between the liquid and the evanescent wave covering the surface of a cylindrical waveguide made of high-resistivity silicon. A test measurement was performed on a series of D-glucose solutions having various concentrations.

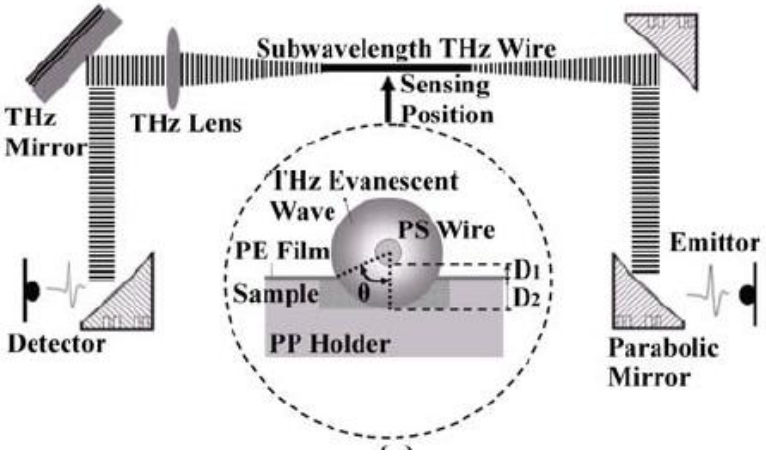

Fig. 2.6. Experimental setup for THz evanescent wave sensing by using a subwavelength plastic wire. The inset illustrates the cross section of interaction between THz evanescent wave and the sample where D_1 refers to the separation between wire and top surface of sample and D_2 denotes the depth of the PP holder [Reprinted from Ref. [78]]

A similar label-free THz sensing based on the plastic wires was also reported [78]. The THz subwavelength plastic wire used in the experiment had a circular cross-section, an infinite air-cladding, and a step-index profile. The wire core was made of polystyrene (PS), in which the refractive index is 1.59 [see Fig. 2.6]. Due to the thin core and low core index, a large portion of THz power is transmitted in the air cladding.

The enhanced evanescent wave causes considerable variation of waveguide dispersion when the cladding index changes. Based on the measured variation of waveguide dispersion dip, various concentrations of melamine alcohol solution are successfully identified.

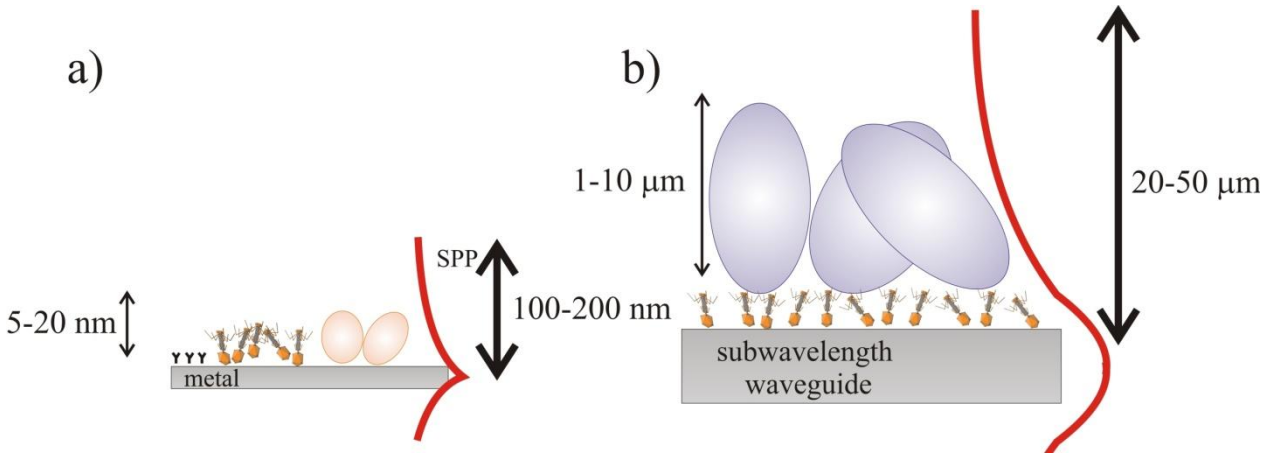

Fig. 2.7. a) Size of the plasmon's tail in visible range (typical size is less than 100 nm) and b) probing length of the evanescent field of an optical waveguide (in THz spectral range) that are used to detect changes in the optical properties at the interfaces.

The present work is motivated by the recent reports on evanescent field of surface plasmon resonance (SPR) biosensors in the visible and near-IR regions [79, 80]. Most of the investigations in these spectral regions focus on the detection of relatively low concentrations of proteins and small molecules with sizes about/less than tens of nanometers. The reason being is that the probing length of an evanescent field of an optical waveguide, or the size of the tail of a plasmon that are used to detect changes in the optical properties at the interfaces, is deeply subwavelength (see Fig. 2.7 a). For example, a typical size of a plasmon tail in the visible range is smaller than 100 nm, which allows us to track the dynamics of a biochemical event in the immediate vicinity of the interface. However, when one tries to measure directly the presence of a bacteria on a metallic surface, the standard SPR method runs into difficulty as the size of the probing field

(plasmon) is not only smaller than the size of a bacteria, but is also comparable to the size of a phage molecule (~100 nm) that connects the bacteria to the surface. Therefore the detection of large target such as cells and bacteria by SPR methods remain a challenge.

Straight fibre-optic probes suffer from low penetration depth of the evanescent field particularly in the UV/visible spectral ranges. These probes are, generally, unsuitable for thicker analyte layers such as bacteria cell layers. This problem can be addressed by adapting optical fibre probes (via geometry modification)in order to improve the overlap of the evanescent field of the fiber mode and a relatively thick analyte layer. One of the possible approaches is to operate at a shorter wavelength and then increase evanescent field presence in the analyte by fiber tapering [81] in order to match the mode extent of the analyte with the thickness of the analyte layer. In order to get a better access to the evanescent field of the guided mode one can also expose the fiber core by chemical etching [82] or bending the fiber probe [83]. Another alternative is to use longer wavelengths (such as mid- or far-IR) and then match the extent of the modal evanescent field with the analyte layer thickness by reducing the modal penetration into the cladding region by using high-refractive-index core/clad material combination. This is the method studied in our work where we explore using THz fibers operating at wavelength longer than the size of the studied object, while reducing extent of the modal evanescent field into the cladding by using high refractive index plastic/air combination.

2.3 Guiding THz waves using thin chalcogenide capillaries

Chalcogenide glasses have attracted strong interest in a view of optical applications in the near-IR and mid-IR spectral ranges (1–14 μm) [84] due to the glass relatively low losses and high nonlinearities. Furthermore, chalcogenide glass-based microstructured fibers open many interesting possibilities for a large number of applications in the mid-IR spectral range, where applications in optical sensing [85], supercontinuum generation [86, 87], and single-mode propagation of IR light [88], and transmission of the CO and CO_2 laser radiation [89, 90] have already been demonstrated. We believe that chalcogenide glasses can be also of great interest to the THz spectral range for several reasons. Particularly, as indicated in [91] these glasses offer very high refractive index, and their absorption losses show several regions of relatively low loss and high nonlinearity.

The main difficulty in designing terahertz waveguides lies in the fact that almost all materials are highly absorbent in the terahertz region [92]. Since the lowest absorption loss occurs in dry gases, an efficient waveguide design must maximize the fraction of power guided in the gas. Different types of THz waveguides have been proposed based on this concept [93, 94]. Thus, a subwavelength waveguide [94, 95], features a core with a size much smaller than the wavelength of light, and as a consequence, a large fraction of the guided light is found outside of the lossy core region. Another type of a low-loss waveguide is presented by the hollow-core fibers featuring a structured cladding that traps the light in the fiber core. As in the case of subwavelength waveguides, hollow core fibers confine most of the guided light within the low loss gas region. In the design of hollow-core fibers the main challenge is to ensure high reflection of light back into the hollow core at the core-cladding interface. Different cladding structures have been developed for the hollow-core-type waveguides, that include metallic reflectors [96-98] and various resonant multilayered dielectric [99-101] reflectors.

Among the hollow-core waveguides with resonant dielectric reflectors the simplest ones are in the form of a capillary [99-101]. In the following we refer to this type of waveguides as pipe waveguides. The structure of the THz pipe waveguide is very simple and consists only of a pipe featuring a thin dielectric layer on its inner surface with a layer size comparable to the wavelength of light. The hollow-core defined by the pipe has a diameter which is typically much larger than the wavelength of light. Similar pipe structures have also been demonstrated for guiding infrared (IR) light [102, 103]. The guiding mechanism of pipe waveguides has a resonant nature and is generally referred to as an ARROW type guidance.

The guiding mechanism in such capillaries has been well described [104, 105]. In the THz spectral range they guide via total internal reflection, while in the mid-IR spectral range guiding mechanism is dictated by the antiresonant reflection conditions where the wall of the capillary acts as a Fabry–Pérot resonator [99-101]. At the resonant frequencies, the light leaks through the capillary wall and leaves the waveguide. In contrast, when the antiresonant condition is satisfied, the field is strongly reflected by the capillary wall back into the core leading to the efficient field confinement in the hollow core. Positions of the transmission windows (spectral regions of high transmission) are, thus, defined by the resonant frequencies of the capillary wall, which can be accurately predicted. Within transmission windows, only few percent of power is guided in the capillary wall, while most of the power is guided in the air. As a result, capillary attenuation

within the transmission windows can be remarkably lower than attenuation of the bulk material. As an example, in silica pipes at THz frequencies, the attenuation coefficient can be lower than 0,03 cm^{-1} (13.62 dB/m), whereas absorption of the bulk silica is around 2 cm^{-1} [105, 106], signifying that the light propagation loss in the capillary is almost 100 times lower than the light propagation loss in the bulk material. Clearly, as the capillary thickness increases, light propagation loss will also increase.

CHAPTER 3
COMPOSITE THZ MATERIALS USING ALIGNED METALLIC AND SEMICONDUCTOR MICROWIRES, EXPERIMENTS AND INTERPRETATION

3.1 Introduction

In this section we study the fabrication and optical properties of continuous uniform metamaterial films fabricated by densification technique, where individual metamaterial fibers are first aligned and then pressed together at elevated temperature. The effective refractive index and the permittivity of such composite media have complex frequency dependence. In order to extract a material's effective optical parameters from transmission measurements a transfer matrix-based analytical model of transmission trough a 3-layer metamaterial film was first developed. A numerical procedure was then used in order to fit experimental data with transmission curves generated by the semi-analytical formulas containing effective optical parameters as fitting variables.

Right from the start the two main distinctive features of our metamaterials should be pointed out. First of all, most of the existing experimental studies of the THz wire array materials deal with highly ordered arrays of relatively large diameter wires (hundreds of microns). For such materials, a comparison with analytical theories (Pendry's formula, for example) developed for strictly periodic structures is relatively straightforward. In our case, due to the specifics of the fabrication technique, we create the arrays of parallel yet randomly positioned microwires of variable from wire-to-wire diameters on the order of 1-10 microns. Therefore, the applicability of formulas developed for periodic wire arrays to our metamaterials is questionable, if at all justified. Instead, to describe our metamaterials one has to use effective random media theories such as Maxwell-Garnett or Bruggeman theories. Moreover, in most experimental work on the wire-array media, one typically uses commercial wires made of pure metals such as copper or gold having dielectric constants that can be fitted well with a Drude model. Again due to the specifics of our fabrication technique, we could only use low melting temperature alloys which are thermo-mechanically compatible with plastics used during fiber drawing. In particular, we

use alloys of semi-metals Tin (Sn) and Bismuth (Bi) with dielectric constants that cannot be generally described by a simple Drude model.

Finally, it will be demonstrated that metal containing metamaterials yield strong polarization effects, as well as the possibility to design high refractive index composite materials using chalcogenide nanowires.

3.2 Fabrication process

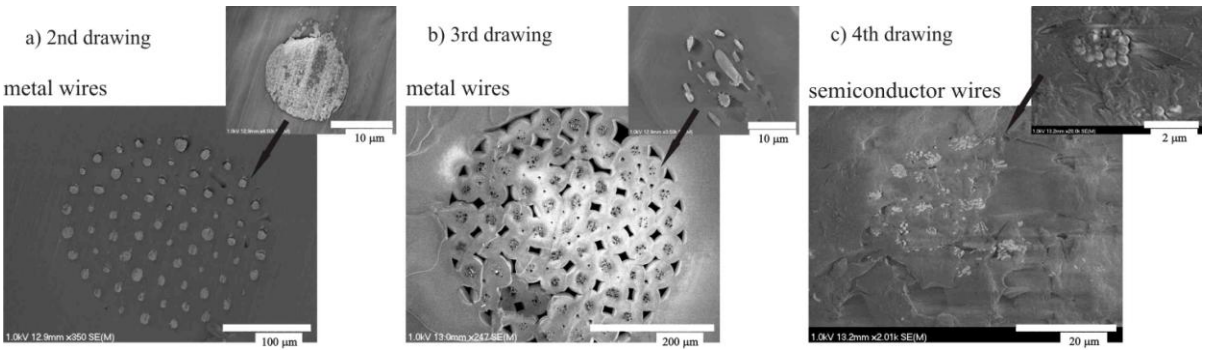

Fig. 3.1. SEM pictures of the cross-sections of fabricated wire-array metamaterial fibers. a) metal wire fiber after 2nd drawing, b) metal wire fiber after 3rd drawing, c) semiconductor wire fiber after 4th drawing. Insets show magnification of individual wires. Inset of c) shows cluster of nanowires with the individual fiber diameters as small as 200nm.

The microwire arrays are made by the stack-and-draw fiber fabrication technique using co-drawing of low melting temperature metals or amorphous semiconductor glasses together with polymers. The fabrication process of both metal and chalcogenide glass (As_2Se_3) samples is similar and can be divided into several steps. First, we prepare microstructured fibers containing microwire arrays. For that we start by filling a single PC (polycarbonate) tube with a liquid melt (T_m ~ 130˚C) of Bismuth and Tin alloy (42% Bi, 58% Sn). After the first preform is made it is drawn at 190˚C into a polymer-clad wire with a diameter of ~ 260 μm (first drawing). We then stack hundreds of wires together, clad them with another PC tube and draw it again under the same temperature. A scanning-electron-micrograph of the cross-section of a composite fiber after the second drawing is shown in Fig. 3.1 (a). Inset is a magnification of an individual wire of size ~ 10 μm. Note that after the first drawing, metallic wire is surrounded by a polymer cladding of

thickness comparable to the size of a wire. Relatively thick cladding is needed to prevent individual wires from coalescing with each other during the following consecutive drawings.

By repeating stack and draw process several times we can create ordered wire arrays with sub-micron size wires. The inset in Fig. 3.1 (c) shows crossection of a fiber after the 4th drawing featuring semiconductor wires with diameters as small as 200 nm. Finally, to create metamaterial films we use fibers after the 3rd drawing, place them on a flat surface next to each other and then press them under pressure of several tons at 195˚C. Fig. 3.2 presents optical micrographs of the cross-sections of a film containing metal (Fig. 3.2 (a)) and semiconductor (Fig. 3.2 (b)) microwire arrays. When pressing the fibers a three-layer film is created. The fiber polymer cladding creates the two outer polymer layers that sandwich a metamaterial layer.

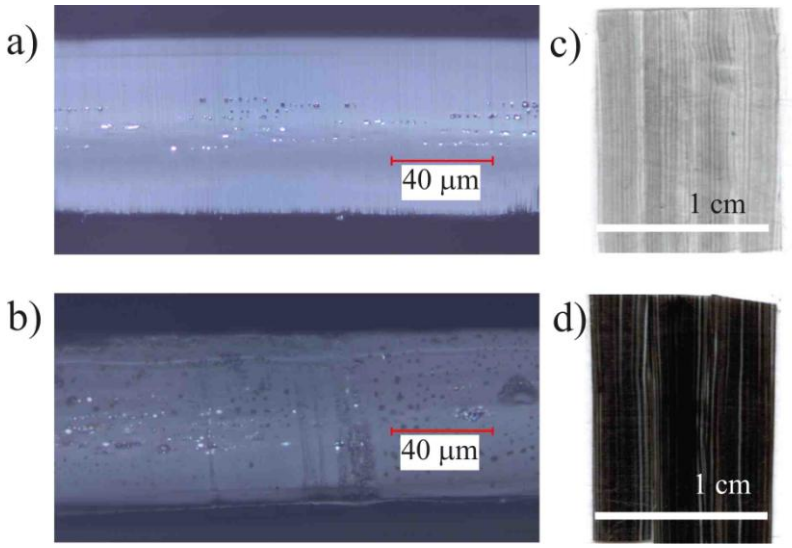

Fig. 3.2. Optical micrographs of a film containing (a) metal, and (b) semiconductor microwire arrays. The metamaterial layer is sandwiched between the two polymer layers. Figures (c) and (d) present top view of the films where metal and semiconductor wires can be seen to traverse the entire span of the film.

Fig. 3.2 (c, d) presents an optical micrograph displaying the top view of a metamaterial film, where the aligned metal (c) or chalcogenide (d) wires can be clearly seen. From the SEM images of the pressed films we see that the wire size fluctuates in the range 0.5–4 μm. To create semiconductor nanowires we follow the same fabrication procedure but start with As_2Se_3

semiconductor chalcogenide glass rods cladded with a PSU (PolySulphone). Fibers were then drawn at 300˚C and subsequently arranged and pressed into films at temperatures 280˚C and pressures of several thousands of PSI.

A single fiber drawing yields hundreds of meters of a uniform diameter fiber. Cutting, stacking, and pressing such fibers into films enables fabrication large area composite films. In our experiments we have produced films having an area of several cm^2, with the main limitation being the size of the hot press. The main challenge in pressing the composite films is to guarantee the uniformity of the metamaterial layer. Because of the relatively thick plastic cladding of the individual wires, most of the pressed films show stripes of metal wires separated by stripes of clear plastic. Press parameters have to be chosen carefully to guarantee that during the compactification process the wires are free to intermix in the horizontal plane without loss of alignment.

3.3 Transmission measurements

Transmission spectra for the films were then studied in the whole THz range (0.1–20 THz) using a combination of Terahertz Time-Domain Spectroscopy (THz-TDS) and Fourier-Transform Infra-Red spectroscopy (FTIR). In Fig. 3.3 (a) we present the FTIR transmission spectra of a metamaterial film containing ordered metal wires (in the range 0.1–20 THz) for two different polarization of the incoming light. Grey color corresponds to polarization of the electric field parallel to the wires, whereas black color corresponds to polarization perpendicular to the wires. As seen from Fig. 3.3 (a) metamaterial films are strongly polarization sensitive for frequencies up to 5 THz, while polarization sensitivity persists up to 10 THz. For comparison, in Fig. 3.3 (b) we present transmission spectra through a metamaterial film containing As_2Se_3 semiconductor glass wires, where no polarization sensitivity is observed.

The polarization dependence of THz light transmission through metamaterial samples is clearly seen in Fig. 3.3 (a); however, the lack of phase information makes it difficult to retrieve the corresponding effective refractive indices for the two polarizations. As shown in Fig. 3.3 (a), light polarized parallel to the metal wires is blocked, while light polarized perpendicular to the wires is largely transmitted. The wire-grid polarizer consists of an array of slender wires arranged parallel to one another. The metal wires provide high conductivity for the electric fields parallel to the wires. Such fields produce electric currents in the wires, like the microwave dipole receiver

antenna. The energy of the fields is converted into energy of currents in the wires. Such currents are then partially converted to heat because of the small but significant electrical resistance of the wires, and partially irradiated back. The physical response of the wire grid is, thus, similar to that of a thin metal sheet. As a result, the incident wave is mostly absorbed or reflected back and only weakly transmitted in the forward direction. Because of the nonconducting spaces between the wires, no current can flow perpendicular to them. So electric fields perpendicular to the wires produce virtually no currents and lose little energy, thus, there is considerable transmission of the incident wave. In this respect, the wire grid behaves as a dielectric rather than a metal sheet.

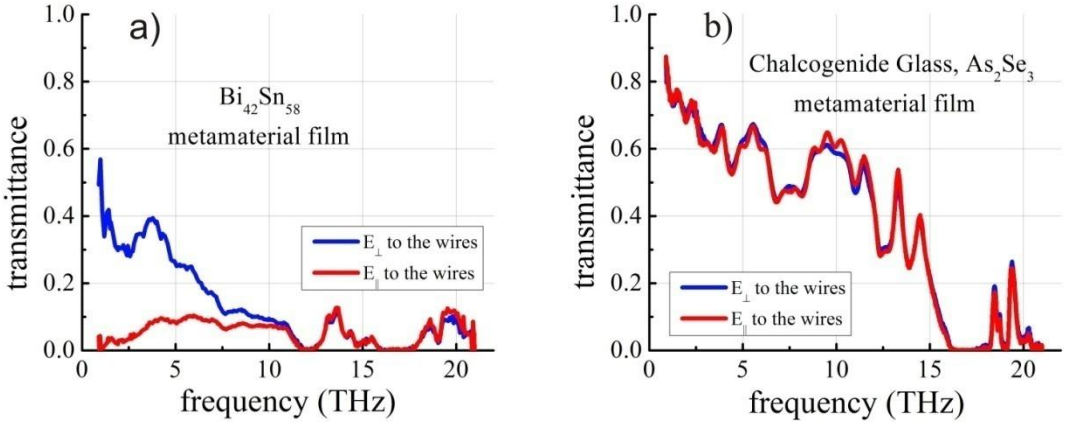

Fig. 3.3. FTIR transmission spectra (0.1–20 THz) of a metamaterial film containing ordered (a) metal and (b) semiconductor wires. Strong polarization dependence of transmission spectrum is observed for metallic wire arrays.

Alternatively, for the parallel polarization of incoming wave, the response of a wire-grid medium can be modeled as that of a metal with an effective plasma frequency defined solely by the geometrical parameters of the medium such as wire size and inter-wire separation. Thus, at lower frequencies below the effective plasma frequency of a wire medium, electromagnetic waves are effectively blocked by such a material. However, at frequencies above plasma frequency polarization sensitivity of the wire grid medium is greatly reduced as both polarizations can go through the medium. At even higher frequencies when the inter-wire spacing and individual wire size (which are comparable in our samples) become comparable to the wavelength of light the metamaterial approximation breaks down. In our samples we observe that

polarization sensitive transmission through the wire-medium is lost completely at frequencies higher than 10 THz.

In order to obtain the complex permittivity of the samples, complex transmission spectra (amplitude (Fig. 3.4 a, c) and phase (Fig. 3.4 b, d)) through metamaterial films were measured with a THz-TDS setup. The THz-TDS setup uses a frequency-doubled femtosecond fiber laser (MenloSystems C-fiber laser) as a pump source. Identical GaAs dipole antennae were used as THz source and detector yielding a spectrum ranging from 0.1 to 3 THz. The FWHM spot size of the THz beam at the focal point of the parabolic mirrors is roughly 3 mm. For convenient handling of samples, the metamaterial films were cut into 1cm x 1cm pieces and placed at the focal point of the parabolic mirrors. For each film sample, two transmission spectra were measured corresponding to the parallel and perpendicular polarizations of the THz beam with respect to the wire direction.

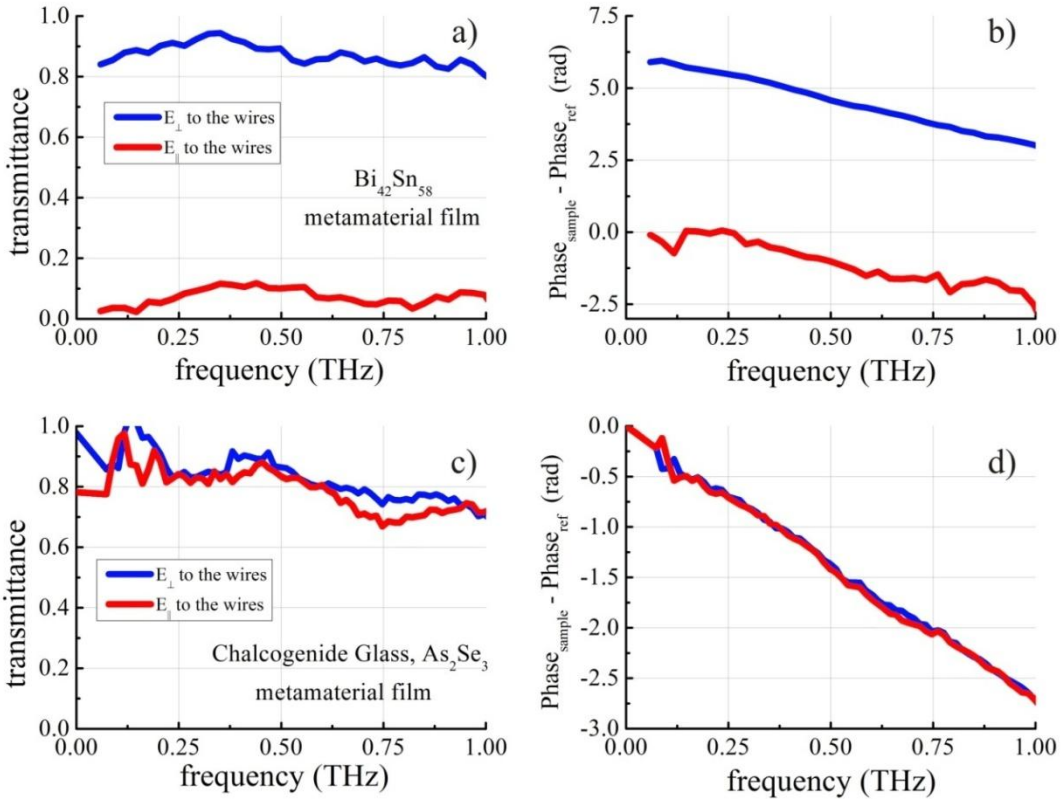

Fig. 3.4. Transmission spectra (a, c) and phase difference (b, d) of THz light through metamaterial film containing (a, b) ordered metallic wires, (c, d) ordered semiconductor wires.

To ensure constant input illumination conditions during rotation of samples, we used a rotation mount (RSP1 from Thorlabs). It utilizes two precision bearings for smooth, backlash-free rotation, and a small iris was inserted in the center of the rotation mount. The metamaterial film was then placed over the iris. The normalized transmittance through the metamaterial film was calculated by dividing the transmission data with, and without, the metamaterial film.

3.4 Interpretation of the experimental data

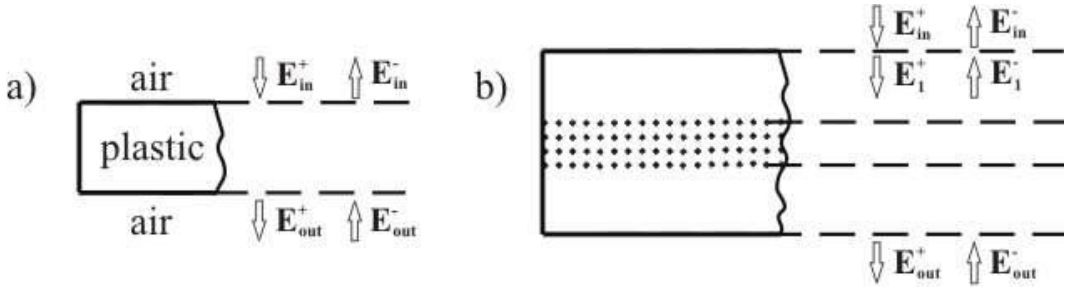

Fig. 3.5. Schematic of (a) one layer of plastic and (b) a metamaterial film modeled as a three layer system. The subscripts indicate the layer number, while the + and the – signs distinguish incoming and outgoing waves, respectively.

In order to infer the optical parameters of metamaterial layers, one has to assume a particular geometry of a composite film, as well as optical parameters of the constituent materials. As mentioned previously, the fabricated films can be viewed as a three-layer system (Fig. 3.2 a, b), where a wire metamaterial layer is sandwiched between the two polymer layers (either PC or PSU for metal or chalcogenide wire films, respectively). Therefore, we first characterize refractive indexes and absorption losses of the pure PC and PSU polymers. We then use this data to fit the parameters of a metamaterial film.

3.4.1 Procedure for retrieving the refractive index and losses of pure polymers

Characterization of refractive indices of pure plastics is done with THz-TDS setup using thick polymer slabs with parallel interfaces. Samples were prepared by pressing the PC or PSU tubes into thick films at temperatures similar to those used during the fabrication of metamaterial films. Transmission spectra and phase difference of THz light through the plastic slabs are shown at Fig. 3.6 (a, b).

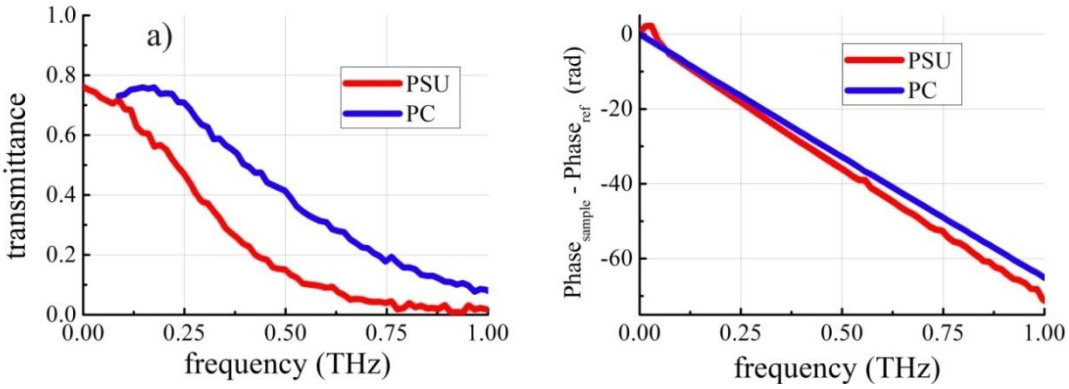

Fig. 3.6. Transmission spectra (a) and phase difference (b) of THz light through a plastic slabs.

We retrieve the refractive index and absorption losses of pure plastics by fitting the predictions of a transfer matrix model to the experimental transmission data [107-109]. Particularly, using the + and – superscripts to denote forward and backward traveling waves, the field amplitudes before and after a plastic slab are:

$$\begin{pmatrix} E_{in}^{+} \\ E_{in}^{-} \end{pmatrix} = \prod_{i=1}^{2} M_{i-1,1} \begin{pmatrix} E_{out}^{+} \\ 0 \end{pmatrix} = \begin{bmatrix} T_{11}^{m} & T_{12}^{m} \\ T_{21}^{m} & T_{22}^{m} \end{bmatrix} \begin{pmatrix} E_{out}^{+} \\ 0 \end{pmatrix} . \tag{3.1}$$

The complex field transmission coefficient through a single layer is then given by

$$t = \frac{1}{T_{11}^{m}} = \frac{t_{a,p} t_{p,a} \exp(-i n_p \omega d_p / c)}{1 + r_{a,p} r_{p,a} \exp(-2i n_p \omega d_p / c)} , \tag{3.2}$$

where $r_{a,p}$, $r_{p,a}$ and $t_{a,p}$, $t_{p,a}$ are the complex reflection and transmission Fresnel coefficients of the interface between air (subscript *a*) and plastic (subscript *p*), as well as between plastic and air respectively. These coefficients have the same form for both *s* and *p* polarizations due to normal angle of radiation incidence. Denoting d_p to be the plastic layer thickness, and n_p to be the refractive index of a plastic layer, we can write:

$$t_{a,p} = \frac{2n_a}{n_a + n_p} , \tag{3.3}$$

$$r_{a,p} = \frac{n_a - n_p}{n_a + n_p} \ . \tag{3.4}$$

For the calculation of refractive index and absorption losses of pure plastics we can assume that slabs are thick enough, so that multiple reflections within a sample (*i.e.* Fabry-Pérot reflections) can be neglected. In this case we can assume that the denominator of Eq. (3.2) simply equals 1, which allows us to write:

$$t = T(\omega)e^{i\phi} = \frac{4n^{real}(\omega)}{(n^{real}(\omega)+1)^2}\exp\left(-i\frac{\omega d_p}{c}\left(n^{real}-1\right)\right)\exp\left(-\frac{1}{2}\alpha d_p\right) . \tag{3.5}$$

The transmittance $T(\omega)$ and phase shift φ at each frequency are obtained simultaneously by the THz-TDS measurements. Eq. (3.5) easily separates into two equations respectively for the real and imaginary parts of the refractive index [92, 110]. For n^{real} and α we get:

$$n^{real}(\omega) = 1 + \frac{c\phi}{\omega d_p} \ , \tag{3.6}$$

$$\alpha = 2n^{im}\omega / c = \frac{2}{d_p}\ln\left(\frac{(n^{real}(\omega)+1)^2 T(\omega)}{4n^{real}(\omega)}\right) . \tag{3.7}$$

It is important to realize that imaginary part of the refractive index of common plastics in THz frequency range can be several percent from the value of the real part of the refractive index. Therefore, to guarantee the third digit accuracy in the value of the real part of the extracted refractive index, Eq. (3.6, 3.7) may no longer be valid, and the use of the complete formula Eq. (3.5) may be necessary. Experimentally the thicknesses of the two polymer slabs were 5 mm. In fact, the samples should be thick enough so that multiple Fabry-Pérot reflections are suppressed via absorption of the reflected waves on the length scale of a sample width. On the other hand, the sample should not be too thick, otherwise absorption losses even after one passage would be too large to make a reliable measurement of a transmitted field.

The value of the fitted refractive index of PC is almost constant across the whole THz range and it equals to $n = 1.64$, which is in good agreement with prior reports [92]. Absorption loss of plastics are a rapidly increasing function of frequency which can be fitted as PC:

$\alpha_{PC}[cm^{-1}] = 3.77f + 6.65f^2$, PSU: $\alpha_{PSU}[cm^{-1}] = 5.03f + 20.25f^2$,where f is frequency in [THz]. In this work, for the first time to our best knowledge, we also report the THz refractive index of PolySulphone $n = 1.74$, which is also effectively constant across the whole THz range. Fig. 3.7 details frequency dependence of the PC and PSU refractive indices (a) and absorption losses (b) obtained by fitting the experimental transmission data.

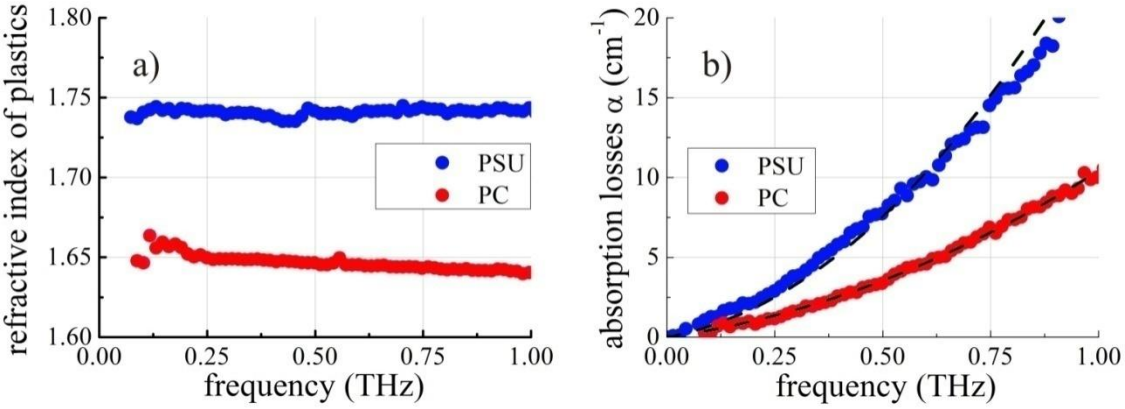

Fig. 3.7. a) real part of the refractive index and b) absorption losses of pure plastics PC, PSU.

3.4.2 Procedure for retrieving the refractive index and permittivity of metamaterial layers

As mentioned earlier, we model the experimental films as a three-layer system (Fig. 3.5 b)) where a wire metamaterial layer is sandwiched between two polymer layers (either PC or PSU for metal or chalcogenide-based wire arrays). We start with the metal wire-based metamaterial films. The total thickness of such films is 150 μm. Thickness of a metamaterial layer alone is 35±5 μm. The layer comprises metal wires of 1.3±0.5 μm average diameter.

The complex transmission of a 3-layer system is modeled using a transfer matrix theory, assuming that a multilayer is surrounded by air. The field amplitudes E_{in}, E_{out} in the first and last semi-infinite air regions respectively are related via the product of four 2×2 transfer matrices on each interface:

$$\begin{pmatrix} E_{in}^{+} \\ E_{in}^{-} \end{pmatrix} = \prod_{i=1}^{4} M_{i-1,1} \begin{pmatrix} E_{out}^{+} \\ 0 \end{pmatrix} = D_0^{-1} \left[\prod_{i=1}^{3} D_i P_i D_i^{-1} \right] D_4 \begin{pmatrix} E_{out}^{+} \\ 0 \end{pmatrix} = \begin{bmatrix} T_{11}^{m} & T_{12}^{m} \\ T_{21}^{m} & T_{22}^{m} \end{bmatrix} \begin{pmatrix} E_{out}^{+} \\ 0 \end{pmatrix}. \qquad (3.8)$$

Each side of an interface is represented by the corresponding transmission matrix D_i, whereas the propagation inside the bulk material of each layer is represented by its propagation matrix P_i

$$D_i = \frac{1}{t_{i-1,i}} \begin{bmatrix} 1 & r_{i-1,i} \\ r_{i-1,i} & 1 \end{bmatrix}, \tag{3.9}$$

$$P_i = \begin{bmatrix} \exp(i\frac{n_i \omega d_i}{c}) & 0 \\ 0 & \exp(-i\frac{n_i \omega d_i}{c}) \end{bmatrix} , \tag{3.10}$$

where $r_{i-1,i}$ and $t_{i-1,i}$ are the complex reflection and transmission Fresnel coefficients:

$$t_{i-1,i} = \frac{2n_{i-1}}{n_{i-1} + n_i} , \tag{3.11}$$

$$r_{i-1,i} = \frac{n_{i-1} - n_i}{n_{i-1} + n_i} , \tag{3.12}$$

of the interface, d_i is the thickness of i layer, and n_i is the complex refractive index. In our case we made only transmission measurements, thus we only have amplitude and phase information about the forward traveling waves E_{in}^{+} and E_{out}^{+}. The complex transmission coefficient of the multilayer is given in terms of the system transfer matrix elements T_{ij} as $T_{theor} = 1/T_{11}^{m}$. The THz-TDS setup allows to obtain information about amplitude E_{out}^{+} and phase ϕ of the signal transmitted through the sample for all THz frequencies in a single measurement. The measured complex transmission coefficient is obtained from the ratio of the sample and reference fields,

$$T_{measured} = T(\omega)e^{i\phi} = E_{out}^{+}(\omega) \big/ E_{ref}^{+}(\omega)e^{i(\phi - \phi_{ref})} . \tag{3.13}$$

The reference field amplitude E_{ref}^{+} and phase ϕ_{ref} are obtained by measuring the signal without sample. Assuming that multilayer geometry and refractive index of a host material are known, complex refractive index of the metamaterial layer is found by taking the difference

between the measured and theoretical transmission coefficients to be zero, and then finding the roots of a resultant equation:

$$T_{measured} - T_{theory}\left(\mathrm{Re}\left(n_{meta}\right), \mathrm{Im}\left(n_{meta}\right)\right) = 0 \ . \tag{3.14}$$

Note that Equation (3.14) is effectively a system of two purely real equations for the real and imaginary parts of the complex transmission coefficient. This system of equations has two unknowns, which are the real and imaginary parts of the metamaterial refractive index. Therefore, equation (3.14) is well defined.

The theoretical transmission coefficient of the multilayer depends on the knowledge of the exact thicknesses of the layers and their complex refractive indices. While the complex refractive indices of the host polymers, as well as the total thicknesses of a multilayer have been accurately measured, the thickness of a metamaterial layer must be assumed to be an adjustable parameter since its accurate estimation from the micrographs is not possible due to ambiguity in the definition of a boundary between metamaterial and a plastic cover. As it will become clearer in the following section, the exact choice for the value of the thickness of a metamaterial layer can only be made if an additional optimization criterion is established. Without a supplemental restriction on Eq. (3.14), this equation can be solved for any given value of the metamaterial layer thickness. To solve numerically Eq. (3.14) we use a nonlinear Newton method for the real and imaginary parts of the refractive index at each frequency point. Another subtlety in solving Eq. (3.14) comes from the possibility of multiple solutions of this equation. For the cases with more than one solution, unphysical solutions are eliminated by verifying their compatibility with the Kramers–Kronig relations. Finally, the effective permittivity is calculated from the extracted complex refractive index of the metamaterial in order to facilitate the interpretation of the metamaterial behaviour and the analysis via the effective medium theory.

3.4.3 Extracted refractive index and permittivity of the films

Figure 3.8 presents the complex refractive index and complex permittivity of the metal wire metamaterial films, calculated using the transmission spectra of Fig. 3.4. (a) and the procedure described in the previous section. A clear difference in the reconstructed optical properties of a metamaterial layer can be seen for the two polarizations of the incident light. Not surprisingly, we find that a wire-grid structure behaves like a metal ($\mathrm{Re}(\varepsilon) < 0$ and $\mathrm{Im}(\varepsilon) > 0$)

for the electromagnetic waves polarized parallel to the wires. From Fig. 3.8 we see that the real part of the dielectric constant of our metamaterial changes sign around 1THz, which within the Drude model corresponds to the metamaterial plasma frequency.

Alternative interpretation for the operational principle of the wire grid polarisers is in terms of the effective plasma frequency of a metamaterial. This was proposed by Pendry et al. [32] to explain wave propagation through a 2D array of wires. He demonstrated that such an array behaves like a Drude metal with effective plasma frequency which is only a function of the geometrical parameters of a wire array $\omega_p^2 = 2\pi c^2 \Big/ \left(a^2 \ln(a/r)\right)$, where c is the speed of light in vacuum, a is the inter-wire spacing, and r is the wire radius. Several more complicated but precise derivations of the effective plasma frequency for the wire medium have been developed [33] and a comparison between the models has been conducted in [34]. Since the effective plasma frequency in a wire medium can be tuned by adjusting the medium's geometrical parameters, the spectral region for the desired permittivity values can be engineered to occur at practically any frequency.

At this point it would be interesting to estimate theoretically the plasma frequency of our metamaterial using Pendry's model. However, in our case we believe that the results of such a prediction would have a limited validity. Particularly, Prendry's plasma frequency is derived for a periodical network of wires of a fixed diameter. From the SEM pictures of a typical cross-section of the wire-array metamaterial fibers after 3rd drawing (see Fig. 3.1) we see that the wire diameter fluctuates in the range 0.5–4 μm, with an average wire size being around 1 μm. The distance between wires could be estimated from the optical micrograph of the film containing metal microwire array (Fig. 3.2), we see that it varies between 5 μm and 50 μm. Thus, when using Pendry's formula we get estimates to the plasma frequency ranging from 1 THz (d=0.5 μm, a=50 μm) to over 25 THz (d=4 μm, a=5 μm). Therefore, applicability of the Pendry's formula to random wire arrays is not obvious.

In passing we mention that there is a growing body of work dedicated to the study of influence of disorder in the metal wire arrays on their transmission properties. Thus, small disorder typically results in the shift of plasma frequency to lower frequencies [111]. Disorder also leads to increase in the attenuation of the wire medium, which is, moreover, highly sensitive to the particular realisation of a disorder. In general, in disordered systems plasmonic response

becomes less pronounced [112]. In metamaterials consisting of split ring resonators, small disorder yields to narrowing and reduction of the resonance gap [113], while large disorder could lead to a complete suppression of resonances [114].

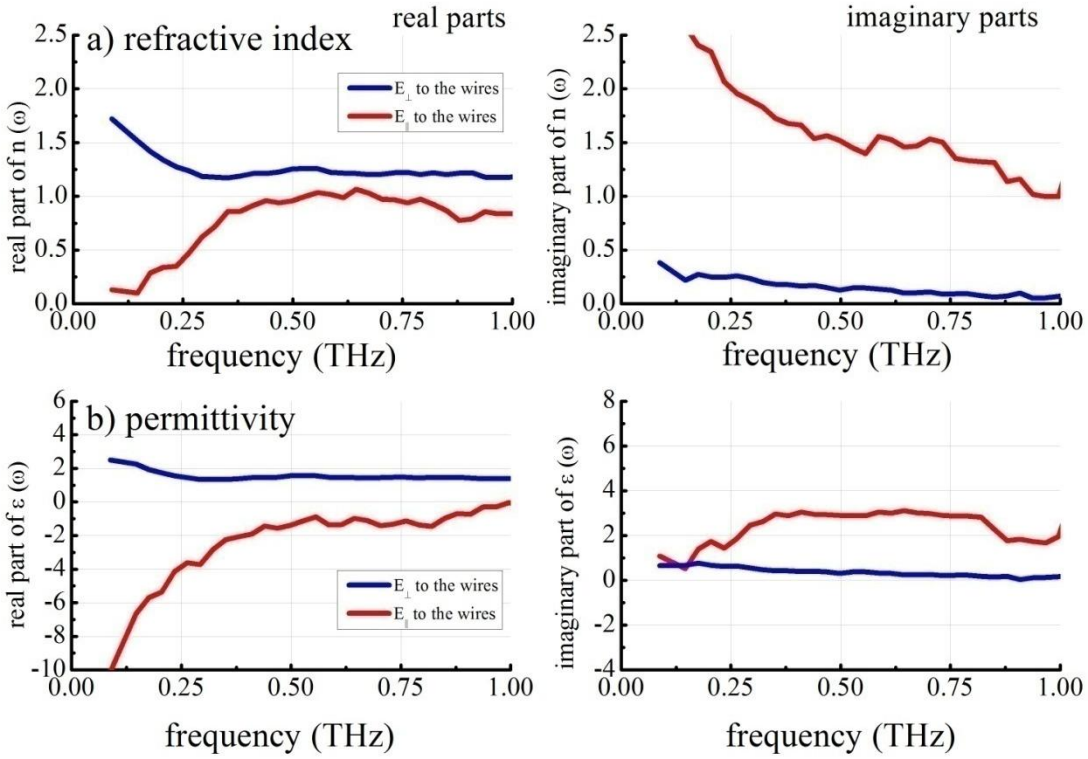

Fig. 3.8. Extracted (a) refractive index, and (b) permittivity of a metamaterial layer containing metal wires.

As we note from Fig. 3.8 (b), while frequency behavior of the real part of the metamaterial dielectric constant is consistent with a Drude model ($\mathrm{Re}(\varepsilon)$ changes sign from negative to positive at plasma frequency), the imaginary part of the metamaterial dielectric constant does not exhibit a typical Drude behavior ($\mathrm{Im}(\varepsilon)$ should decrease monotonically as frequency increases). We believe that there are two reasons for the non-Drude behavior of our material, one is related to the inversion algorithm, and another is related to the non-Drude nature of the semimetals from which our metamaterial is made. At this point we cannot say with certainty which is the main reason and additional studies are still needed to resolve this issue.

The first reason is due to extraction algorithm itself. Note that due to manufacturing process, the metamaterial layer is thin ~ 40 μm. As a result, even with relatively high absorption

losses in a metamaterial layer where $\mathrm{Im}(\varepsilon) \sim 2$ one cannot disregard interference effects in the metamaterial layer. The extraction algorithm, therefore, is based on a full transfer matrix theory and uses the roots of highly nonlinear equation where real and imaginary parts of the metamaterial dielectric constant are strongly coupled to each other. We note that non-Drude behavior of $\mathrm{Im}(\varepsilon)$ is most pronounced in the spectral region of low frequencies below 0.3 THz. This is the region where THz source power is already quite low. At the same time, this is the region where real part of the dielectric constant is negative and very large (compared to the imaginary part). We, therefore, observe that uncertainties in the intensity and phase data results in relatively small errors in the $\mathrm{Re}(\varepsilon)$, while potentially large errors in $\mathrm{Im}(\varepsilon)$. Therefore, non-Drude behavior of $\mathrm{Im}(\varepsilon)$ of our metamaterial at lower frequencies can be related to the artifact of inversion algorithm. A way to improve the accuracy of inversion algorithm would be to work with much thicker metamaterial samples, so that interference effects inside metamaterial layer could be ignored. In this case one can simply assume an exponential decay of THz light in the metamaterial layer, and in the resultant equations real and imaginary parts of the metamaterial dielectric layer would be decoupled.

Second reason is the non-Drude behavior of the semimetals and their alloys from which our metamaterial is made. Particularly, it is suggested in several references that spectral behavior of the terahertz conductivity of the poor conductors (such as semi-metals Sn, Bi and their allows), as well as materials near the metal-insulator transition is described by a Drude-Smith model which is a generalization of the Drude model, that can exhibit a substantially different frequency dependence from a classical Drude model [115]. In our samples we use Bismuth Tin alloy, bulk electrical conductivity of which is only around 2% of the conductivity of the pure Copper. Moreover, it is known that in micro and nanostructures (such as microwires in our case) Bismuth Tin alloy exhibits phase separation into pure metals, which greatly complicates description of the electrical properties of such alloys [116]. In our case phase separation manifests itself in formation of the nano-sized grids as presented in Fig. 3.10 of the last section. There are several works about refractive index and conductivity of nanostructured Bi in the form of thin (sub-micron) Bismuth layers [117, 118]. In these works they conclude that the plasma frequency of the nanosized Bi films is on the order of $\nu_{pl} = 100$ THz. At the same time, plasma frequency of the monocrystal bismuth was reported to be $\nu_{pl} = 4.86$ and 5.64 THz, depending on the anisotropy

axis orientation [119], which is more than 20 times different from the plasma frequency of Bi thin films. From this we conclude that microstructure of the semimetal alloys can influence dramatically its electrical properties. To remedy this complexity in our future work we will try to find the material combination of plastics and pure low melting temperature metals such as In, Sn or Bi, to fabricate microwire arrays with electrical properties that would be easier to interpret. The only reason for the use of Tin Bismuth alloy in this work was that it showed outstanding compatibility with the plastic host material during drawing. Finally, additional experiments are needed to study optical properties of the pure low melting temperature metals in the vicinity of 1 THz, which are still not available in the literature.

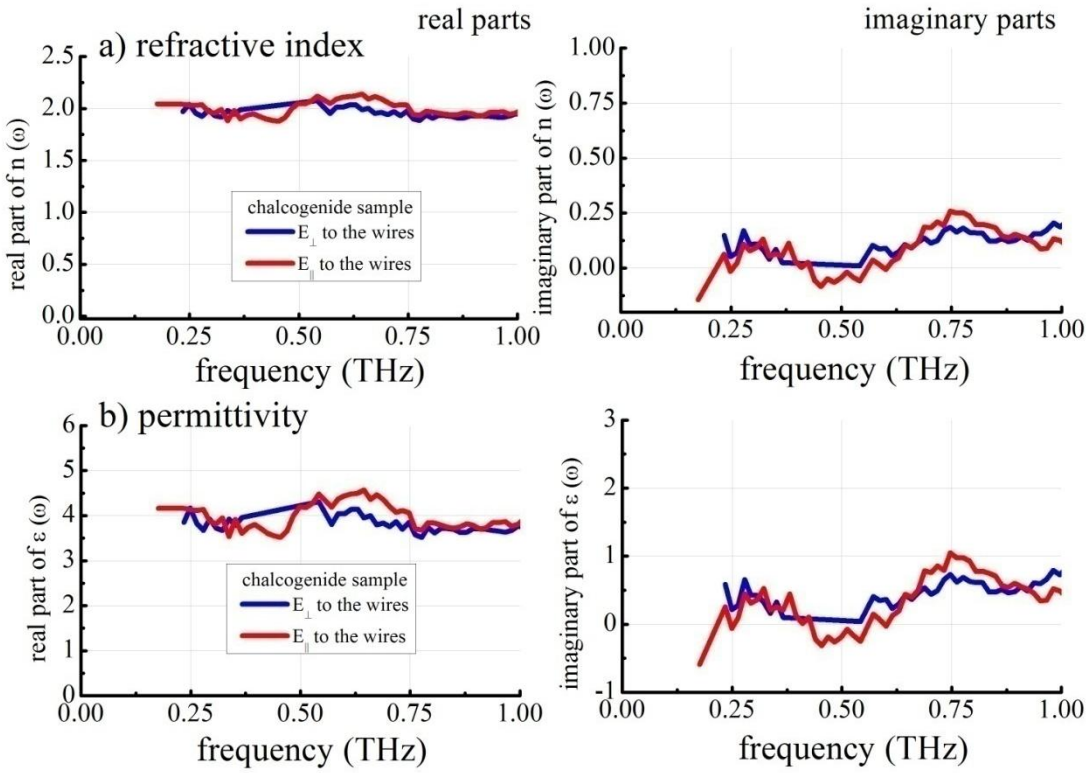

Fig. 3.9. Extracted (a) refractive index, and (b) permittivity of a metamaterial layer containing chalcogenide glass wires

Finally, for comparison with the metal wire arrays, we present the refractive index and permittivity of the metamaterial layer containing chalcogenide glass wire array. The values calculated from the transmission spectra of Fig. 3.4 (b) are shown in Fig. 3.9. Due to the low conductivity of the chalcogenide wires, the wire-array does not act as an effective metal and there

is no difference between the polarizations parallel or perpendicular to the wires. In this case, the chalcogenide glass inclusions merely form a dielectric composite material having a significantly higher refractive index compared to the pure PSU plastic host.

3.5 Discussion

Here we would like to discuss briefly two issues that are related to the fundamental relation between the components of a dielectric tensor of a wire array medium, and to the unexpected self-organized nanostructure observed when drawing wires from the binary alloys.

3.5.1 Effective medium theory

It is interesting to note that according to the effective medium theories [20, 21, 30], components of the dielectric tensor of a wire array metamaterial are not independent. They are, in fact, well defined functions of the filling factor and dielectric constants of the metal and host materials. Therefore, one can, in principle, design an algorithm that can check consistency between the experimentally measured parallel and perpendicular components of the metamaterial dielectric tensor. The goal, for example, is to determine validity of various assumptions for the geometrical and material parameters that are made in the data interpretation algorithms, thus improving their reliability.

A typical effective medium theory assumes that inclusions (spheres, discs, rods) are randomly dispersed within a host matrix, and that these inclusions are much smaller than the wavelength of light inside the host material (<0.1– 0.2 λ). Among many effective medium theories, one of the most popular is the Maxwell-Garnett model [23, 24], which uses as a fundamental parameter a volume fraction (filling factor) $f = V_{particles}/V_{background}$ of the particles embedded in the uniform background material. In the case of wire arrays, $V_{background}$ is proportional to the active area of the background material, and $V_{particles}$ is proportional to the total area of the metallic wires. For the polarization parallel to the wires, the effective permittivity of the composite in Maxwell-Garnett approach is then given by:

$$\left(\frac{\varepsilon^{\parallel}_{eff\,(theory)}(\omega) - \varepsilon_{plastic}}{\varepsilon^{\parallel}_{eff\,(theory)}(\omega) + \varepsilon_{plastic}} \right) - f \left(\frac{\varepsilon_m - \varepsilon_{plastic}}{\varepsilon_m + \varepsilon_{plastic}} \right) = 0 \ , \qquad (3.15)$$

where ε_m is the dielectric constant of the wires, and $\varepsilon_{plastic}$ is the dielectric constant of the host material. For polarization perpendicular to the wires the effective permittivity of the composite is:

$$\varepsilon^{\perp}_{eff\,(theory)}(\omega) = f\varepsilon_m + (1-f)\varepsilon_{plastic} \ . \tag{3.16}$$

In order to find the optimal value of the filling factor and thickness of a metamaterial layer that one uses in the data interpretation algorithms, one can proceed by simultaneous minimization of the two weighting functions:

$$Q_{\parallel}(d,f) = \int_{\omega_{\min}}^{\omega_{\max}} d\omega \left| \varepsilon^{\parallel}_{eff\,(theory)}(\omega) - \varepsilon^{\parallel}_{eff\,(\exp)}(\omega) \right|^2 \ , \tag{3.17}$$

$$Q_{\perp}(d,f) = \int_{\omega_{\min}}^{\omega_{\max}} d\omega \left| \varepsilon^{\perp}_{eff\,(theory)}(\omega) - \varepsilon^{\perp}_{eff\,(\exp)}(\omega) \right|^2 \ . \tag{3.18}$$

Ideally, if the metamaterial layer thickness and filling fractions are chosen correctly one expects $Q_{\perp}(d,f) = 0$ and $Q_{\parallel}(d,f) = 0$, meaning that consistency between the two components of the dielectric tensor is achieved via their underlying relation to the geometrical and optical parameters of the constituent materials. An obvious disadvantage of this algorithm is the necessity of knowledge of the dielectric constants of metal and host material used in the metamaterial sample. In our particular case, we could not apply the consistency algorithm as the optical data for the Tin Bismuth alloy in THz region is not available.

Finally, one can be tempted to use effective medium theory in the attempt to invert equations (3.15) and (3.16) in order to extract, for example, the permittivity of a semimetal alloy from the measured data. For example, from equation (3.16) it follows that:

$$\varepsilon_m = \frac{\varepsilon^{\perp}_{eff\,(theory)}(\omega) - (1-f)\varepsilon_{plastic}}{f} \ . \tag{19}$$

When trying to use this relation, especially in the case of low volume fractions where this relation is most applicable, one quickly finds that small measurement errors are greatly amplified by the f^{-1} factor, which renders the inversion algorithm practically unusable.

3.5.2 Nanostructured inclusions

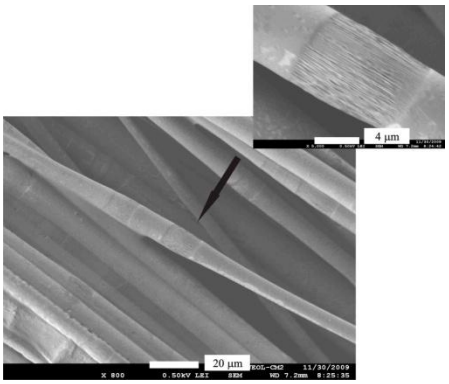

Fig. 3.10. Microwires after 2nd drawing featuring nanogrids. Microwires were obtained by dissolving PC polymer matrix. In the inset, shown is a pure Bi, Sn lamellar structure due to phase separation of an alloy.

We note in passing, that metallic wires made of multi-components alloys can exhibit an additional self-organized nanostructure. Particularly upon solidification, the metals of $Bi_{42\%}Sn_{58\%}$ alloy have been found to separate into different pure metal phases [116]. To illustrate this, Fig. 3.10 presents a scanning-electron-micrograph of the eutectic alloy wires obtained after two subsequent drawings. These wires were extracted from the composite by dissolving the PC cladding. On the wire surfaces one clearly sees formation of nanogratings. Stoichiometric studies using TOF-SIMS measurements (Time-of-Flight Secondary Ion Mass Spectrometry) showed that the lamellar structure on the surface of the individual wires is made of pure Bi (Bismuth) and Sn (Tin) parts.

3.6 Conclusion

This work presents an in-depth study of the challenges and practical issues encountered when trying to extract from the THz optical transmission data both the material and geometrical parameters of the deeply subwavelength wire arrays making a metamaterial film. Particularly, we detail a novel fabrication method for the large area THz metamaterial films using a two step fabrication process. First, we draw microstructured fibers containing ordered arrays of micro- or nano-wires made from either metal or dielectric materials. We then arrange such fibers parallel to each other and compactify them into a composite film by using a hot-press technique. Characterization of the THz transmission through metal wire composite films demonstrates

strong polarization sensitivity of their optical properties, promising application of such films as polarizers or high pass filters for THz radiation. Furthermore, composite films containing high refractive-index dielectric wires in place of metallic wires showed no polarization sensitivity, while the effective refractive index of such metamaterial films could be adjusted in a broad range. Using the transfer matrix theory, we then demonstrate how to retrieve the polarization dependent complex refractive index and complex effective permittivity of the metamaterial films from the THz optical transmission data. Finally, we detail the selfconsistent algorithm for the validation of such parameters as filling factor and thickness of the metamaterial layers by using an effective medium approximation.

CHAPTER 4
LABEL-FREE BACTERIA DETECTION USING EVANESCENT MODE OF A SUSPENDED CORE TERAHERTZ FIBER

4.1 Introduction

In this chapter the possibility of using THz fibers operating at wavelength longer than the size of the studied object is explored. Combination of high refractive index of the core (polyethylene) and the cladding (air) allows to significantly reduce the size of the probing evanescent tail. Thus it becomes possible to develop a label-free technique (target bacteria are not labelled or altered and are detected in their natural forms) based on the interaction between the evanescent wave, localized around the core of the fiber, and a thin layer of bacteria covering it. This technique is then used for the detection and quantification of the *E. coli* bacteria in the THz spectral range.

In addition, established measurement protocol allows measurement of the biological properties in the aqueous environment, while using THz waves that are normally unsuitable for this purpose because of the strong absorption of water. This so-called "frozen dynamics" approach allows all the biological processes to take place in water, while the system is robust enough to allow drying for THz measurements at the intermediate stage without affecting the biological subcomponents (such as phages).

4.2 Terahertz subwavelength fiber

The major complexity in the design of the terahertz waveguides is the fact that most dielectric materials are highly absorbing in this spectral region [92] with a typical loss in excess of ~1 cm^{-1}. To combat material losses, a novel approach based on the introduction of porosity in the fiber core has been recently introduced by our group [120]. We have proposed that since the absorption loss is lowest in dry air, one way to reduce waveguide propagation loss is to maximize the fraction of power guided in the air.

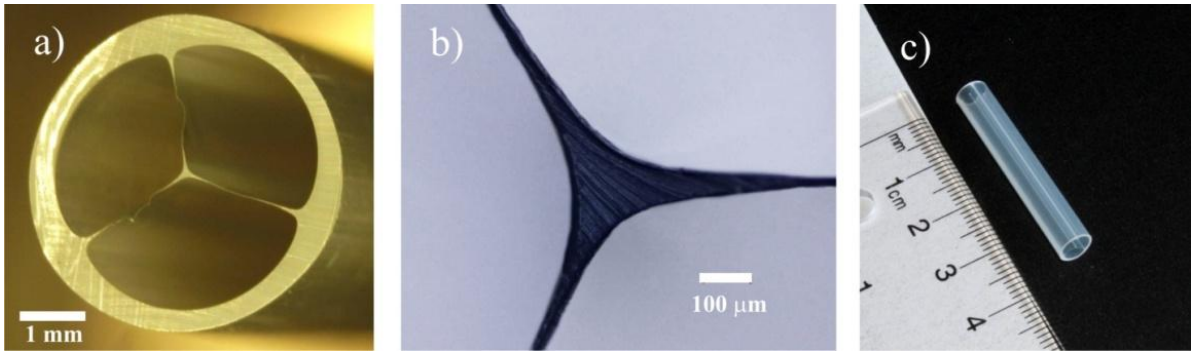

Fig. 4.1. (a, b) The THz fiber featuring a 150 μm core suspended by three 20 μm-thick bridges in the center of a 5.1 mm diameter tube, (c) 4 cm-long fiber piece used in the experiments.

One of the waveguides that operates on this principle was recently described in [9] and presents a subwavelength fiber suspended on thin bridges in the middle of a larger protective tube (see Fig. 3.1). Large channels formed by the bridges and a tube make a convenient opto-microfluidic system that is easy fill with liquid analytes or purge with dry gases. Particularly, the THz subwavelength waveguide used in our experiments features a 150 μm core fiber suspended by three 20 μm-thick bridges in the center of a 5.1 mm diameter tube (Fig. 4.1. (a, b)) of 4 cm in length. This waveguide design presents several important advantages for bio-sensing applications. First, the waveguide structure allows direct and convenient access to the fiber core and to the evanescent wave guided around it. Second, the outer cladding effectively isolates the core-guided mode from the surrounding environment, (*e.g.*, fiber holders), thereby preventing the undesirable external perturbations of the terahertz signal.

All the data in our experiments was acquired using a modified THz-TDS (Time-Domain Spectroscopy) setup. The setup consists of a frequency-doubled femtosecond fiber laser (MenloSystems C-fiber laser) used as a pump source and identical GaAs dipole antennae used as source and detector yielding a spectrum ranging from ~ 0.1 to 3 THz. Contrary to the standard THz-TDS setup where the configuration of parabolic mirrors is static, our setup has mirrors mounted on translation rails. This flexible geometry facilitates mirrors placement, allowing measurement of waveguides up to 45 cm in length without realigning the setup. Fig. 3.2 (a) illustrates the experimental setup where the fiber is fixed between the two irises and placed between the focal points of the two parabolic mirrors.

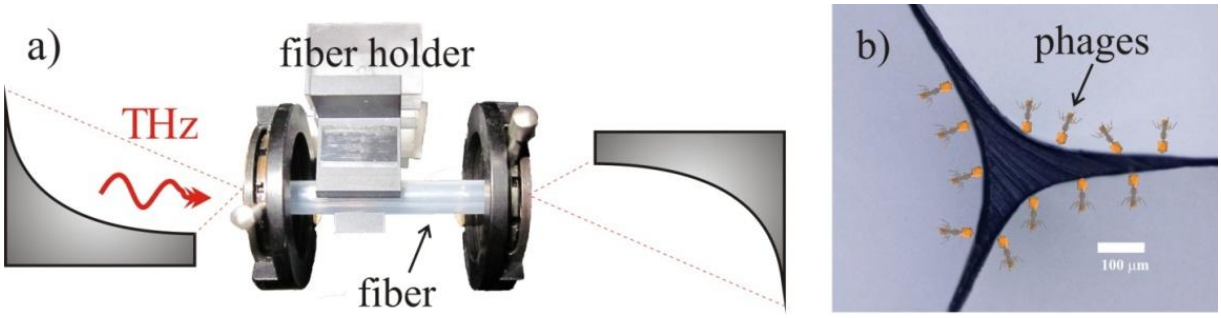

Fig. 4.2. (a) Schematic of the experimental setup: the fiber is placed between the focal points of the two parabolic mirrors, (b) schematic presentation of phages adsorbed onto the fiber core. The capsid adsorbed onto the fiber, while the tail (which is specific to the bacteria) faces towards the cladding for bacteria capturing.

4.3 Materials and methods

4.3.1 Bacteria culture

The bacteria solution was prepared as follows. A frozen stock of *E. coli* B strain was used to seed an overnight culture in LB media (liquid media for growing bacteria, contains 10 g Tryptone, 5 g yeast extract, 10 NaCl in 1L H_2O). Bacteria were harvested by centrifugation at 3000xg for 10 min, followed by washing in PBS (Phosphate Buffer Saline). Dilutions of the overnight culture were spread on LB agar plate to determine the titre, expressed in colony forming unit (cfu). Appropriate dilutions of bacteria stock with a concentration 10^4 – 10^9cfu/ml were made in PBS for subsequent experiments.

4.3.2 Phage production

100 μL of *E.coli* B log-phase culture was added to 3 ml cooled top agar and poured onto LB agar plate until solidified. 100uL of phage stock specific to *E.coli* B was added onto the solidified top agar and incubated at 37ºC overnight. A macroplaque was developed on the lawn of bacteria after incubation. 3 ml of lambda buffer was added onto the top agar, which is then scraped off and collected in a 50 ml centrifuge tube, followed by an additional washing of the LB agar plate with 3ml lambda buffer. 3 drops of chloroform were added into the suspension, vortexed and centrifuge at 3500xg for 10 min to pellet pieces of agar and bacteria. The supernatant was then passed through a 0.22 μm filter to remove the remaining bacteria. The filtrate is the stock phage solution and is prepared fresh for each experiment. The titre of the

phage stock was determined by serial dilution of the stock, followed by infection to E.coli as described above. Plaques were counted and the titre of the phage stock is expressed in plaque forming unit (pfu).

4.4 Characterization

The light propagating through an optical fiber consists of two components: the field guided in the core and the exponentially decaying evanescent field in the cladding. For evanescent sensing one typically removes the fiber cladding and introduces analyte into the immediate proximity of the fiber core [121]. In the presence of strong absorption or scattering in the analyte, the intensity of guided wave would decrease, which can then be then used to interpret various analyte properties. In application to THz evanescent sensing, both analyte refractive index and analyte absorption can be deduced by comparing the signals from the empty waveguide with that from the waveguide containing a layer of the measured material. By measuring the changes in both amplitude and phase caused by the addition of the analyte layer even very small amounts of analyte can be detected and characterized (see, for example, [122] where nanometer-size aqueous layers were characterized in THz) [123].

An immediate complication for evanescent biosensing in THz is that natural environment for a majority of bacteria is water and water is highly absorbing in THz spectral range. To avoid this problem, we have developed a protocol where all the bio-reactions take place in the natural aqueous environment, while the THz measurement is done on dried samples.

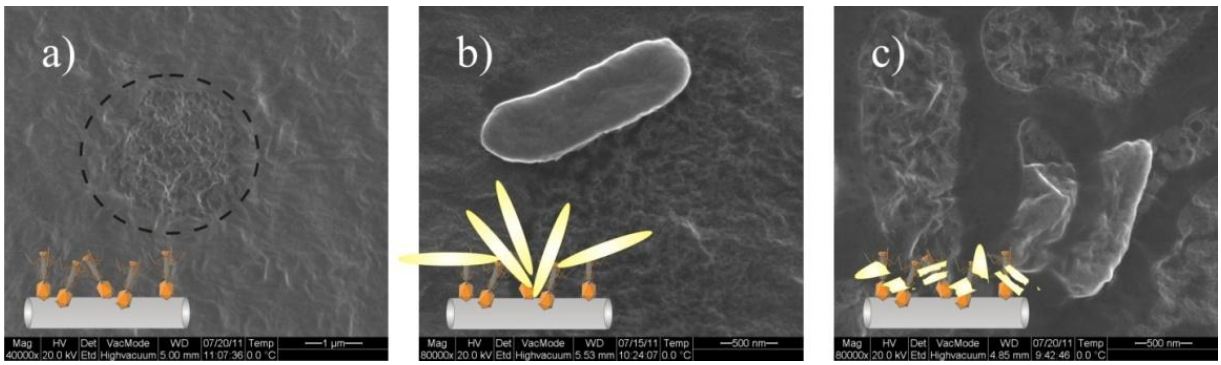

Fig. 4.3. SEM images illustrating each step of the experiment (a) step 1 – phages are immobilized on the fiber core surface, (b) step 2 – capturing of *E.coli* bacteria by the phages, and lysis of the bacteria, (c) step 3 – fiber is washed with PBS, bacteria chunks remain bound to the core surface.

In what follows all the SEM images were taken with a Quanta 200 FEG scanning electron microscope operating in high vacuum mode. First, the samples were fixed with formalin for 12 hours and then metalized with several nm-thick layer of gold.

To follow the dynamics of the bacteria binding we performed several experiments according to the three-step procedure described below. Before the measurement, the suspended core fiber (4 cm in length) was cleaned with isopropyl alcohol and distillated water. The fiber was incubated overnight (12 hours) with T4-bacteriophage solution at 10^{10} pfu/ml concentration. During this incubation, phages are adsorbed non-specifically onto the plastic fiber surface. The T4 phages recognize and bind to specific cell surface protein on the *E. coli* bacteria using their tail proteins (scheme of the process is shown at Fig. 4.2 (b)). This recognition is highly specific and has been extensively used for typing of the *E. coli*.

After phage adsorption the fiber was washed 3 times with distillated water and PBS. Only 10% of the fiber's bridges surface and core were covered by phages. The exposed fiber surface was therefore blocked with bovine serum albumin (BSA) for 30 min in order to reduce non-specific adsorption of the bacteria, and washed again with the buffer solution and dried out. Blocking with BSA is required because it is not possible to achieve 100% coverage of the fiber by the phages. Without BSA blocking, exposed fiber surface could cause non-specific adsorption of the bacteria and other components present in the sample, causing false positives.

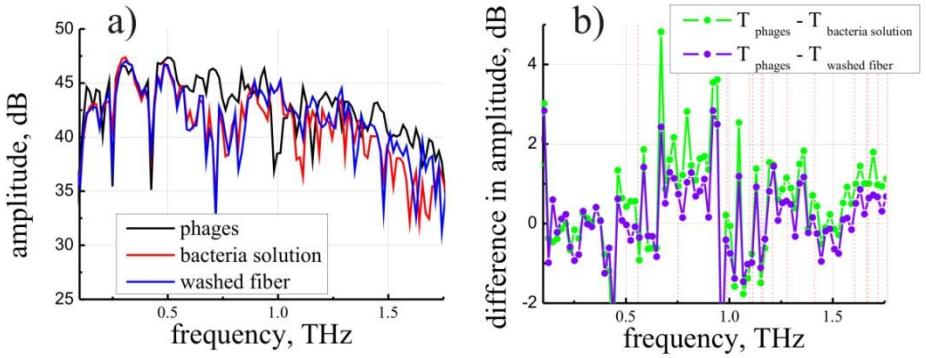

Fig. 4.4. (a) Transmission spectrum of the fiber during each step of the experiment: step 1 – black line, only phages, step 2 – red line, transmission of the fiber decreased due binding of E. coli bacteria to the phages, step 3 – blue line, fiber is washed with PBS. Fiber transmission is increased but not up to the level of the first step, suggesting that some bacteria (or parts of it) remain bound to the fiber via specific interaction with the phages. (b) Difference in transmission between each step of the experiment.

SEM imaging was performed to confirm the adsorption of the phages onto the fiber core as well as the stability of the phage layer, and the extent of fiber surface coverage. Fig. 4.3 (a) illustrates phages adsorbed onto the fiber (dark spots within the area define by dashed line). At the same time, THz transmission through the fiber was measured. The fiber transmission spectrum is shown in Fig. 4.4 (a − black line).

After the addition of the bacteria and subsequent binding of the phage on the bacterial surface, the phage infection process will start. The phage progeny will accumulate and eventually the bacteria host is ruptured followed by the release of the phage. The period between infection and bacteria lysis is known as the latent period and usually last for 25 minutes. The second measurement of the THz transmission through the fiber was done during the first 15 min after the introduction of bacteria (Fig. 4.4 (a − red line)). It could be clearly seen that the transmission of the fiber decreases considerably due to binding of the bacteria to the phages. A zoom-in of the waveguide core after some reaction time ~5-10 min is shown in Fig. 4.5. There, the dashed line circumscribes the part of a core covered with the bacteriophages; *E. coli* Bacteria are clearly visible bound to the region covered by the phages and not to the rest of the core surface blocked with BSA.

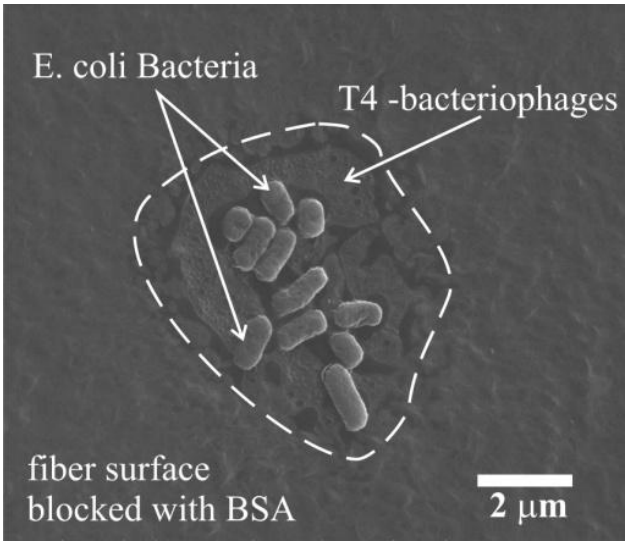

Fig. 4.5. Zoom-in of the waveguide core, dashed line marks the area covered with the bacteriophages. Bacteria are clustered in the phage-covered surface with the rest of the surface blocked by BSA.

In the last step, after 25 min of reaction time, the fiber was washed with the PBS in order to remove the unbound bacteria on the fiber surface and then again dried out. Fiber transmission (Fig. 4.4 (a − blue line)) increased compared to the previous step, but not up to the level of the first step, suggesting that some bacteria (or parts of them created by lysis and rapture) remain bound to the fiber via specific interaction with the phage.

The following SEM images (Fig. 4.6) were prepared at different moments of time during the process of specific recognition and binding of the *E. coli* bacteria with phages in order to understand the process that take place during the last 10 min of the 2nd step of the measurements.

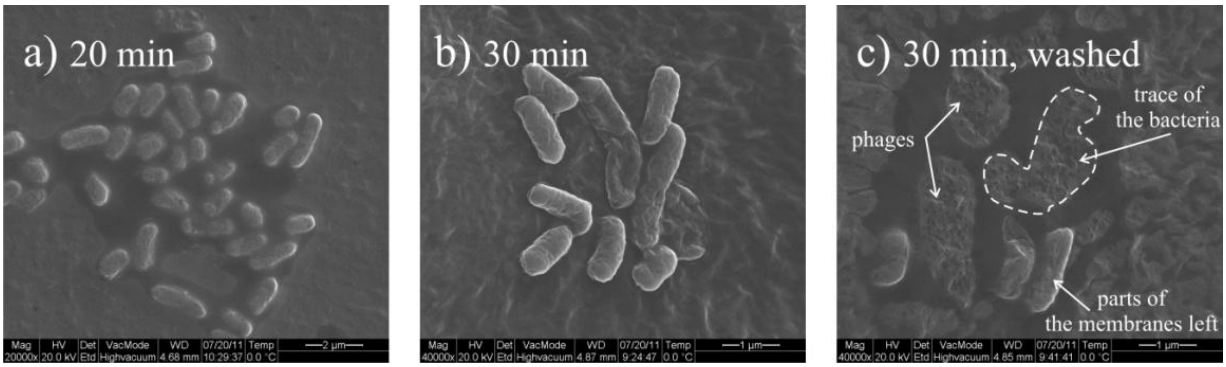

Fig. 4.6. SEM images of the fiber core (a) after 20 min since the beginning of the 2nd step; (b) after 30 min before washing with PBS (end of the 2nd step); (c) after 30 min after washing with PBS. The bacteria shape changed from a uniform rod shape to a random shape. Eventually, the bacteria cell wall ruptures and releases intracellular components with only the cell membrane left on the fiber.

Fig. 4.6 (a) shows fiber core after 20 min of interaction of *E. coli* bacteria with the phages. The bacteria are bound to the phages and have well defined rod shapes. Fig. 4.6 (b) shows the fiber core at the end of the 2nd step, after 30 min of bacteria interaction with pages. It is clearly seen that by the end of the 2nd experiment the bacteria change its shape form the rod-like to a highly distorted rod shape which is a result of bacteria lysis. During lysis the bacteria cell wall is eventually ruptured and releases intracellular components with only the cell membrane left on the fiber. Fig. 4.6 (c) illustrates the core of the fiber after 30 min of interaction of the bacteria with the phages and after washing with PBS. After the fiber was washed, traces of the bacteria

(membrane fragments) can be clearly seen still bound to the phages. Visually, washed fibers corresponding to Fig. 4.6 (c) look cleaner than the same fibers before washing.

In order to explain the considerable increase in the fiber transmission loss due to bacteria binding (during the course of the 2^{nd} measurement) we note that the *E. coli* largely consists of water. Therefore, it is expected that its mobilization on the core surface would lead to a significant loss increase due to water absorption. Particularly, cell dry weight ("dry weight" is the remaining material after all the water is removed) of the *E. coli* bacteria is only 30% and can be subdivided into protein (55%), RNA (22.5%), DNA (3.1%), lipids (9.1%), peptidoglycan (2.5%), polysaccharides (3.4%) and Glycogen (2.5%), while remaining 70% of the bacteria weight is water [124]. Additionally, we expect that the presence of the large and irregular bacteria clusters on the fiber surface would lead to scattering loss.

Similarly, after washing the fiber at the end of the 2^{nd} measurement, the fiber transmission is expected to increase as only the dry chunks of bacteria membrane remain on the surface. Moreover, their surface coverage is smaller than this of the bacteria before washing, therefore scattering loss is expected to be smaller in washed fibers. For completeness, we note that the outer membrane of the gram-negative bacteria such as *E. coli* is a complex structure composed of phospholipids, proteins, and polysaccharides that controls the permeability and helps maintain the shape and rigidity of the cell. The protein complement of the outer membrane includes a Murein-lipoprotein that is one of the most abundant proteins in bacteria: there are about $7.2\ 10^5$ molecules per cell.

Finally, we have observed that there are two spectral regions in the vicinity of 0.7 THz and in the range of 1.5–2.0 THz where the changes in the fiber absorption are especially pronounced. These particular spectral regions of high sensitivity were consistently identified in each of the several repetitions of our experiments. The physical nature of high absorption in these spectral regions is still unclear to us, while there is an indication that it can be related to spectral signatures of specific macromolecules abundant in the *E. coli* bacteria composition. In particular, in the THz spectral range large tandem repeats peptides or nucleosides have some observable spectral features, whereas nonperiodic biological molecules such as DNA and proteins have relatively featureless spectra [68]. Optimal regions for the THz detection of the *E. coli* bacteria found in our work correlate with the position of the absorption peaks of the Murein-lipoprotein or

Broun's lipoprotein (BLP), that is one of the most abundant proteins in bacteria [124, 125]. Additionally, there is a 0.68 THz absorption peak of Thioredoxin protein which is a commonly occurring electron transport protein in a bacteria. For the sake of clarity we also note that all the measurements were done in a nitrogen purged cage at 12% of humidity, therefore all the narrow dips in the transmission spectrum as observed in Fig. 4.4 (for example the 0.752 THz peak) are caused by the water vapour [126-128], which has to be distinguished from the broad absorption features due to bacteria.

4.5 Results and Discussion

In this section we present and interpret the changes in the fiber absorption loss during the bacteria binding process. Fiber absorption loss is defined as $\alpha = -\ln\left(P/P_{ref}\right)/L$ where L is the fiber length, P_{ref} is the transmitted power through the setup without fiber, and P is a transmitted power through the setup with fiber. To see the influence of bacteria binding on the THz transmission of a suspended core fiber in dynamics we measure the absorption loss of the fiber (with a dry sample) as a function of time. Particularly, during each step of the experiment we did at least 10–15 scans of the transmitted spectrum (one scan takes ~1 min). As a result, we have absorption losses of the fiber as function of time. Also, as it was mentioned before, the THz measurement is done with dried samples, while the bio-reactions take place in the natural aqueous environment. In particularly, after the 1st step of the experiment, the fiber was incubated with bacteria aqueous solution and then after 15 min (during this time phages have already captured bacteria) the fiber was dried out for transmission measurements. This results in a ~15 min gap in the sensorgram where it was impossible to measure losses due to high water absorption in THz spectral range.

Figure 4.7 illustrates the effect of the bacteria binding on the THz transmission of a suspended core fiber at 0.7 THz. First the reference sensorgram was acquired (Fig. 4.7 (a)) for which the fiber was prepared exactly the same way as described in the characterization section. However, no phages were used (phage solution was simply substituted with buffer during the 1st step), while the fiber surface was blocked with BSA to prevent non-specific bacteria binding to the core surface. The absorption loss returned to the initial level after bacteria were washed away with PBS. This transmission measurement and SEM images (not showed here) prove that the

fiber surface was indeed blocked with bovine serum albumin and no non-specific adsorption of the bacteria took place on the fiber surface.

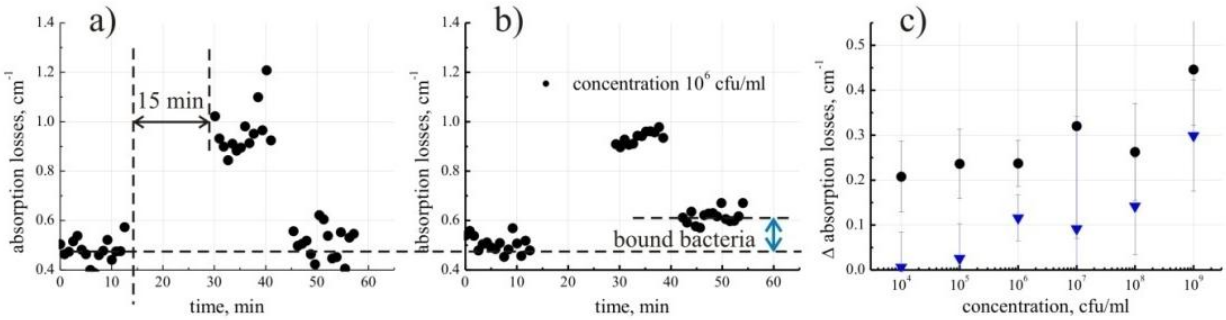

Fig. 4.7. Absorption losses of the fiber. (a) reference sensorgram; (b) sensorgram for bacteria concentration at 10^6cfu/ml as a function of time; (c) Correlation between the changes in the fiber absorption losses and bacteria concentration: difference between base level (absorption losses of the fiber with phages immobilized on the fiber core) and losses of the "washed" fiber is shown in blue triangles, as a function of a concentration. Black dots correspond to the difference between absorption losses of the fiber after 2nd and 3rd steps (before and after fiber washing).

In Fig. 4.7 (b), results of the experiments with phages are presented where despite extensive washing, some bacteria are always retained by specific binding to the phage-coated fiber, and as a consequence, fiber absorption loss does not return to the original level. More importantly, we are able to show the correlation between the fiber absorption losses and the bacteria concentration of the samples, further suggesting the specificity of the detection method. Thus, in Fig. 4.7 (c) the difference between the base level (absorption losses of the fiber with phages immobilized on the fiber core) and losses of the "washed" fibers are shown in blue triangles, as a function of bacteria concentration in the solution used during the 2nd experiment. Also, in black circles we show difference between absorption losses of the fiber after 2nd and 3rd steps (before and after washing of the fiber). This difference is related to a signal due to both specific bacteria binding to the phages and nonspecific temporary adsorbed bacteria onto a fiber surface so by itself it cannot be used for sensing. From the presented data (blue triangles) we see that the detection of limit of this method is around 10^4 cfu/ml, which is comparable with existing commercially available methods [80]. The commercial methods usually employ antibodies (Abs) as recognition elements instead of bacteriophages. The production of the specific Abs, however,

is difficult, expensive and very time-consuming. Also, antibodies easily lose their activity when subjected to changing environmental conditions. Bacteriophages are alternative method of bacteria capture that offer many advantages compared to antibodies. Particularly, phages are easy to produce in large quantities at a relatively low cost, they have long storage life and unlike antibodies can be physically adsorbed onto the fiber surface.

Considerable sensitivity enhancement of our method is possible by increasing the amount of the initial phage coverage of the fiber surface by better anchoring the phages via covalent immobilization onto the fiber surface, rather than physical adsorption. This however implies considerable effort in fiber surface biofunctionalisation chemistry which is beyond the scope of this paper.

4.6 Simple theoretical model to explain changes in the fiber absorption loss

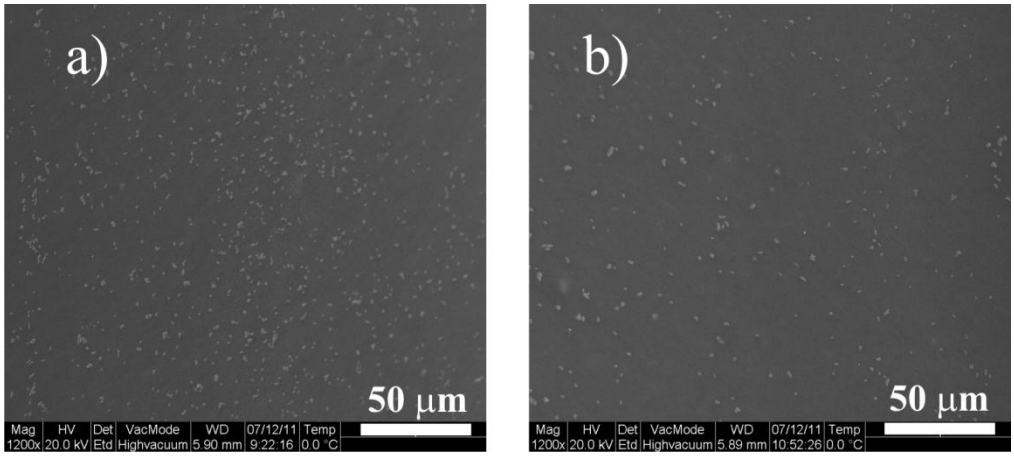

Fig. 4.8. SEM images of the fiber core with bacteria concentration of (a) 109 cfu/ml and 10 min interaction time (b) with a concentration of 10^6 cfu/ml, 10 min interaction time.

We believe that strong changes in the fiber transmission loss during the 2nd phase of the experiment (before washing the fiber) can be explained by the presence of water containing bacteria on the fiber core due to non-permanent adsorption or sedimentation during rapid drying of samples. As seen in Fig. 4.7 (c) these losses are proportional to the bacteria concentration. Moreover, from the direct observation of the SEM images, bacteria coverage of the fiber core is also proportional to the bacteria concentration. For example, at 10^9 and 10^6 cfu/ml, the average

coverage was correspondingly 4.35% and 1.52% (Fig. 3.8. (a, b). These values were achieved after analyzing presented SEM images via custom LabVIEW software. First we determined the ratio of the area covered with the bacteria (in pixels) to the total area of the picture in percentage. At the same time the total number of the bacteria in the field of view was also counted, which divided by the area of the SEM image yields the coverage ratio of 45 cells/100 μm^2 for the concentration 10^9 cfu/ml and 15 cells/100 μm^2 for the concentration 10^6 cfu/ml. Despite the fact that at concentration 10^9 cfu/ml we have 1000 times more bacteria then at the concentration 10^6 cfu/ml, we do not have any significant increasing of the bacteria coverage ratio due to limitation of the initial phage coverage of the fiber surface (only 10%) and number of phages required for the bacteria binding and subsequent lysis. As we will see in the following, it is the presence of the water containing bacteria on the fiber surface that leads to strong increase in the fiber absorption before washing. After washing, only dry bacteria chunks remain bound at the fiber surface and, therefore, fiber loss decreases. Thus, the additional loss after washing is most probably due to scattering on the bacteria remains.

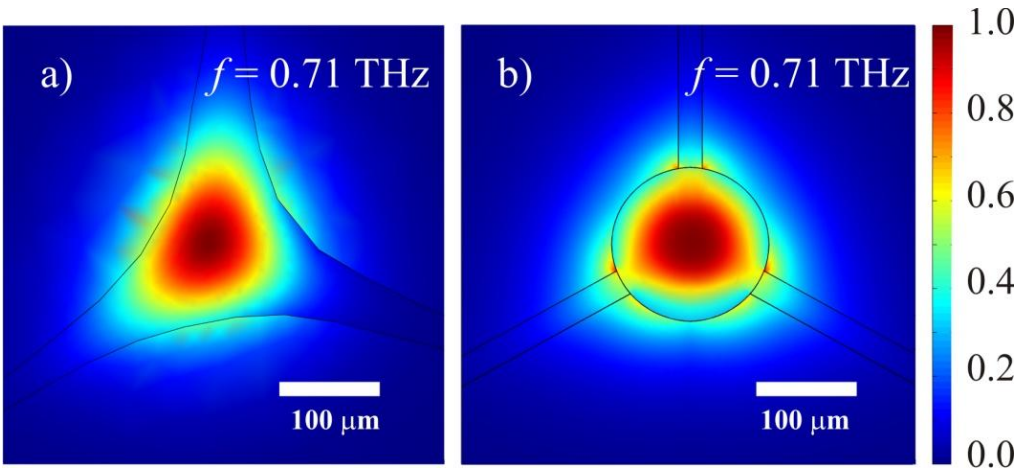

Fig. 4.9. Transverse distribution of power flow for the fundamental mode of (a) the real waveguide and of (b) the simplified design of the waveguide profile. The field is confined in the central solid core and is guided by total internal reflection.

To create a theoretical model of the experiment we first studied the modal structure of our fiber. We started by importing the fiber cross-section as captured by the optical microscope Fig. 4.1. (a) into COMSOL Multiphysics Finite Element software. The complex effective refractive indices and field profiles of both core guided and cladding modes were then studied.

Then, the power coupling coefficients were computed from the overlap integrals of the modal fields with those of the Gaussian beam of a source as described in [9]. The inspection of the coupling coefficients confirms that the fundamental mode is predominantly excited in the 0.2 – 2.0 THz frequency range. The transverse distribution of the longitudinal power flux in the fundamental mode of a fiber at 0.71 THz is shown in Fig. 4.9 (a) and a typical penetration depth of the evanescent field into the air cladding is determined to be $25\pm5\,\mu\text{m}$ which is in good agreement with a theoretical estimate $\lambda\Big/\left(4\pi\sqrt{\varepsilon_{core}-\varepsilon_{cladding}}\right)_{0.71THz}\approx 29\,\mu\text{m}$.

Next, absorption losses of a suspended core fiber with a bacteria layer have been investigated numerically using COMSOL. The simplified fiber geometry has been used to facilitate the task of distribution of bacteria on the core and characterization of the bacteria coverage ratio. We have reduced the transverse shape of the core to a circle and we have assumed that the bridges are straight and of constant width. The values of the waveguide core radius and the bridges width were chosen to make the changes in the effective refractive index, the absorption losses and the modal size minimal compared to the microscope imported design, and, hence, for simulation we used $D_{core}=175\,\mu\text{m}$ and $d_{bridges}=30\,\mu\text{m}$.

E. coli are typically rod-shaped, about 2.0 μm long and 0.5 μm in diameter. To simulate bacteria we have approximated their shape as an infinite cylinder of diameter $d_{bacteria}=1\mu\text{m}$. positioned along the fiber length. Considering that bacteria are mostly made of water (70% by total wet wt. [124]) we considered their refractive index and losses as those of the bulk water. The complex dielectric permittivity of water has been calculated using the full Rocard-Powles-Lorentz model with the parameters taken from [129]. For 0.71 THz the water refractive index is 2.19+0.65*i* resulting in absorption loss of 191 cm^{-1}. For low density polyethylene the real part of the refractive is about 1.514 in THz frequency range and the material loss are computed from the measurements [130]: $\alpha[cm^{-1}]=0.75\nu^2-0.1\nu+0.2$ where ν is the frequency in THz.

From the SEM images of the fiber surface with bacteria (see Fig. 4.8) we see that bacteria are randomly positioned on the core surface with relatively low concentrations. To take this into account in our simulations water cylinders (bacteria) were randomly distributed (see Fig. 4.10 (a)) on the fiber core surface with a fixed value of a coverage ratio (*i.e.*, the core's surface occupied by the water cylinders to the overall core's surface). Then, the fundamental

mode and its losses were found using FEM software, and the modal losses were then averaged over 10 random bacteria distributions.

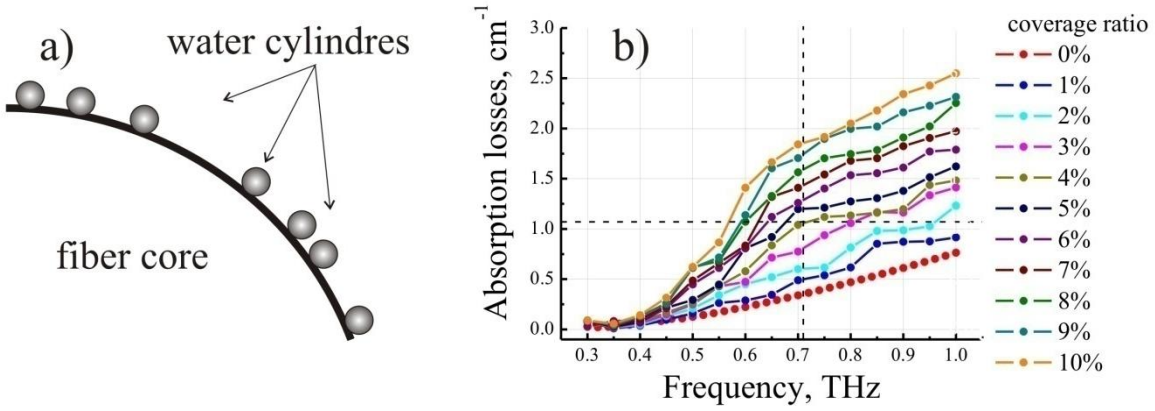

Fig. 4.10. (a) Randomly distributed 1 μm water cylinders on the waveguide core's surface for a given value of surface coverage. (b) Absorption loss of the fundamental mode for the fiber with a bacteria layer as a function of the bacteria coverage ratio. The crossing of the dash lines in the figure corresponds to the experimentally measured value of the propagation losses minus the theoretically estimated coupling loss for the 10^9 cfu/ml concentration of bacteria.

In Fig. 4.10 (b) we present the calculated propagation losses of the fiber fundamental mode as a function of the bacteria coverage ratio. We observe that the increase in the bacteria coverage ratio leads to a linear growth of the modal absorption losses. Due to much higher absorption losses of water compared to those of a polyethylene core, even a small coverage ratio of the bacteria results in large increase in the modal absorption loss. As an example, in Fig. 4.10 (b) we show at the intersection of the dashed lines the case of bacteria of concentration 10^9 cfu/ml that corresponds to the experimental fiber loss of ~1.2 cm^{-1} at 0.71 THz. Our theoretical analysis predicts that this loss is produced by the absorption loss of the fundamental modes due to 4% coverage ratio of water on the core's surface multiplied by the modal coupling coefficient from the Gaussian beam to the fundamental mode, which corresponds well with the experimental value of the bacteria coverage ratio 4.35% found from the SEM observations

Another important feature found in Fig. 4.10 (b) is an observation that for a given water coverage ratio, fiber absorption loss is small at low frequencies, then shows a rapid increase in the vicinity of 0.5 THz, and, then, at frequencies above 0.7 THz it simply follows the absorption loss of the polyethylene material with an almost constant loss contribution from the water layer.

This is easy to rationalize by noting that at low frequencies (< 0.3 THz in our case) the mode of a subwavelength fiber is strongly delocalized, and, therefore, its presence in the thin water layer around the core is minimal. When frequency increases (~0.5 THz in our case), the fiber mode shows rapid localization in the vicinity of a core region, and, therefore, its relative presence in the water layer and, hence, losses also rapidly increase. This also explains why in Fig. 4.4, there is little difference in the measured transmission losses of bare and bacteria activated fibers at frequencies below 0.5 THz. Finally, at even higher frequencies (above 0.7 THz in our case) the fundamental mode becomes mostly localized in the fiber core of radius R with a small fraction of power in a thin layer (of thickness d) on the core surface being $-d\Big/\left(\nu^2 R^3\right)$. Here we assume that the layer thickness is smaller than the evanescent field penetration depth into the air cladding $d < \lambda\Big/\left(4\pi\sqrt{\varepsilon_{core}-\varepsilon_{cladding}}\right)$, which is a true assumption all the way up to 10 THz. Considering that the bulk absorption loss of water increases $-\nu$ with frequency [126-128] we conclude that at higher frequencies absorption loss contribution due to a small water layer on the fiber surface becomes a slowly decreasing function of the operation frequency $-d\Big/\left(\nu R^3\right)$, compared to the $-\nu^2$ behavior of the fiber loss due to polyethylene absorption (see Fig. 4.10 (b)).

4.7 Conclusion

We demonstrate the possibility of using suspended core (d=150 μm) polyethylene THz fibers for sensing of the *E. coli* bacteria with detection limit of 10^4 cfu/ml. The structure of the suspended core fiber allows convenient access to the fiber core and to the evanescent part of the guided wave. The outer cladding effectively isolates the core-guided mode from interacting with the surrounding environment such as fiber holders and humid air, thus making the fiber convenient to handle and to operate.

It was shown that selective binding of the *E. coli* bacteria to fiber surface bio-functionalized with specific phages unambiguously influences the THz transmission properties of the suspended core fiber. Moreover, changes in the fiber absorption loss can be correlated with the concentration of bacteria samples. Thus, our setup allows not only detection of the *E. coli*, but also quantitative measurement of its concentration. Presented bacteria detection method is label-free and it does not rely on the presence of any bacterial "fingerprint" features in the THz spectrum.

A simple theoretical model was also developed in order to explain observed changes in the fiber absorption losses. It was found that the strong increase in the fiber loss can be explained by absorption of a thin water layer corresponding to the bound bacteria.

.

CHAPTER 5
THIN CHALCOGENIDE CAPILLARIES AS EFFICIENT WAVEGUIDES FROM MID-IR TO THZ

5.1 Introduction

In this chapter we investigate low-loss chalcogenide capillary-based waveguides that operate both in the mid-IR and THz spectral ranges. By exploiting the outstanding performance of chalcogenide glasses in the mid-IR and THz spectral ranges one can envision building fiber-based THz light sources with pumping in the mid-IR.

5.2 Glass synthesis and capillaries fabrication

The capillaries in this work are drawn under pressure from the chalcogenide glass melt by using a double crucible drawing technique [105, 106]. The wall thickness of the glass capillary is controlled during drawing using temperature and pressure, thus allowing fabrication of very thin capillaries with wall thickness, ranging in the 12 μm (Fig. 5.1 (b)) –130 μm (Fig. 5.1 (a)).

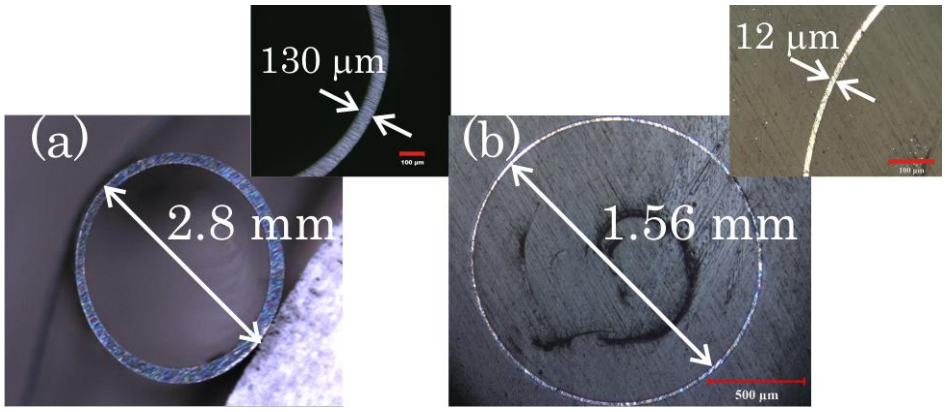

Fig. 5.1. Fabricated chalcogenide glass capillaries with different wall thickness in the range of (b) 12 μm to (a) 130 μm by double crucible glass drawing technique. To perform an imaging of thin wall capillaries, such as capillary with 12 μm walls shown at (b), they were glued in epoxy and then polished.

Chalcogenide glasses are typically synthesized from pure chemical elements, where bulk samples of vitreous arsenic chalcogenides of optical grade are produced by solidification of the

glass forming melt [131]. We here use $As_{38}Se_{62}$ glass. This composition was chosen because of its higher stability against crystallization during the drawing compared to As_2Se_3. An 80 g glass preform was prepared from the pure materials (Se: 99.999% 5N and As: 99.999% 5N). The compounds are introduced in a chemically cleaned and dried silica ampoule. The ampoule was then evacuated using a diffusion vacuum pump to the pressure of 5×10^{-7} mbar and placed into a rocking furnace where the glass is melted at temperatures above 600°C. In the next step, the glass is first slowly cooled down to 450°C and then quenched in cold water in order to solidify the glass forming-melt. The obtained glass rod is then annealed overnight under a temperature close to the glass transition temperature T_g (T_g = 165°C) so as to reduce inner stress caused by the quenching. The chalcogenide glass rod then removed from silica ampoule and inserted into the quartz-based double crucible.

Traditionally, the double crucible set-up is used to draw step index fibers in which both volumes of the double crucible contain core and clad glasses with different refraction indices (i.e. different chemical compositions) in order to yield either a multimode or single-mode fiber, depending on the core size in the final fiber [131]. A schematic of our drawing tower with the double-crucible method is presented in Figure 5.2. In our case, the volume of the crucible designed for the fiber core remains empty while the clad crucible contains the synthesized $As_{38}Se_{62}$ glass. The entire chamber with the double crucible is purged at 50°C overnight with a constant flow of N_2 to avoid O_2 and dust particles in the heated zones.

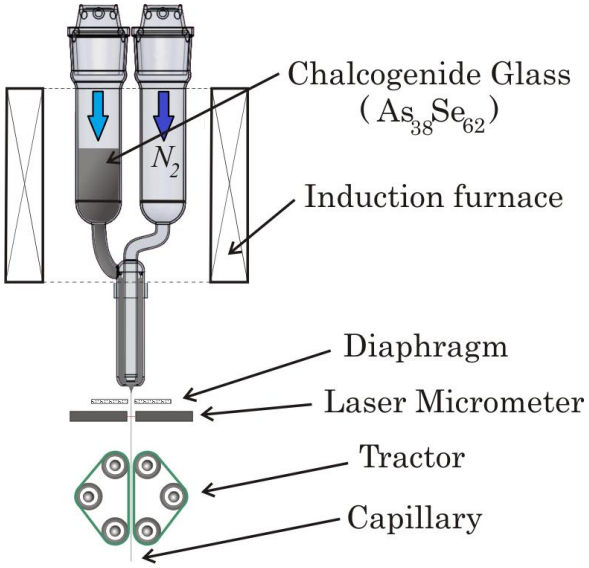

Fig. 5.2. Set-up for drawing capillaries using the double-crucible method.

The temperature slowly increases from the bottom to the top of the crucible. In the higher zone, at 400°C the glass starts to melt and flows down to the cooler zones (~295°C) along the crucible, thus the viscosity of the melt in the lower zones is higher which enables us to have a slower and more controllable flow. At the tip of the double crucible, a drop of glass is formed and as it goes down by gravity, the fiber is drawn like in a conventional fiber drawing tower. As soon as the drop reaches the tractor, it is pulled down with a controlled speed; meanwhile the pressure in the core crucible is increased in order to form a capillary. By varying the drawing conditions such as tractor speed and pressure in the core, numerous dimensions of capillaries and wall thicknesses have been obtained.

In case of capillaries with thin walls (around 20 μm), the mechanical stability of the drawn fiber can sometimes be low. If the walls of the capillary are very thin, they can be easily crushed due to squeezing within mechanical parts of the tractor during the fabrication or later with fingers. For the capillaries with the outer diameter of 2 mm and wall thickness 80 μm the minimal bending radius is around 15 cm, which demonstrates good mechanical strength. However capillaries with thinner walls are still very fragile and are almost impossible to be bent.

5.3 Absorption loss of the $As_{38}Se_{62}$ glass

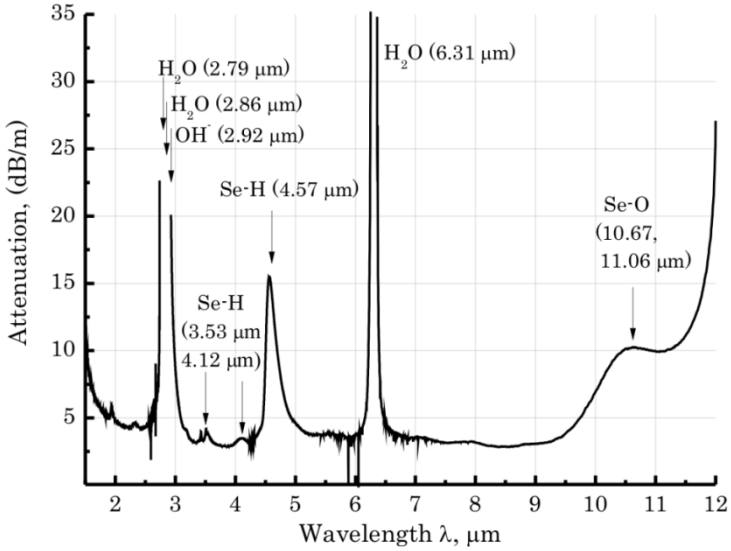

Fig. 5.3. Absorption loss of the $As_{38}Se_{62}$ rod with diameter 350 μm. Absorption bands in the 3–5 μm spectral range corresponds to impurity absorptions due to SeH bond at 3.53, 4.12, 4.57 μm. Also strong absorption bands at 2.7–2.93 μm and 6.31 μm are due to OH–group and water.

Figure 5.3 presents the absorption loss of the $As_{38}Se_{62}$ rod-in-the-air fiber with diameter 350 μm in the 1–12 μm spectral range obtained by the cut-back measurement from 1 m to 30 cm. The minimum of attenuation is about 2.89 dB/m at 3.85 μm. One can notice that the absorption bands due to hydrogen impurities (O-H and H_2O) are important compared with the Se–H band at 4.5 μm. Such impurities can be in principle removed by using standard static or dynamic distillation processes that requires complex glassware [131-133]. The increase of the optical losses in the 10–12 μm spectral region is usually explained by the effect of the oxygen impurity (Se-O, Arsenic oxides) [133-135].

In the mid-IR spectral range we have used Sellmeier fit of the real part of the refractive index versus wavelength [136]:

$$n(\lambda)=\left[1+\lambda^2\left(A_0^2/\lambda^2-A_1^2\right)+A_2^2/\left(\lambda^2-19^2\right)+A_3^2/\left(\lambda^2-4A_1^2\right)\right]^{-1/2}, \qquad (5.1)$$

where $A_0=2.234921$, $A_1=0.24164$, $A_2=0.34744$, $A_3=1.308575$ resulting in the values in the range 2.76 – 2.8. $As_{38}Se_{62}$ glass in the 2–12 μm range features a relatively small absorption losses 0.01 cm^{-1}, while showing complex and generally nonmonothonic growth of the absorption losses with the subsequent increase of the wavelength in the 4–18 THz spectral range.

The refractive index of the chalcogenide glass in THz spectral region was measured in house using THz-TDS setup. The real part of the refractive index was found to be nearly constant in the whole 0.1–2.5 THz range and its value is approximately 3.12. The imaginary part of the refractive index in the 0.1–2.5 THz spectral range was found to increase quadratically with frequency and can be estimated as $1.9\omega+50.9\omega^2$ where ω is the frequency in THz.

5.4 Results and discussion

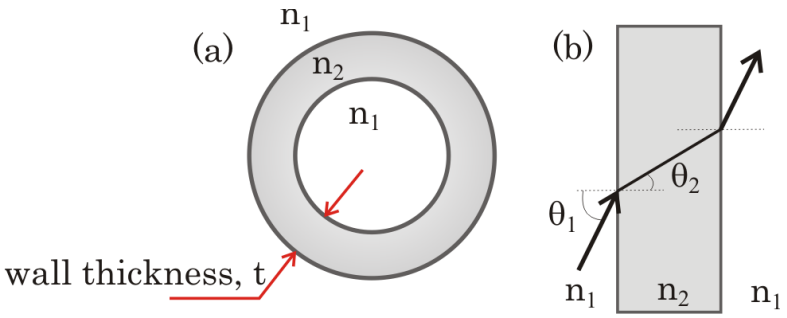

Fig. 5.4. (a) Profile of the capillary waveguide. (b) Fabry-Pérot etalon.

As we have mentioned earlier, the guiding mechanism of the leaky core modes in the capillary waveguide (chalcogenide glass tube) is similar to that of the antiresonant optical waveguides (ARROWs) [99, 100, 103, 104], and can be simply described by considering the capillary wall as a Fabry-Pérot étalon [Fig. 5.4 (a)–(b)]. Close to the resonance frequencies [Eq. (5.2)], there is almost no reflection from the tube walls and, consequently, light is not well confined inside the capillary. On the other hand, under the antiresonant condition considerable reflections at the inner side of the tube result in the strong light confinement (waves bounce back and forth inside of the capillary).

The resonant frequencies of the tube wall are given by the condition of the constructive interference between the multiple reflections of light between the two refracting surfaces of the wall [Fig. 5.4 (b)], where n_2 and n_1 denote the refractive indices of chalcogenide glass and air respectively, θ_1 and θ_2 are incident and reflected angles with respect to the interface normal respectively; t is the wall thickness of the capillary. Then, frequencies at which the tube wall becomes virtually transparent to the incident light are given by:

$$f_m = \frac{mc}{2 \cdot n_2 \cdot t \cdot \cos\theta_2} = \frac{mc}{2 \cdot n_2 \cdot t \cdot \sqrt{1-\left(n_1/n_2\right)^2}} = \frac{mc}{2 \cdot t \sqrt{n_2^2 - n_1^2}} \ , \tag{5.2}$$

where c is the speed of light in vacuum, m is an integer and we suppose that radiation angle of incidence is grazing ($\theta_1 = \pi/2$), which is true for the capillaries with diameters much larger than the wavelength of light. These resonances result in the appearance of the periodic minima in the capillary transmission spectrum. The bandwidth of the transmission windows is given by:

$$\Delta f = f_{m+1} - f_m = \frac{c}{2 \cdot t \sqrt{n_2^2 - n_1^2}} \ , \tag{5.3}$$

or in terms of wavelength:

$$\Delta\lambda = \lambda_m - \lambda_{m+1} = \frac{\lambda_m \cdot \lambda_{m+1}}{2 \cdot t \sqrt{n_2^2 - n_1^2}} \ . \tag{5.4}$$

The modal characteristics of the pipe waveguides have been also numerically investigated using full-vector transfer matrix theory and finite element method (COMSOL software). For each capillary the attenuation constants of the lowest 12 modes of the waveguide have been calculated.

The fundamental HE_{11} ARROW mode has the highest coupling coefficient with an incident linearly-polarized Gaussian beam and has the lowest attenuation constant. The resonance positions and the bandwidth of the transmission windows are the same for the fundamental and higher-order modes. Modal indices of the higher-order modes are somewhat lower than that of the fundamental mode. Within the ray-optics approach, this means that the higher-order modes propagate at a higher inclination angle (with respect to the propagation axis) than the fundamental mode; the modes with higher angles at the core-cladding interface incur larger attenuation constants. Also we note that the modes of a fiber only with angular momentum equal to 1 can be excited by the incoming (centered) Gaussian beam due to symmetry considerations. Finally, distribution of the transverse $E-$ field components $\bar{E}_{output} = \left(E^x_{output}, E^x_{output}\right)$ at the output facet of a fiber of length L_w is modeled as a coherent superposition of the $N = 12$ lowest loss guided modes:

$$\bar{E}_{output}(x,y,\omega) = \sum_{m=1}^{N} C_m \cdot \vec{E}_m(x,y,\omega) \cdot \exp\left(i\frac{\omega}{c} n_{eff,m} \cdot L_w\right) \cdot \exp\left(-\frac{\alpha_m L_m}{2}\right), \qquad (5.5)$$

where $\bar{E}_{output} = \left(E^x_{output}, E^x_{output}\right)$ stands for the transverse field components of the m-th guided mode. The variables α_m and $n_{eff,m}$ denote respectively the power loss coefficient and the real effective refractive index of the *m*-th mode at a given frequency ω. The variable C_m refers to the standard normalized amplitude coupling coefficients computed from the overlap integral of the respective flux distributions of the *m*-th mode with that of the input beam [7].

Transmission measurements were performed in two spectral ranges: in mid- IR from 1.5 to 14 μm by the Fourier Transform Infrared Technique (FTIR) using a modified ABB FTLA2000 Fourier transform IR spectrometer, and in THz spectral range from 0.1 up to 3 THz by a Terahertz Time-Domain Spectroscopy (THz-TDS) setup. The setup consists of a frequency-doubled femtosecond fiber laser (MenloSystems C-fiber laser) used as the pump source and two identical GaAs dipole antennae used as source and detector of a spectrum ranging from ~ 0.1 to 3 THz. Contrary to the standard THz-TDS setup where the configuration of parabolic mirrors is static, the utilized setup has mirrors mounted on translation rails. This flexible reconfiguration facilitates mirrors placement, allowing measurement of waveguides up to 50 cm in length without realigning the setup (for more details see [9]).

5.4.1 Capillaries in mid-IR spectral range

In the mid-IR spectral range, the dominant guidance mechanism is the anti-resonant reflection from the capillary walls with the highest fraction of power concentrated inside the hollow core.

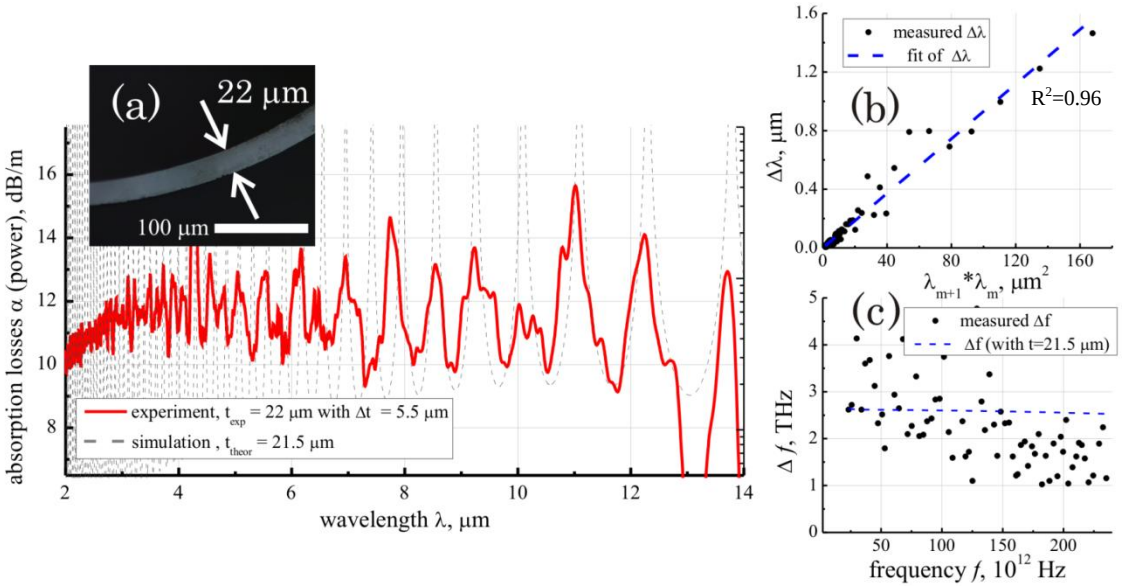

Fig. 5.5. (a) Absorption losses of capillary with 22 μm average wall thickness in spectral range from 2–14 μm, measured with the cut-back method. (b) Measured period of the resonances $\Delta\lambda$ as a function of product of two consecutive resonance wavelengths $\lambda_{m+1} * \lambda_m$ (μm^2) from Fig. 5.5 (a) of absorption losses. (c) Measured period of the resonances Δf as a function of frequency. Blue dashed line is the experimental fit of the resonances, which gives the wall thickness value of $t_{fit} = 21.2 \pm 4.8$ μm, which is in a good agreement with measured with optical microscope wall thickness $t = 22.1 \pm 5.5\,\mu m$.

Very thin chalcogenide capillaries with wall thickness below 25 μm and outer diameter 1–2 mm guide very well the mid-IR radiation with losses from 7 to 16 dB/m depending on the wavelength. Figure 5.5 (a) illustrates the absorption losses of capillary with average wall thickness of 22 μm in the spectral range from 2–14 μm, measured with cut-back method by FTIR technique. The results of the transfer matrix calculation for the fundamental mode are shown as a dashed line. The comparison of the theoretical results with the experimental data shows that for such capillaries the positions of the absorption minimums and the widths of the transmission

bands can be well described by taking into account only a single fundamental HE_{11} mode. Figure 5.5 (b) shows measured periods of the resonances $\Delta\lambda = \lambda_{m+1} - \lambda_m$ (difference between the two adjacent absorption loss maxima λ_{m+1}, λ_m) as a function of product of two consecutive resonance wavelengths $\lambda_{m+1} * \lambda_m$ (μm^2). Blue dashed lines in the figures 5.5 (b) and (c) are the theoretical fits of the experimental data using equations (5.3) and (5.4). From these fits we find that to explain position of the transmission minima capillary wall thickness has to have value of $t_{fit} = 21.2 \pm 4.8\,\mu m$ which is in a good agreement with measurements corresponding to the wall thickness retrieved with the optical microscope $t = 22.1 \pm 5.5$ μm (inset in the Fig. 5.5 (a)).

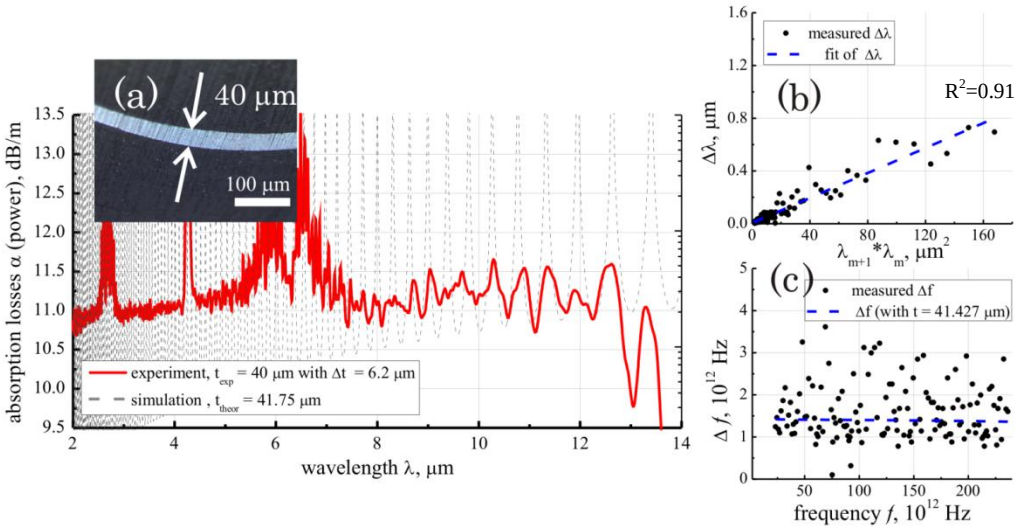

Fig. 5.6. (a) Absorption losses of the capillary with average wall thickness 40 μm in the spectral range 2–14 μm. (b) measured period of the resonances $\Delta\lambda = \lambda_{m+1} - \lambda_m$ (difference between the two adjacent absorption loss maxima λ_{m+1}, λ_m) as a function of product of two consecutive resonance wavelengths $\lambda_{m+1} * \lambda_m$ (μm^2) from Fig. 5.6 (a) of absorption losses. (c) Measured period of the resonances Δf as a function of frequency. Blue line is the experimental fit of the resonances, which gives the wall thickness value of $t_{fit} = 41.4 \pm 5.6\,\mu m$, which is in a good agreement with measurements via the optical microscope $t = 40.1 \pm 6.2$ μm

Figure 5.6 (a) illustrates absorption losses of capillary with average wall thickness of 40 μm within the spectral range from 2–14 μm. Compared to the thin capillaries, spectral oscillations in the transmission spectrum of the twice as thick capillary are much less pronounced, especially at shorter wavelengths. Weak oscillations are still visible between 8 and 13 μm. Figure 5.6 (b)

shows measured period of the resonances $\Delta\lambda = \lambda_{m+1} - \lambda_m$ (difference between the two adjacent absorption loss maxima λ_{m+1}, λ_m) as a function of product of two consecutive resonance wavelengths $\lambda_{m+1} * \lambda_m$ (μm^2) from Fig. 5.6 (a) of absorption losses, blue dashed lines are the experimental fit of the resonances, which gives a wall thickness value of $t_{fit} = 41.4 \pm 5.6$ μm, that is in good agreement with measurements with the optical microscope observation: $t = 40.1 \pm 6.2\ \mu m$ [inset of Fig. 5.6 (a)]. The absorption losses measured using capillaries samples are typically consistently higher than the losses of the rods of the same material. We believe that it can be explained by the surface roughness of the capillaries. The scales of this roughness and the nonuniformity of the capillaries wall thickness can be comparable with the wavelength causing the dissipation of the transmitted power.

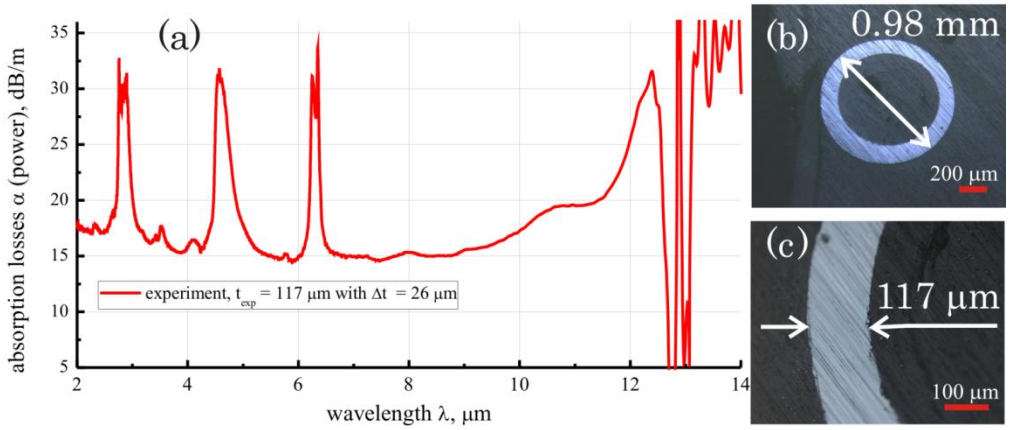

Fig. 5.7. (a) Absorption losses of the capillary in the spectral range 2–14 μm, it tends to show a featureless spectrum with ~15 dB/m losses. (b) and (c) optical micrographs of the capillary with outer diameter of 0.98 mm and averaged wall thickness 117 μm.

When using even thicker capillaries, the spectral contrast between minima and maxima in the mid-IR transmission spectrum decreases, and in very thick capillaries with wall thicknesses above 100 μm, the oscillations are not detectable with the FTIR technique.

Capillaries tend to show a featureless spectrum with ~15 dB/m losses. Figure 5.7 (a) illustrates absorption losses of the capillary 0.98 mm in diameter with average wall thickness 117 μm in the spectral range 2–14 μm [Fig. 5.7 (b), (c)].

5.4.2 Capillaries in the THz spectral range

In the THz spectral range, the thicker capillaries (~100 μm) show clear anti-resonant guidance with periodic minima and maxima as a function of frequency. Figure 5.8 (a) illustrates the transmittance through a 50 cm long capillary with wall thickness t = 98 μm and diameter 0.95 mm with total losses by power (coupling and transmission) ranging from 58 to 93 dB/m depending on the frequency.

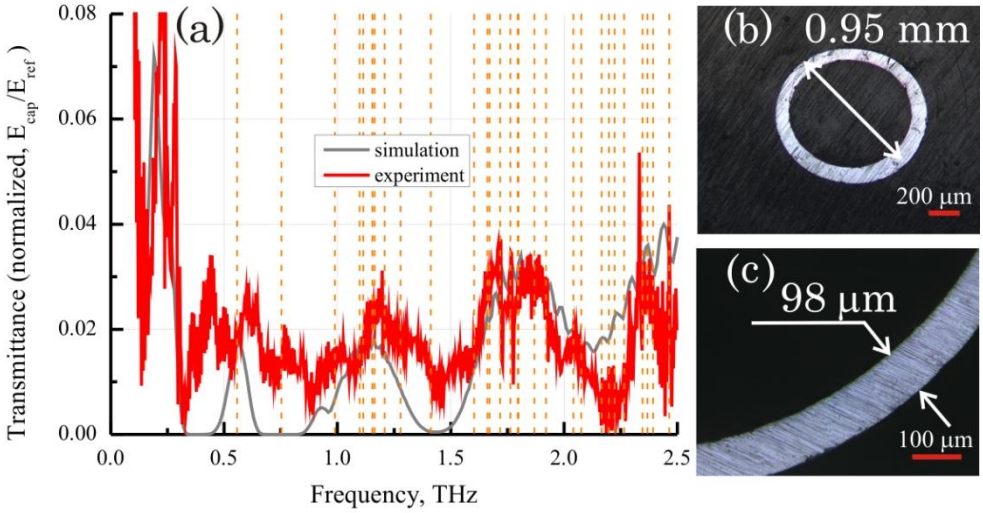

Fig. 5.8. (a) Transmittance by field of the effectively single mode 50 cm-long capillary with 98 μm average wall thickness and 0.95 mm diameter in the spectral range between 0.1 –2.5 THz. At lower frequencies (ω < 0.3 THz) guidance mechanism is of TIR type with losses ~44 dB/m, while at higher frequencies (ω > 0.3 THz) guidance is of ARROW type with total losses ranging in the 58 – 93 dB/m range depending on the operation frequency; (b) and (c) optical micrographs of the capillary used in the experiments with outer diameter of 0.95 mm and averaged wall thickness 98 μm .Orange dashed lines correspond to the positions of the water lines in the THz spectrum.

Numerical simulations show that a 50 cm-long chalcogenide capillary of 0.95 mm diameter and 98 μm thickness operates in the effectively single-mode regime, while higher-order modes contribute only to small oscillations in the fiber transmission spectrum due to their higher attenuation constants.

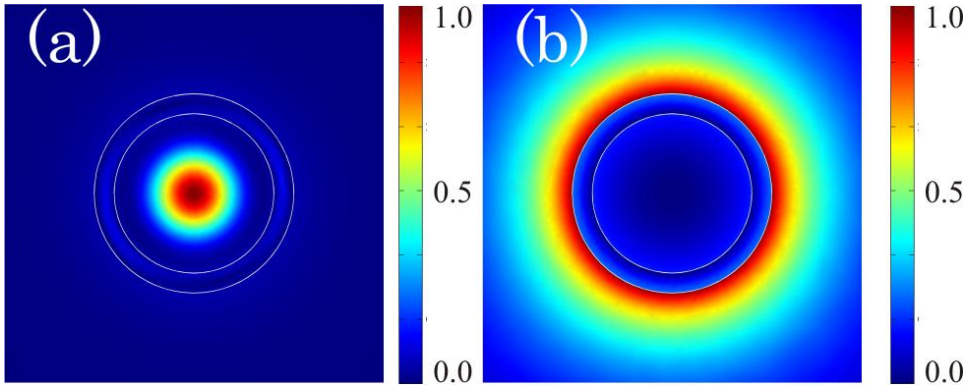

Fig. 5.9. Longitudinal energy flux distributions for (a) ARROW type fundamental (HE_{11} mode) in thick wall capillary (98 μm thickness, 0.95 mm diameter) at 0.57 THz, (b) total internal reflection (TIR) type mode guided by the deeply subwavelength capillary walls at 0.18 THz of the same capillary.

Particularly, at low frequencies (< 0.3 THz) the only guided mode supported by a capillary is a TIR mode where thin-walled capillary acts as a subwavelength waveguide (see Fig. 5.9 (b)). In this case capillary wall thickness is much smaller than the wavelength of light, while the capillary diameter is comparable or smaller than the wavelength of light. At higher frequencies (> 0.3 THz), the waveguide is again effectively single mode with the principal mode being the ARROW mode mostly concentrated in the fiber core (see Fig. 5.9 (a)). In this case, capillary wall thickness is comparable to the wavelength of light, while the capillary diameter is much larger than the wavelength of light. Longitudinal energy flux distributions for the ARROW and TIR modes computed at frequencies 0.57 THz and 0.18 THz are shown in Fig. 5.9 (a) and (b). The operation frequency for the ARROW mode is chosen to be in the center of a transmission band, so that the fiber fundamental mode power is confined almost entirely inside of the capillary hollow core (see Fig. 5.9 (a)). In contrast, the TIR mode is guided mostly outside of the capillary with only a small fraction of power inside the hollow core (see Fig. 5.9 (b)). The capillary wall thickness of 91 μm (compared to 98 μm measured thickness) was taken in numerical simulations for the best match of the positions of the transmission peaks with the experimental data. This difference can be explained by the non-uniformity of the capillaries, their average thickness can differ slightly from the value measured on its facets. Alternatively, it can be explained by an inaccuracy in measurement of refractive index of the chalcogenide glass. Both

these values are key parameters in the equation which defines the positions of minimal and maximal transmittance of the capillary when it guides through anti-resonant mechanism.

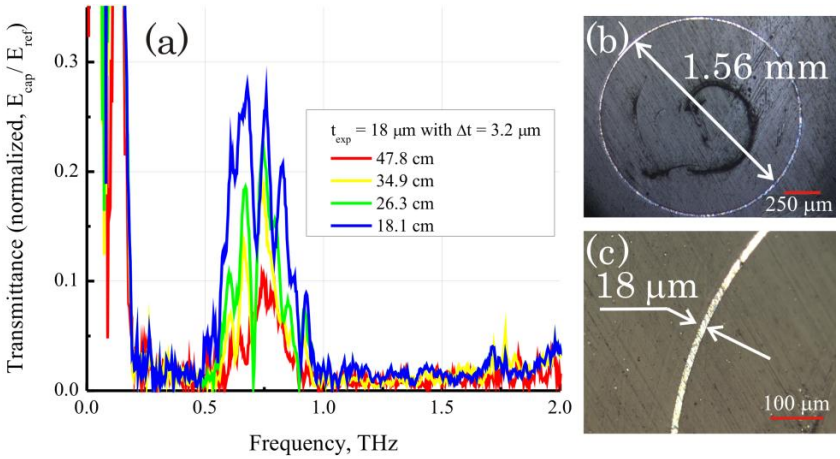

Fig. 5.10. (a) Transmittance of the capillary with average wall thickness 18 μm in the 0.1–2.0 THz spectral range with ~19 dB/m transmission loss at 0.75 THz. (b)–(c) photograph of the capillary used in the experiments with outer diameter of 1.56 mm and average wall thickness 18 μm .

Finally, even thinner capillaries (wall thickness < 20 μm) show a broad 0.5–0.9 THz transmission band [Fig. 5.10 (a)] that corresponds to the TIR mode guided by the deeply subwavelength capillary walls. In Fig. 5.10 (a) transmittance of the capillaries with 18 μm thick-walls is shown for various values of the capillary length (cut-back measurements). Capillary transmission losses are low (below 0.05 cm^{-1} / 19 dB/m at 0.75 THz) in the whole transmission window of 0.5–0.9 THz. Transmission measurements at different capillary length reveal the fine spectral structure, which could be a result of the structural imperfection of the capillary walls along the fiber length. The numerical simulations using transfer matrix method give a simple explanation to the spectral position of the transmittance peak of the TIR mode. It is simply a frequency at which the overlap between the TIR mode and incoming Gaussian beam (whose waist is proportional to the wavelength) is maximized.

5.5 Conclusion

In this work we have demonstrated that chalcogenide glass $As_{38}Se_{62}$ capillaries can be used as efficient waveguides covering the whole mid-IR–THz spectral range. The capillaries are fabricated using a double crucible glass drawing technique. The wall thickness of the glass capillaries can be well controlled during drawing by using temperature and pressure parameters, thus, enabling fabrication of the chalcogenide capillaries with wall thickness varying in a wide range of 12 μm to 130 μm. Such capillaries show low-loss transmission of the mid-IR and THz light. Particularly, in the mid-IR range, guidance is mostly governed by Fresnel reflections at the inner walls of the capillary and by the resonances in the capillary walls (ARROW guidance). Additionally, in the THz spectral range capillaries with deeply subwavelength wall canguide via total internal reflection mechanism.

GENERAL DISCUSSION

In the previous chapters I have reported experimental and theoretical results that were achieved within the three main research directions during my doctoral studies. In this section, I would like to clarify several specific questions regarding experimental setup, procedures, simulation methods and some other practical aspects that should be taken into consideration.

Signal processing in THz time domain spectroscopy

In this section, I explain the choice of the acquisition frequency in the temporal domain and the associated delay line displacement that allows avoiding spectral artifacts appearance.

To obtain the amplitude and phase information from the experiment, we measure current signal at the detector antenna which is proportional to $E_{THz}(t)$ using a mechanical delay stage and a lock-in amplifier. We record one point of data at each position of the delay stage, *N* points in total. This gives us a discretely sampled signal (measured point-by-point) with Δt being the time interval between the samples. For any sampling interval Δt, there is a special frequency $f_{\max}[THz]$ called the Nyquist critical frequency, given by:

$$f_{\max}[THz] = \frac{1}{2 \cdot \Delta t} = \frac{c}{2 \cdot 2 \cdot dx} \approx \frac{300[THz \cdot \mu m]}{4 \cdot dx[\mu m]}, \tag{5.6}$$

$$df[GHz] = \frac{1}{t_{\max} - t_{\min}} \approx \frac{300[GHz \cdot mm]}{2 \cdot \Delta x[mm]}, \tag{5.7}$$

where c is the speed of light, dx is the step size of the delay line and Δx is the total displacement. For the frequencies equal or below Nyquist frequency THz spectrum can be retrieved without the aliases caused by sampling.

Example of the THz electric field measured point-by-point in the time-domain $E_{THz}(t)$ and its Fourier transform $E_{THz}(f)$ are shown in Fig. 5.11. Figure 5.11 (a) presents the THz electric field $E_{THz}(t)$ as a function of the delay line displacement. Figure 5.11 (b) shows the THz electric field $E_{THz}(t)$ as a function of the associated recalculated time in picoseconds. For better visualisation of the step size dx, measured point-by-point in the time-domain with $N = 1024$ points, $\Delta t = 68.2\ ps$ and $dx = 10\ \mu m$ a zoom-in of the THz electric field $E_{THz}(t)$ is shown in

Fig. 5.11 (c). The Fourier transform of the time signal gives an amplitude $|E_{THz}(f)|$ with $f_{\max} = 7.5$ THz (Fig. 5.11 (d)) and with a frequency resolution $df = 14.66$ THz (Fig. 5.11 (f)).

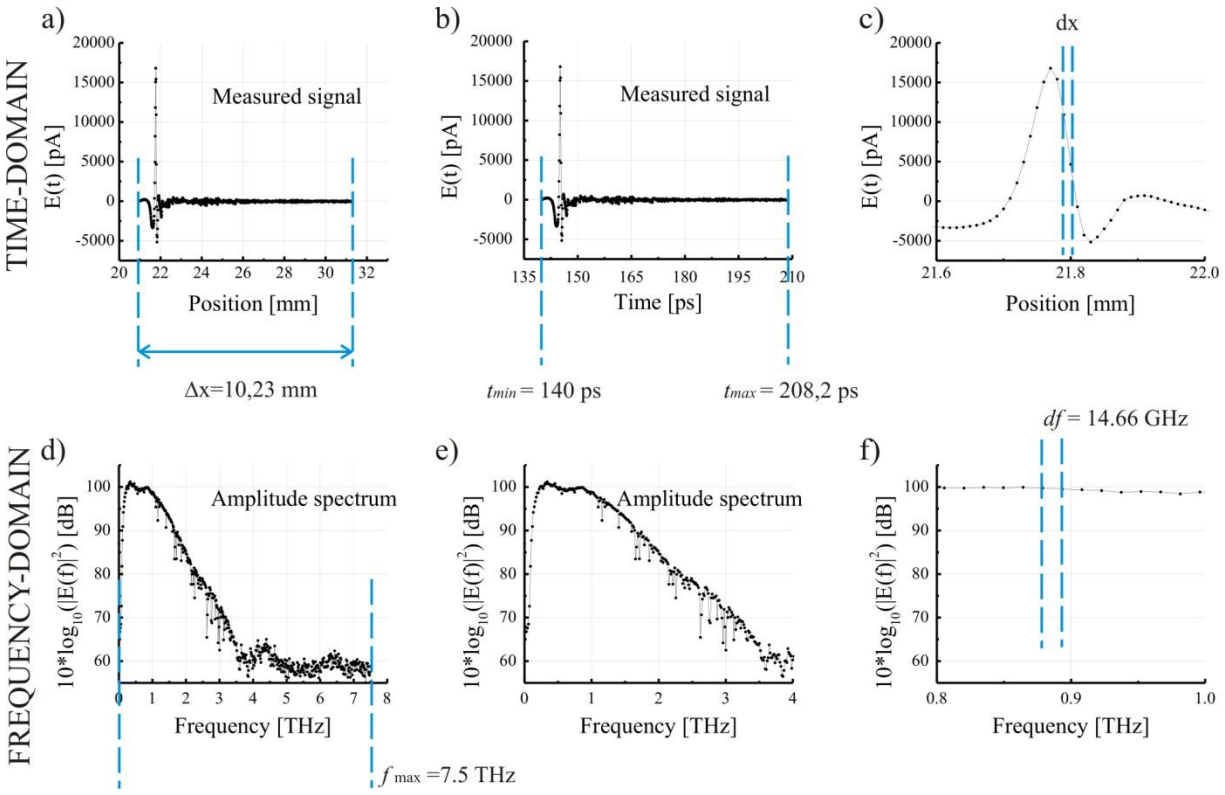

Fig. 5.11 (a) THz electric field $E_{THz}(t)$ as a function of the delay line displacement and (b) associated recalculated time in picoseconds. (c) Zoom-in of the THz electric field $E_{THz}(t)$ measured point-by-point in the time-domain with $N = 1024$ points, $\Delta t = 68.2\ ps$ and $dx = 10\ \mu m$. The Fourier transform of the time signal gives an amplitude $E_{THz}(f)$ with $f_{\max} = 7.5$ THz (d)-(e) and with a frequency resolution $df = 14.66$ THz (Fig. 5.11 (f)).

Thus, for a typical THz spectrum that extends from 0 to 4 THz (shown in Fig. 5.11 (e)), it is required to have Nyquist critical frequency $f_{\max} > 5\,THz$ and scan with the step size $dx < 15\ \mu m$ to avoid spectral artifacts. Furthermore, a frequency resolution of 10 GHz requires a delay line displacement of $\Delta x = 15\ mm$, and a resolution of 1 GHz requires $\Delta x = 15\ cm$.

Ambient humidity

Ambient water vapor has very strong absorption lines at THz frequencies. A detailed list of the frequency positions and strengths of the absorption lines can be found in the literature [31, 137]. In order to illustrate the strong effects of the water vapor absorption, a comparison of the typical spectra from the THz Emitter measured at 12% and 65% of humidity is given in Figure 5.12.

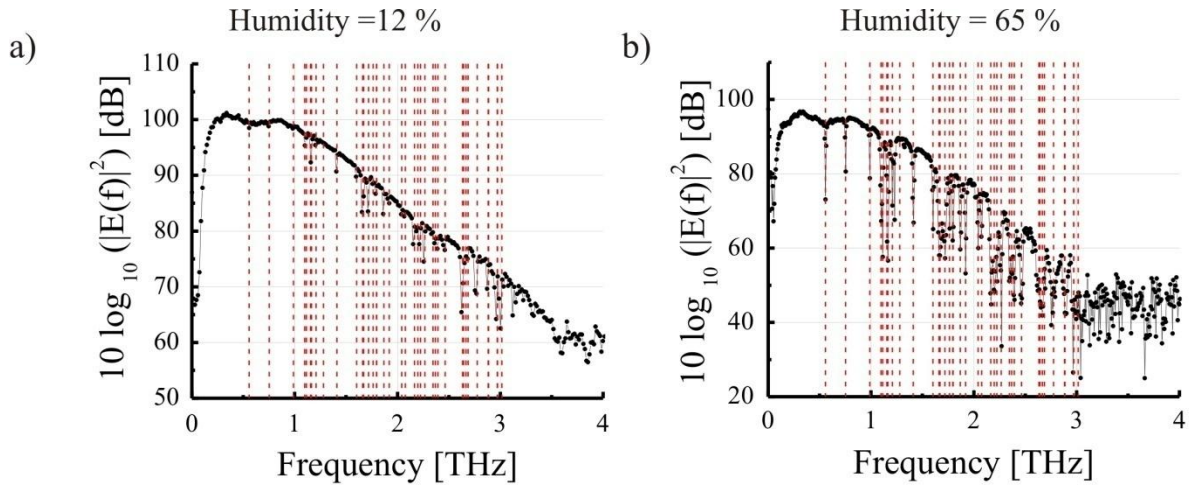

Fig. 5.12. Comparison of the typical spectra from the THz Emitter measured at a) 12% and b) 65% of humidity. Water absorption lines are indicated by red dashed lines in the range of 0–3 THz. At high humidity levels the spectrum is very much altered by absorption lines.

Our THz system is placed within a large nitrogen purged cage to minimize the absorption effects. However it is impossible to completely remove the water vapor in our setup, this is why we can only compare “high” (65–80%) and “low” (5–12%) humidity levels. Positions of water absorption lines are indicated by red dashed lines in the spectra presented in Fig. 5.12. It could be noticed that at high humidity levels the spectrum is very much altered by absorption lines. Thus before each experiment the cage was purged with pure Nitrogen overnight (approximately from 8 to 12 hours) in order to reach 10–12 % of humidity during the summer and 4–5 % during the winter time.

Fiber holders

Another important question that I would like to discuss is the reproducibility of my measurements. It is influenced by many factors, but specific fiber holders used during the experiments are most crucial elements. Ideally, fiber holder should not cause any undesirable perturbations in the initial radiation during the measurements and in the same time allow placing the fiber at the same exact position during each measurement.

Label-free bacteria detection

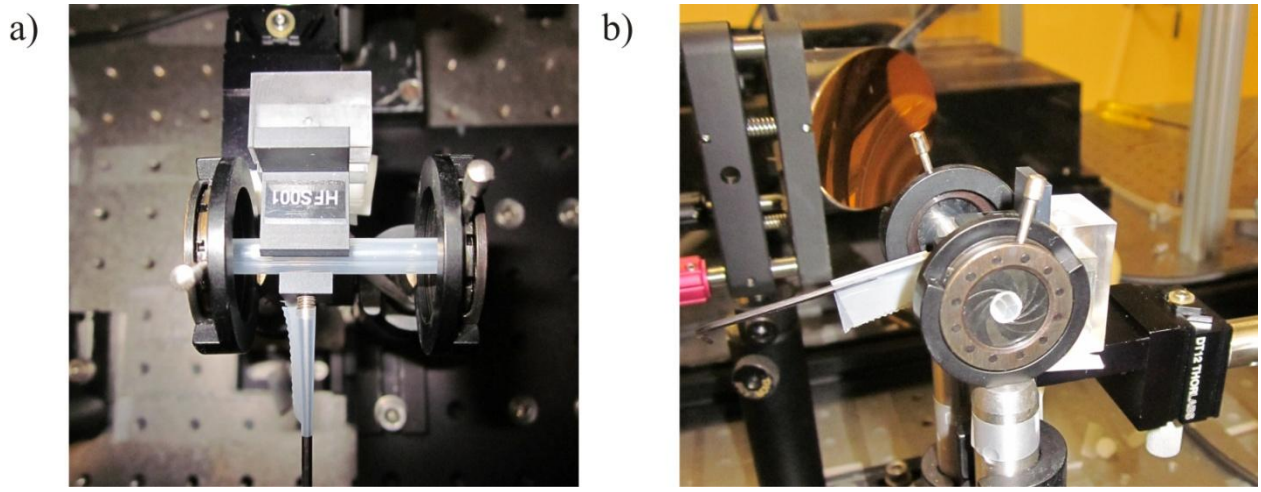

Fig. 5.13. a) a top view and b) front view of the THz fiber, fixed between two irises and placed between the focal points of the two parabolic mirrors for the label free bacteria detection.

We used HFS001 V-groove hexagonal holder for the label-free bacteria detection experiments (see Fig. 5.13 a)). It has a V-shaped groove, which allows us to fix fibers with a typical diameter of 5 mm. The holder itself was fixed on the 3-axis translation stage. Also, in our setup two apertures are placed in the focal points of each parabolic mirror while the fiber is fixed between these two apertures (Fib 5.13 b)). Thus we can ensure consistent alignment during all the experiments. For example, in the case of the *E-coli* bacteria detection measurements the fiber has to be removed after each step of the experiment and then placed back. Our fiber holder and two apertures allow us to put the fiber back exactly at the same position as it was during the previous steps of the experiment.

Another aspect that has to be mentioned regarding the *E-coli* bacteria detection experiments is fiber drying. Earlier it was mentioned that the fiber was dried out for the transmission measurements. We found that the best way to dry the fiber is using a low flow of the compressed air. After the drying surface of the fiber core and bridges was checked under the optical microscope in order to avoid small drops of buffer or distillated water that could remain after the washing.

Chalcogenide glass capillaries

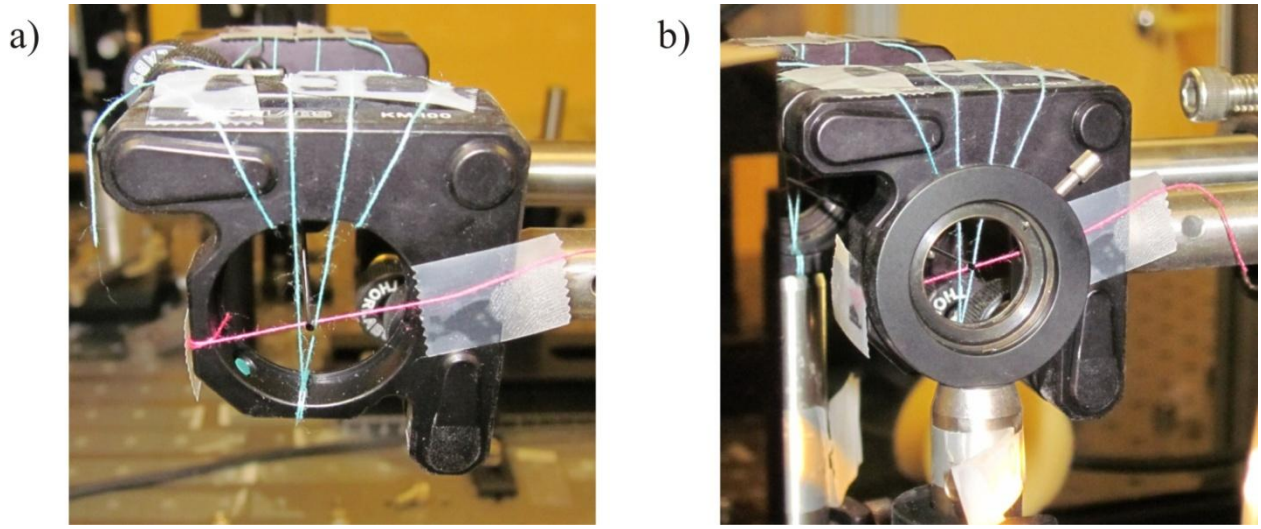

Fig. 5.14. a) Front view of the chalcogenide glass capillary, suspended on the threads fixed over the holder placed on 3-axis translation stage. This kind of holder was used, because thin-walled capillaries are very fragile. b) The capillary was aligned with respect of the two apertures and placed between the focal points of the two parabolic mirrors.

Thin-walled chalcogenide glass capillaries with a wall thickness below 20 μm are very fragile. And we have figured out that the most reliable way is to suspend the capillary on the tiny threads fixed over the holder which is placed on 3-axis translation stage (see Fig 5.14 a)). Then the capillaries were aligned with respect of the two apertures (see Fig. 5.14 b) as discussed above and placed between the focal points of the two parabolic mirrors.

Label-free bacteria detection

Some comments have to be made about the Fig. 4.4 in the Chapter 4. As it was mentioned in Chapter 4, the THz subwavelength waveguide used in our experiments features a 150 μm core fiber suspended by three 20 μm-thick bridges in the center of a 5.1 mm diameter tube. This fiber was made from the low density polyethylene (LDPE) with a typical wall thickness $t_{wall} = 750 \pm 50\,\mu\text{m}$.

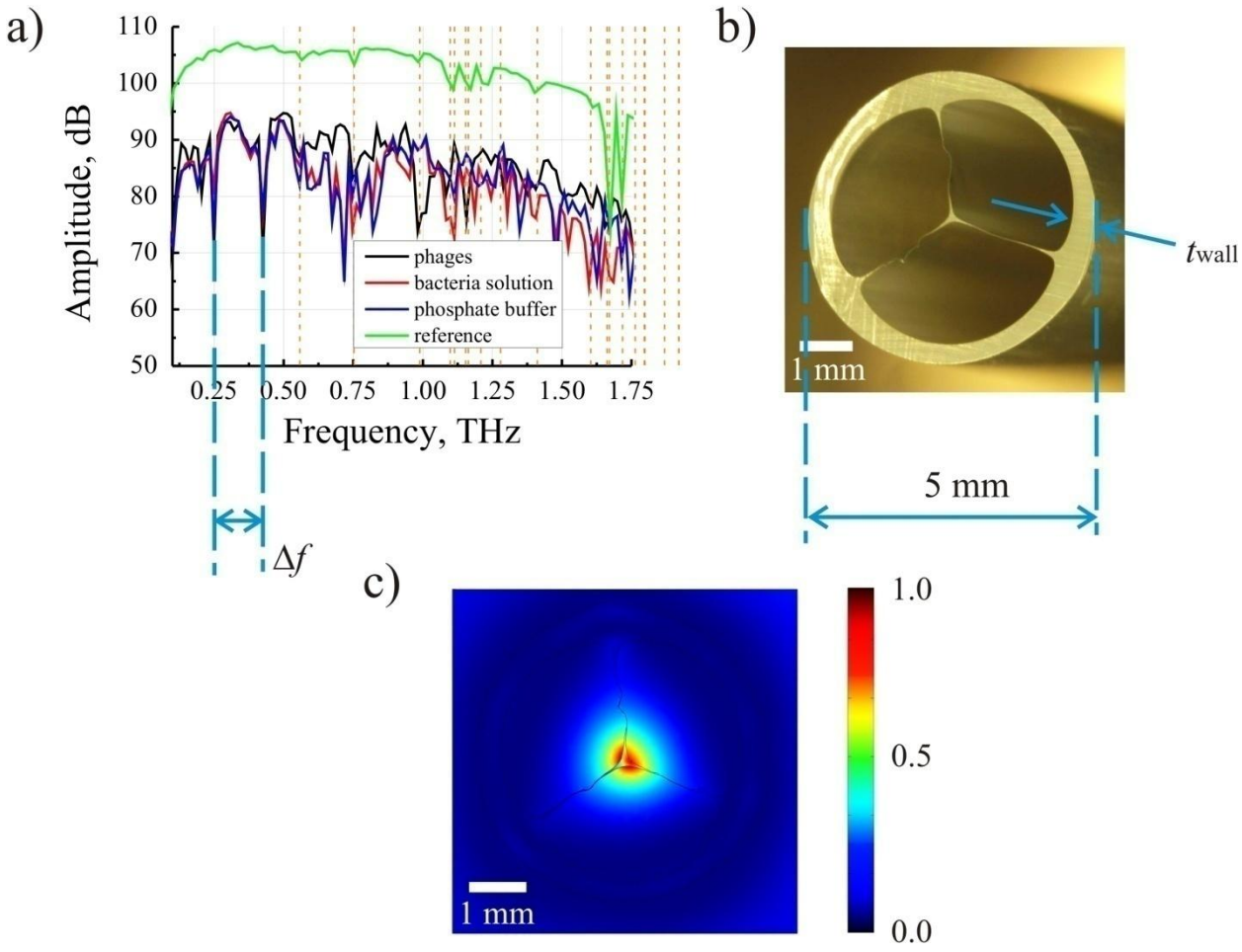

Fig. 5.15. (a) Transmission spectrums of the fiber during each step of the label-free bacteria detection experiment: step 1- black line, only phages, step 2 – red line, transmission of the fiber decreased due binding of E. coli bacteria to the phages, step 3 – blue line, fiber is washed with PBS. Green line –a reference spectrum. Positions of the water absorption lines are indicated by orange dashed lines. (b) The THz subwavelength waveguide used in our experiments features a 150 μm core fiber suspended by three 20 μm-thick bridges in the center of a 5.1 mm diameter tube. (c) Transverse distribution of the power flow of the real waveguide at 0.25 THz.

The THz radiation is focused into the fiber with the parabolic mirror (Fig 4.2 (a)). The focusing of a Gaussian beam leads to a frequency-dependent beam size that is approximately given by: $d_0 = 4 \cdot F \cdot \lambda / (\pi \cdot D)$, where F is the focal distance of the parabolic mirror (4 inch), and D is initial diameter of the Gaussian beam (in our case it equals the aperture size of the parabolic mirror which is 2 inches). Thus, we can estimate, that frequency-dependent beam size at focal point at 1 THz is around 767 μm, while at 0.25 THz the beam size is around 2.56 mm. Due to a large beam size at low frequencies we have coupling not only to the modes of the core, but also to the modes of the waveguide as a whole. Moreover, the coupling efficiency of the initial Gaussian beam into the modes of the tube (the waveguide as a whole) dominates over the coupling into modes of the waveguide, since the wavelength is much higher than the dimensions of the core. The transverse distribution of the power flow of the waveguide at 0.25 THz is shown in Fig. 5.15 (c). For the simulation we have used the structure of the waveguide obtained from its microscopic photo. Fig. 5.15 (c) shows high delocalization of the modal power, the radiation is affected by the presence of the tube's walls and, therefore, the diameter of the waveguide and its walls thickness affect transmission at low frequencies. The guiding mechanism at low frequencies is similar to the ARROW guiding in capillaries. Thus, the dips in the transmission spectra can be explained as antiresonant reflection conditions where the wall of the capillary acts as a Fabry–Perot resonator. Under the antiresonant condition considerable reflections at the inner side of the tube result in the strong light confinement inside this tube (waves bounce back and forth inside of the tube). The guiding mechanism of the pipe waveguides is described in Chapter 5. The resonant frequencies of the tube wall are given by the condition of the constructive interference between the multiple reflections of light between the two refracting surfaces of the wall (Fig. 5. 4 (b)), where n_2 and n_1 denote the refractive indices of plastic (polyethylene) and air, respectively; t_{wall} is the wall thickness of the tube: $f_m = \frac{mc}{2 \cdot t_{wall} \cdot \sqrt{n_2^2 - n_1^2}}$, where c is the speed of light in vacuum, and m is an integer. Typical value for the refractive index of Polyethylene is 1.514, thus resulting in $\Delta f = 0.176\,THz$, which perfectly fits the positions of the two resonances presented in Fig. 5.15.

I would also like to emphasize that all presented graphs are the results of the averaging over 15 spectra measured during each step of the experiment. As it was mentioned before during

each step of the experiment we performed at least 10-15 scans of the transmitted spectrum (one scan takes ~1 min).

Despite the high selectivity and sensitivity of the currently available methods, a number of drawbacks limit their universal application, notably the time duration required to yield a result, which typically varies from days to weeks. These detection methods are designed specifically for laboratory use and cannot be expected to serve in field. Plus, the supporting systems are expensive and require complicated sample processing as well as specialized operator training. This is why major research efforts are currently focused on the development of the efficient and low-cost sensor devices for detection of pathogenic bacteria.

A great number of recent research projects were devoted to the investigation of the use of bacteriophages (phages) as recognition elements. The phages identify their host by specific receptor molecules on the outside of the bacterial cell, infect the host and use it as a factory for their own replication. The advantage of phages is their sensitivity and high specificity to bacteria. Moreover, these small viruses are harmless to humans and animals, are much less expensive and faster to produce than antibodies, and have a much longer shelf life. Phage-based recognition receptors also show very high thermal stability. In the same time a number of optical sensors have been developed for label-free detection of bacteria based on the surface plasmon resonance (SPR) or resonant mirrors (RM) effects. Both these effects offer very high sensitivity to variations in properties of the external medium.

We suggest a first implementation of the label-free *E.coli* bacteria sensor based on the evanescent field of the fundamental mode of the suspended core THz fiber that combines benefits of the phages-based recognition techniques and evanescent field detection methods.

The detection of the bacteria should be specific and selective in order to discriminate the real signals from false-positive signals. This is why after the phage absorption in our experiments the fiber was washed with distillated water and PBS, and then exposed fiber surface was blocked with bovine serum albumin (BSA) for 30 min in order to reduce nonspecific adsorption of the bacteria. The whole detection procedure takes only 40 minutes and does not require complicated sample processing.

Finally, the detection limit of our method is on the order of 10^4 cfu/ml. Strictly speaking, actual detection limit is 10^6 cfu/ml, but significant changes in absorption losses are visible,

starting from 10^4 cfu/ml. However these changes are less or comparable with an inaccuracy of the transmission measurements.

CONCLUSION

In conclusion, I would like to summarize the results and point out the distinctive features of the completed projects, as well as indicate some directions for possible future improvements and research.

THz composite films. In Chapter 3 a novel method for the fabrication of THz metamaterial composite films via fiber drawing and subsequent pressing of the metallic or dielectric microwire arrays into composite films was proposed. Additionally it was shown that fabricated metal wire based metamaterial films appear to have strong polarization properties, while chalcogenide-based metamaterial films produced by the same method obtain designable high refractive index and are polarization insensitive.

As it was already mentioned in the introduction to the Chapter 3, there are two main distinctive features of our metamaterials. First of all, most of the existing experimental studies of the THz wire array materials deal with highly ordered arrays of relatively large diameter wires (hundreds of microns). Such ordered wire array materials could be easily described by existing analytical models. However in our case, due to specifics of the fabrication technique, we create arrays of *parallel, while randomly positioned* microwires of variable from wire to wire diameters on the order of 1-10 microns. Therefore, applicability of formulas developed for the periodic wire arrays to our metamaterials is questionable if at all justified. Instead, to describe our metamaterials one has to use effective random media theories such as Maxwell-Garnett or Bruggeman theories. Moreover, in most experimental work on the wire-array media one typically uses commercial wires made of good metals such copper or gold with dielectric constants that can be well fitted with a Drude model. Due to specifics of the fabrication technique, we can only use *low melting temperature alloys* which are thermo-mechanically compatible with plastics used during fiber drawing. In particular, we use alloys of semi-metals Tin (Sn) and Bismuth (Bi) with dielectric constants that cannot be generally described by a simple Drude model.

The first obvious improvement over the accomplished work would be to use better materials, such as highly conductive metals together with thermally compatible low-loss(at THz frequencies) plastics or glasses. Among potential material choices are cupper/borosilicate glass or even amorphous metal/PSU polymer combinations. Second improvement would be a perfected fabrication technique that would result in highly ordered wire arrays embedded into the fiber host

material. This would result in better comparison with the existing theoretical predictions for the properties of the metal wire arrays, as well as improved polarization performance of the polarisers based on the composite films.

Thus, applying the suggested improvements to the already developed design, cost-effective mass-production of the presented wire-grid polarizers would become possible.

Label-free bacteria detection. To our knowledge, a label-free *E. coli* bacteria sensor based on the evanescent field of the fundamental mode of a suspended-core terahertz fiber is studied for the first time. In the previous sections we were able to show the correlation between the fiber absorption losses and the bacteria concentration of the samples. It was also demonstrated that the detection of limit of our method is on the order of 10^4 cfu/ml, which is comparable with the existing commercially available laboratory-based methods [80]. The commercial methods usually employ antibodies (Abs) as recognition elements instead of bacteriophages. Production of the specific Abs, however, is difficult, expensive and very time-consuming. Also, antibodies easily lose their activity when subjected to changing environmental conditions. Bacteriophages present an alternative method of bacteria capture that offer many advantages compared to antibodies. Particularly, phages are easy to produce in large quantities at a relatively low cost, they have long storage life and unlike antibodies can be physically adsorbed onto the fiber surface.

Considerable sensitivity enhancement of our method is possible by increasing the amount of the initial phage coverage of the fiber surface by better anchoring the phages via covalent immobilization onto the fiber surface, rather than physical adsorption. This, however, implies considerable effort in fiber surface biofunctionalisation chemistry. However, this theme is beyond the scope of the current research but could be an interesting stand-alone interdisciplinary project.

Thin chalcogenide capillaries. Chalcogenide glass $As_{38}Se_{62}$ capillaries were proved to act as efficient waveguides in the whole mid-infrared – terahertz spectral range. As it was mentioned earlier in the Chapter 4, guiding mechanism of the capillary waveguide is well known and is similar to that of the antiresonant optical waveguides (ARROWs), which can be simply described by considering the capillary wall as a Fabry-Pérot etalon. The resonant frequencies of the tube wall are given by the condition of the constructive interference between the multiple reflections of light between the two refracting walls of the capillary. Therefore, it is not surprising that the capillary wall thickness is the most important parameter that controls the fiber

transmission. Observed difference in the measured and theoretical results can be, in principle, explained by the radial and longitudinal non-uniformity of the capillaries, as well as by the lack of detailed knowledge of the chalcogenide glass refractive index in the whole near-IR and mid-IR frequency ranges. Both of these parameters are the key factorsin the equation that defines the positions of minimal and maximal transmittance of the capillary when it guides via anti-resonant mechanism.

Although in our group we are able to fabricate chalcogenide glass capillaries of various sizes, degree of the capillary uniformity still remains an open question. For power transmissionof the mid-IR radiation the uniformity of the capillary wall thickness should be better characterised and controlled. A more uniform capillary thickness could be achieved by perfecting materials and processes, as well as by using various feedback algorithms during capillary drawing.

One very promising application of the discussed capillaries is development of the all-fiber tunable, coherent and narrow-band THz sources based on the effect generation of THz difference frequency radiation by the mixing of two output lines of a CO_2 laser in nonlinear crystals (*e.g.* GaAs, GaSe, $ZnGeP_2$ or $LiNbO_3$) [138, 139]. Our capillaries are proved to act as efficient waveguides in the whole THz to mid-IR spectral range thus it becomes possible both to generate and then guide the THz radiation within one chalcogenide glass capillary.

REFERENCES

[1] H. Tao, W. J. Padilla, X. Zhang, and R. D. Averitt, "Recent Progress in Electromagnetic Metamaterial Devices for Terahertz Applications," *Ieee Journal of Selected Topics in Quantum Electronics,* vol. 17, pp. 92-101, Jan-Feb 2011.

[2] W. Withayachumnankul and D. Abbott, "Metamaterials in the Terahertz Regime," *Ieee Photonics Journal,* vol. 1, pp. 99-118, 2009.

[3] B. Reinhard, O. Paul, and M. Rahm, "Metamaterial-based photonic devices for terahertz technology," *Selected Topics in Quantum Electronics, IEEE Journal of,* vol. PP, pp. 1-1, 2012.

[4] S. Atakaramians, S. Afshar, H. Ebendorff-Heidepriem, M. Nagel, B. M. Fischer, D. Abbott, and T. M. Monro, "THz porous fibers: design, fabrication and experimental characterization," *Optics Express,* vol. 17, pp. 14053-14062, Aug 2009.

[5] A. Hassani, A. Dupuis, and M. Skorobogatiy, "Low loss porous terahertz fibers containing multiple subwavelength holes," *Applied Physics Letters,* vol. 92, Feb 2008.

[6] A. Dupuis, J. F. Allard, D. Morris, K. Stoeffler, C. Dubois, and M. Skorobogatiy, "Fabrication and THz loss measurements of porous subwavelength fibers using a directional coupler method," *Optics Express,* vol. 17, pp. 8012-8028, May 2009.

[7] A. Dupuis, A. Mazhorova, F. Desevedavy, M. Roze, and M. Skorobogatiy, "Spectral characterization of porous dielectric subwavelength THz fibers fabricated using a microstructured molding technique," *Optics Express,* vol. 18, pp. 13813-13828, Jun 2010.

[8] M. Nagel, A. Marchewka, and H. Kurz, "Low-index discontinuity terahertz waveguides," *Optics Express,* vol. 14, pp. 9944-9954, Oct 2006.

[9] M. Roze, B. Ung, A. Mazhorova, M. Walther, and M. Skorobogatiy, "Suspended core subwavelength fibers: towards practical designs for low-loss terahertz guidance," *Optics Express,* vol. 19, pp. 9127-9138, May 2011.

[10] H. O. Moser and C. Rockstuhl, "3D THz metamaterials from micro/nanomanufacturing," *Laser & Photonics Reviews,* vol. 6, pp. 219-244, Mar 2012.

[11] D. M. Wu, N. Fang, C. Sun, X. Zhang, W. J. Padilla, D. N. Basov, D. R. Smith, and S. Schultz, "Terahertz plasmonic high pass filter," *Applied Physics Letters,* vol. 83, pp. 201-203, Jul 2003.

[12] A. Macor, E. de Rijk, S. Alberti, T. Goodman, and J. P. Ansermet, "Note: Three-dimensional stereolithography for millimeter wave and terahertz applications," *Review of Scientific Instruments,* vol. 83, Apr 2012.

[13] G. F. Taylor, "A Method of Drawing Metallic Filaments and a Discussion of their Properties and Uses," *Physical Review,* vol. 23, pp. 655-660, 1924.

[14] V. G. Veselago, "The electrodynamics of substances with simultaneously negative values of and," *Soviet Physics - Uspekhi,* vol. 10, pp. 509-14, 1968.

[15] S. Li, H. W. Zhang, Q. Y. Wen, Y. Q. Song, Y. S. Xie, W. W. Ling, Y. X. Li, and J. Zha, "Micro-fabrication and properties of the meta materials for the terahertz regime," *Infrared Physics & Technology,* vol. 53, pp. 61-64, Jan 2010.

[16] F. Miyamaru, S. Kuboda, K. Taima, K. Takano, M. Hangyo, and M. W. Takeda, "Three-dimensional bulk metamaterials operating in the terahertz range," *Applied Physics Letters,* vol. 96, Feb 2010.

[17] O. Rybin, M. Raza, T. Nawaz, and T. Abbas, "Evaluation of layer properties of effective parameters of metallic rod metamaterials in GHz frequencies," *Aeu-International Journal of Electronics and Communications,* vol. 63, pp. 648-652, 2009.

[18] J. B. Pendry, "Negative refraction makes a perfect lens," *Physical Review Letters,* vol. 85, pp. 3966-3969, Oct 2000.

[19] X. Liu, S. MacNaughton, D. B. Shrekenhamer, H. Tao, S. Selvarasah, A. Totachawattana, R. D. Averitt, M. R. Dokmeci, S. Sonkusale, and W. J. Padilla, "Metamaterials on parylene thin film substrates: Design, fabrication, and characterization at terahertz frequency," *Applied Physics Letters,* vol. 96, Jan 2010.

[20] V. S. W. Cai. (2010). *Optical Metamaterials: Fundamentals and Applications*.

[21] C. Brosseau, "Modelling and simulation of dielectric heterostructures: a physical survey from an historical perspective," *Journal of Physics D-Applied Physics,* vol. 39, pp. 1277-1294, Apr 2006.

[22] J.-h. Peng, J.-j. Yang, M. Huang, J. Sun, and Z.-y. Wu, "Simulation and analysis of the effective permittivity for two-phase composite medium," *Frontiers of Materials Science in China,* vol. 3, pp. 38-43, 2009.

[23] J. Elser, R. Wangberg, V. A. Podolskiy, and E. E. Narimanov, "Nanowire metamaterials with extreme optical anisotropy," *Applied Physics Letters,* vol. 89, Dec 2006.

[24] M. G. Silveirinha, "Nonlocal homogenization model for a periodic array of epsilon-negative rods," *Physical Review E,* vol. 73, Apr 2006.

[25] J. B. Pendry, A. J. Holden, D. J. Robbins, and W. J. Stewart, "Magnetism from conductors and enhanced nonlinear phenomena," *Ieee Transactions on Microwave Theory and Techniques,* vol. 47, pp. 2075-2084, Nov 1999.

[26] H. Xin, R. G. Zhou, and Ieee, "Low-effective index of refraction medium using metallic wire array," in *2007 Ieee Antennas and Propagation Society International Symposium, Vols 1-12,* ed New York: Ieee, 2007, pp. 2323-2326.

[27] S. A. F. M R F Jensen, T Dumelow, T J Parker, Kamsu Abraha, R E Camley, S R P Smith and D R Tilley, "Fourier Transform Spectroscopy of Magnetic Materials at Terahertz Frequencies," *Terahertz Science and Technology,* vol. 2, pp. 105-119, 2009.

[28] D. R. Smith, W. J. Padilla, D. C. Vier, S. C. Nemat-Nasser, and S. Schultz, "Composite medium with simultaneously negative permeability and permittivity," *Physical Review Letters,* vol. 84, pp. 4184-4187, May 2000.

[29] M. Y. Koledintseva, J. Wu, J. Zhang, J. L. Drewniak, and K. N. Rozanov, "Representation of permittivity for multi-phase dielectric mixtures in FDTD modeling," in *Proc. IEEE Symp. Electromag. Compat*, Santa Clara, CA, 2004, pp. 309-314.

[30] M. Scheller, S. Wietzke, C. Jansen, and M. Koch, "Modelling heterogeneous dielectric mixtures in the terahertz regime: a quasi-static effective medium theory," *Journal of Physics D-Applied Physics,* vol. 42, Mar 2009.

[31] M. Y. Koledintseva, J. Drewniak, R. DuBroff, K. Rozanov, and B. Archambeault, "Modeling of shielding composite materials and structures for microwave frequencies," *Progress In Electromagnetics Research B,* pp. 197-215, 2009.

[32] J. B. Pendry, A. J. Holden, W. J. Stewart, and I. Youngs, "Extremely low frequency plasmons in metallic mesostructures," *Physical Review Letters,* vol. 76, pp. 4773-4776, Jun 1996.

[33] S. I. Maslovski, S. A. Tretyakov, and P. A. Belov, "Wire media with negative effective permittivity: A quasi-static model," *Microwave and Optical Technology Letters,* vol. 35, pp. 47-51, Oct 2002.

[34] P. Markos and C. M. Soukoulis, "Absorption losses in periodic arrays of thin metallic wires," *Optics Letters,* vol. 28, pp. 846-848, May 2003.

[35] H. Kong, G. Li, Z. Jin, G. Ma, Z. Zhang, and C. Zhang, "Polarization-independent Metamaterial Absorber for Terahertz Frequency," *Journal of Infrared, Millimeter, and Terahertz Waves,* vol. 33, pp. 649-656, 2012/06/01 2012.

[36] Y. Minowa, T. Fujii, M. Nagai, T. Ochiai, K. Sakoda, K. Hirao, and K. Tanaka, "Evaluation of effective electric permittivity and magnetic permeability in metamaterial slabs by terahertz time-domain spectroscopy," *Optics Express,* vol. 16, pp. 4785-4796, Mar 2008.

[37] K. Takano, T. Kawabata, C. F. Hsieh, K. Akiyama, F. Miyamaru, Y. Abe, Y. Tokuda, R. P. Pan, C. L. Pan, and M. Hangyo, "Fabrication of Terahertz Planar Metamaterials Using a Super-Fine Ink-Jet Printer," *Applied Physics Express,* vol. 3, 2010.

[38] T. Kondo, T. Nagashima, and M. Hangyo, "Fabrication of wire-grid-type polarizers for THz region using a general-purpose color printer," *Japanese Journal of Applied Physics Part 2-Letters,* vol. 42, pp. L373-L375, Apr 2003.

[39] H. T. Chen, W. J. Padilla, J. M. O. Zide, A. C. Gossard, A. J. Taylor, and R. D. Averitt, "Active terahertz metamaterial devices," *Nature,* vol. 444, pp. 597-600, Nov 2006.

[40] K. Takano, H. Yokoyama, A. Ichii, I. Morimoto, and M. Hangyo, "Wire-grid polarizer sheet in the terahertz region fabricated by nanoimprint technology," *Optics Letters,* vol. 36, pp. 2665-2667, Jul 2011.

[41] P. H. Yao, C. J. Chung, C. L. Wu, and C. H. Chen, "Polarized backlight with constrained angular divergence for enhancement of light extraction efficiency from wire grid polarizer," *Optics Express,* vol. 20, pp. 4819-4829, Feb 2012.

[42] I. Yamada, K. Takano, M. Hangyo, M. Saito, and W. Watanabe, "Terahertz wire-grid polarizers with micrometer-pitch Al gratings," *Optics Letters,* vol. 34, pp. 274-276, 2009.

[43] C. F. Hsieh, Y. C. Lai, R. P. Pan, and C. L. Pan, "Polarizing terahertz waves with nematic liquid crystals," *Optics Letters,* vol. 33, pp. 1174-1176, Jun 2008.

[44] C. Imhof and R. Zengerle, "Strong birefringence in left-handed metallic metamaterials," *Optics Communications,* vol. 280, pp. 213-216, Dec 2007.

[45] P. Weis, O. Paul, C. Imhof, R. Beigang, and M. Rahm, "Strongly birefringent metamaterials as negative index terahertz wave plates," *Applied Physics Letters,* vol. 95, Oct 2009.

[46] X. G. Peralta, E. I. Smirnova, A. K. Azad, H. T. Chen, A. J. Taylor, I. Brener, and J. F. O'Hara, "Metamaterials for THz polarimetric devices," *Optics Express,* vol. 17, pp. 773-783, Jan 2009.

[47] A. C. Strikwerda, K. Fan, H. Tao, D. V. Pilon, X. Zhang, and R. D. Averitt, "Comparison of birefringent electric split-ring resonator and meanderline structures as quarter-wave plates at terahertz frequencies," *Optics Express,* vol. 17, pp. 136-149, Jan 2009.

[48] J.-B. Masson and G. Gallot, "Terahertz achromatic quarter-wave plate," *Optics Letters,* vol. 31, pp. 265-267, 2006.

[49] N. Amer, W. C. Hurlbut, B. J. Norton, Y. S. Lee, and T. B. Norris, "Generation of terahertz pulses with arbitrary elliptical polarization," *Applied Physics Letters,* vol. 87, Nov 2005.

[50] N. I. Landy, C. M. Bingham, T. Tyler, N. Jokerst, D. R. Smith, and W. J. Padilla, "Design, theory, and measurement of a polarization-insensitive absorber for terahertz imaging," *Physical Review B,* vol. 79, Mar 2009.

[51] N. I. Landy, S. Sajuyigbe, J. J. Mock, D. R. Smith, and W. J. Padilla, "Perfect metamaterial absorber," *Physical Review Letters,* vol. 100, May 2008.

[52] H. Tao, N. I. Landy, C. M. Bingham, X. Zhang, R. D. Averitt, and W. J. Padilla, "A metamaterial absorber for the terahertz regime: Design, fabrication and characterization," *Optics Express,* vol. 16, pp. 7181-7188, May 2008.

[53] H. Tao, C. M. Bingham, A. C. Strikwerda, D. Pilon, D. Shrekenhamer, N. I. Landy, K. Fan, X. Zhang, W. J. Padilla, and R. D. Averitt, "Highly flexible wide angle of incidence terahertz metamaterial absorber: Design, fabrication, and characterization," *Physical Review B,* vol. 78, Dec 2008.

[54] F. Alves, B. Kearney, D. Grbovic, N. V. Lavrik, and G. Karunasiri, "Strong terahertz absorption using SiO2/Al based metamaterial structures," *Applied Physics Letters,* vol. 100, Mar 2012.

[55] R. Ulrich, "Far-infrared properties of metallic mesh and its complementary structure," *Infrared Physics,* vol. 7, pp. 37-50, 1967.

[56] R. Ulrich, "Interference filters for the far infrared," *Applied Optics,* vol. 7, pp. 1987-96, 1968.

[57] S. Gupta, G. Tuttle, M. Sigalas, and K. M. Ho, "Infrared filters using metallic photonic band gap structures on flexible substrates," *Applied Physics Letters,* vol. 71, pp. 2412-2414, Oct 1997.

[58] C. Winnewisser, F. Lewen, J. Weinzierl, and H. Helm, "Transmission features of frequency-selective components in the far infrared determined by terahertz time-domain spectroscopy," *Applied Optics,* vol. 38, pp. 3961-3967, Jun 1999.

[59] O. Paul, R. Beigang, and M. Rahm, "Highly Selective Terahertz Bandpass Filters Based on Trapped Mode Excitation," *Optics Express,* vol. 17, pp. 18590-18595, Oct 2009.

[60] A. J. Gallant, M. A. Kaliteevski, S. Brand, D. Wood, M. Petty, R. A. Abram, and J. M. Chamberlain, "Terahertz frequency bandpass filters," *Journal of Applied Physics,* vol. 102, Jul 2007.

[61] A. Boltasseva and V. M. Shalaev, "Fabrication of optical negative-index metamaterials: Recent advances and outlook," *Metamaterials,* vol. 2, pp. 1-17, 2008.

[62] X. J. Zhang, Z. Y. Ma, Z. Y. Yuan, and M. Su, "Mass-productions of vertically aligned extremely long metallic micro/nanowires using fiber drawing nanomanufacturing," *Advanced Materials,* vol. 20, pp. 1310-1314, Apr 2008.

[63] A. Tuniz, B. T. Kuhlmey, R. Lwin, A. Wang, J. Anthony, R. Leonhardt, and S. C. Fleming, "Drawn metamaterials with plasmonic response at terahertz frequencies," *Applied Physics Letters,* vol. 96, May 2010.

[64] A. Mazhorova, J. F. Gu, A. Dupuis, M. Peccianti, O. Tsuneyuki, R. Morandotti, H. Minamide, M. Tang, Y. Y. Wang, H. Ito, and M. Skorobogatiy, "Composite THz materials using aligned metallic and semiconductor microwires, experiments and interpretation," *Optics Express,* vol. 18, pp. 24632-24647, Nov 2010.

[65] A. Wang, A. Tuniz, P. G. Hunt, E. M. Pogson, R. A. Lewis, A. Bendavid, S. C. Fleming, B. T. Kuhlmey, and M. C. J. Large, "Fiber metamaterials with negative magnetic permeability in the terahertz," *Optical Materials Express,* vol. 1, pp. 115-120, May 2011.

[66] A. Tuniz, R. Lwin, A. Argyros, S. C. Fleming, E. M. Pogson, E. Constable, R. A. Lewis, and B. T. Kuhlmey, "Stacked-and-drawn metamaterials with magnetic resonances in the terahertz range," *Optics Express,* vol. 19, pp. 16480-16490, Aug 2011.

[67] A. Turner, M. Zourob, and S. Elwary, *Principles of Bacterial Detection: Biosensors, Recognition Receptors and Microsystems*: Springer, 2008.

[68] N. Laman, S. S. Harsha, D. Grischkowsky, and J. S. Melingery, "High-resolution waveguide THz spectroscopy of biological molecules," *Biophysical Journal,* vol. 94, pp. 1010-1020, Feb 2008.

[69] C. Markos, W. Yuan, K. Vlachos, G. E. Town, and O. Bang, "Label-free biosensing with high sensitivity in dual-core microstructured polymer optical fibers," *Optics Express,* vol. 19, pp. 7790-7798, Apr 2011.

[70] J. R. Ott, M. Heuck, C. Agger, P. D. Rasmussen, and O. Bang, "Label-free and selective nonlinear fiber-optical biosensing," *Optics Express,* vol. 16, pp. 20834-20847, Dec 2008.

[71] J. F. O'Hara, R. Singh, I. Brener, E. Smirnova, J. G. Han, A. J. Taylor, and W. L. Zhang, "Thin-film sensing with planar terahertz metamaterials: sensitivity and limitations," *Optics Express,* vol. 16, pp. 1786-1795, Feb 2008.

[72] H. Tao, L. R. Chieffo, M. A. Brenckle, S. M. Siebert, M. K. Liu, A. C. Strikwerda, K. B. Fan, D. L. Kaplan, X. Zhang, R. D. Averitt, and F. C. Omenetto, "Metamaterials on Paper as a Sensing Platform," *Advanced Materials*, vol. 23, pp. 3197-+, Jul 2011.

[73] T. Globus, T. Khromova, D. Woolard, and A. Samuels, "THz resonance spectra of bacillus subtilis cells and spores in PE pellets and dilute water solutions - art. no. 62120K," in *Terahertz for Military and Security Applications IV*. vol. 6212, D. L. Woolard, R. J. Hwu, M. J. Rosker, and J. O. Jensen, Eds., ed Bellingham: Spie-Int Soc Optical Engineering, 2006, pp. K2120-K2120.

[74] A. Bykhovski, L. Xiaowei, T. Globus, T. Khromova, B. Gelmont, D. Woolard, A. C. Samuels, and J. O. Jensen, "THz absorption signature detection of genetic material of E. coli and B. subtilis," in *Chemical and Biological Standoff Detection III, 24 Oct. 2005*, USA, 2005, pp. 59950-1.

[75] M. Theuer, S. S. Harsha, and D. Grischkowsky, "Flare coupled metal parallel-plate waveguides for high resolution terahertz time-domain spectroscopy," *Journal of Applied Physics*, vol. 108, Dec 2010.

[76] M. Walther, M. R. Freeman, and F. A. Hegmann, "Metal-wire terahertz time-domain spectroscopy," *Applied Physics Letters*, vol. 87, Dec 2005.

[77] L. Cheng, S. Hayashi, A. Dobroiu, C. Otani, K. Kawase, T. Miyazawa, and Y. Ogawa, "Terahertz-wave absorption in liquids measured using the evanescent field of a silicon waveguide," *Applied Physics Letters*, vol. 92, May 2008.

[78] B. You, T. A. Liu, J. L. Peng, C. L. Pan, and J. Y. Lu, "A terahertz plastic wire based evanescent field sensor for high sensitivity liquid detection," *Optics Express*, vol. 17, pp. 20675-20683, Nov 2009.

[79] M. N. Velasco-Garcia, "Optical biosensors for probing at the cellular level: A review of recent progress and future prospects," *Seminars in Cell & Developmental Biology*, vol. 20, pp. 27-33, Feb 2009.

[80] S. K. Arya, A. Singh, R. Naidoo, P. Wu, M. T. McDermott, and S. Evoy, "Chemically immobilized T4-bacteriophage for specific Escherichia coli detection using surface plasmon resonance," *Analyst*, vol. 136, pp. 486-492, 2011.

[81] D. Maraldo, P. M. Shankar, and R. Mutharasan, "Measuring bacterial growth by tapered fiber and changes in evanescent field," *Biosensors & Bioelectronics,* vol. 21, pp. 1339-1344, Jan 2006.

[82] A. P. Ferreira, M. M. Werneck, and R. M. Ribeiro, "Development of an evanescent-field fibre optic sensor for Escherichia coli O157 : H7," *Biosensors & Bioelectronics,* vol. 16, pp. 399-408, Aug 2001.

[83] R. Bharadwaj, V. V. R. Sai, K. Thakare, A. Dhawangale, T. Kundu, S. Titus, P. K. Verma, and S. Mukherji, "Evanescent wave absorbance based fiber optic biosensor for label-free detection of E. coli at 280 nm wavelength," *Biosensors & Bioelectronics,* vol. 26, pp. 3367-3370, Mar 2011.

[84] B. Bureau, S. Maurugeon, F. Charpentier, J. L. Adam, C. Boussard-Pledel, and X. H. Zhang, "Chalcogenide Glass Fibers for Infrared Sensing and Space Optics," *Fiber and Integrated Optics,* vol. 28, pp. 65-80, 2009.

[85] H. Jong, M. Rodrigues, S. J. Saggese, and G. H. Sigel, Jr., "Remote fiber-optic chemical sensing using evanescent-wave interactions in chalcogenide glass fibers," *Applied Optics,* vol. 30, pp. 3944-51, 1991.

[86] N. Granzow, S. P. Stark, M. A. Schmidt, A. S. Tverjanovich, L. Wondraczek, and P. S. J. Russell, "Supercontinuum generation in chalcogenide-silica step-index fibers," *Optics Express,* vol. 19, pp. 21003-21010, Oct 2011.

[87] B. Ung and M. Skorobogatiy, "Chalcogenide microporous fibers for linear and nonlinear applications in the mid-infrared," *Optics Express,* vol. 18, pp. 8647-8659, Apr 2010.

[88] N. Ho, M. C. Phillips, H. Qiao, P. J. Allen, K. Krishnaswami, B. J. Riley, T. L. Myers, and N. C. Anheier, "Single-mode low-loss chalcogenide glass waveguides for the mid-infrared," *Optics Letters,* vol. 31, pp. 1860-1862, Jun 2006.

[89] A. F. Kosolapov, A. D. Pryamikov, A. S. Biriukov, V. S. Shiryaev, M. S. Astapovich, G. E. Snopatin, V. G. Plotnichenko, M. F. Churbanov, and E. M. Dianov, "Demonstration of CO2-laser power delivery through chalcogenide-glass fiber with negative-curvature hollow core," *Optics Express,* vol. 19, pp. 25723-25728, Dec 2011.

[90] B. Temelkuran, S. D. Hart, G. Benoit, J. D. Joannopoulos, and Y. Fink, "Wavelength-scalable hollow optical fibres with large photonic bandgaps for CO2 laser transmission," *Nature,* vol. 420, pp. 650-3, 2002.

[91] M. Zalkovskij, C. Z. Bisgaard, A. Novitsky, R. Malureanu, D. Savastru, A. Popescu, P. U. Jepsen, and A. V. Lavrinenko, "Ultrabroadband terahertz spectroscopy of chalcogenide glasses," *Applied Physics Letters,* vol. 100, Jan 2012.

[92] Y. S. Jin, G. J. Kim, and S. G. Jeon, "Terahertz dielectric properties of polymers," *Journal of the Korean Physical Society,* vol. 49, pp. 513-517, Aug 2006.

[93] B. Ung, A. Mazhorova, A. Dupuis, M. Roze, and M. Skorobogatiy, "Polymer microstructured optical fibers for terahertz wave guiding," *Optics Express,* vol. 19, pp. 848-861, Dec 2011.

[94] L. J. Chen, H. W. Chen, T. F. Kao, J. Y. Lu, and C. K. Sun, "Low-loss subwavelength plastic fiber for terahertz waveguiding," *Optics Letters,* vol. 31, pp. 308-310, Feb 2006.

[95] J. A. Harrington, R. George, P. Pedersen, and E. Mueller, "Hollow polycarbonate waveguides with inner Cu coatings for delivery of terahertz radiation," *Optics Express,* vol. 12, pp. 5263-5268, Oct 2004.

[96] B. Bowden, J. A. Harrington, and O. Mitrofanov, "Silver/polystyrene-coated hollow glass waveguides for the transmission of terahertz radiation," *Optics Letters,* vol. 32, pp. 2945-2947, Oct 2007.

[97] T. Ito, Y. Matsuura, M. Miyagi, H. Minarnide, and H. Ito, "Flexible terahertz fiber optics with low bend-induced losses," *Journal of the Optical Society of America B-Optical Physics,* vol. 24, pp. 1230-1235, May 2007.

[98] A. Dupuis, K. Stoeffler, B. Ung, C. Dubois, and M. Skorobogatiy, "Transmission measurements of hollow-core THz Bragg fibers," *Journal of the Optical Society of America B-Optical Physics,* vol. 28, pp. 896-907, Apr 2011.

[99] C. H. Lai, Y. C. Hsueh, H. W. Chen, Y. J. Huang, H. C. Chang, and C. K. Sun, "Low-index terahertz pipe waveguides," *Optics Letters,* vol. 34, pp. 3457-3459, Nov 2009.

[100] C. H. Lai, B. W. You, J. Y. Lu, T. A. Liu, J. L. Peng, C. K. Sun, and H. C. Chang, "Modal characteristics of antiresonant reflecting pipe waveguides for terahertz waveguiding," *Optics Express,* vol. 18, pp. 309-322, Jan 2010.

[101] Y. Matsuura, R. Kasahara, T. Katagiri, and M. Miyagi, "Hollow infrared fibers fabricated by glass-drawing technique," *Optics Express,* vol. 10, pp. 488-492, Jun 2002.

[102] M. Miyagi and S. Nishida, "Transmission characteristics of dielectric tube leaky waveguide," *Ieee Transactions on Microwave Theory and Techniques,* vol. MTT-28, pp. 536-41, 1980.

[103] E. Nguema, D. Ferachou, G. Humbert, J. L. Auguste, and J. M. Blondy, "Broadband terahertz transmission within the air channel of thin-wall pipe," *Optics Letters,* vol. 36, pp. 1782-1784, May 2011.

[104] D. R. Chen and H. B. Chen, "A novel low-loss Terahertz waveguide: Polymer tube," *Optics Express,* vol. 18, pp. 3762-3767, Feb 2010.

[105] T. Kanamori, Y. Terunuma, S. Takahashi, and T. Miyashita, "Chalcogenide glass fibers for mid-infrared transmission," *Journal of Lightwave Technology,* vol. T-2, pp. 607-13, 1984.

[106] M. Naftaly and R. E. Miles, "Terahertz time-domain spectroscopy: A new tool for the study of glasses in the far infrared," *Journal of Non-Crystalline Solids,* vol. 351, pp. 3341-3346, Oct 2005.

[107] M. Skorobogatiy and J. Yang, "Fundamentals of photonic crystal guiding," ed, 2009, p. 267.

[108] M. Born, E. Wolf, and A. B. Bhatia, "Principles of optics :electromagnetic theory of propagation, interference and diffraction of light," ed, 1999, p. 952.

[109] C. C. Katsidis and D. I. Siapkas, "General transfer-matrix method for optical multilayer systems with coherent, partially coherent, and incoherent interference," *Applied Optics,* vol. 41, pp. 3978-3987, Jul 2002.

[110] W. Withayachumnankul, B. M. Fischer, and D. Abbott, "Material thickness optimization for transmission-mode terahertz time-domain spectroscopy," *Optics Express,* vol. 16, pp. 7382-7396, May 2008.

[111] M. Bayindir, E. Cubukcu, I. Bulu, T. Tut, E. Ozbay, and C. M. Soukoulis, "Photonic band gaps, defect characteristics, and waveguiding in two-dimensional disordered dielectric and metallic photonic crystals," *Physical Review B,* vol. 64, Nov 2001.

[112] A. I. Rahachou and I. V. Zozoulenko, "Light propagation in nanorod arrays," *Journal of Optics a-Pure and Applied Optics,* vol. 9, pp. 265-270, Mar 2007.

[113] K. Aydin, K. Guven, N. Katsarakis, C. M. Soukoulis, and E. Ozbay, "Effect of disorder on magnetic resonance band gap of split-ring resonator structures," *Optics Express,* vol. 12, pp. 5896-5901, Nov 2004.

[114] N. Papasimakis, V. A. Fedotov, Y. H. Fu, D. P. Tsai, and N. I. Zheludev, "Coherent and incoherent metamaterials and order-disorder transitions," *Physical Review B,* vol. 80, Jul 2009.

[115] N. V. Smith, "Classical generalization of the Drude formula for the optical conductivity," *Physical Review B,* vol. 64, Oct 2001.

[116] S. H. Chen, C. C. Chen, and C. G. Chao, "Novel morphology and solidification behavior of eutectic bismuth-tin (Bi-Sn) nanowires," *Journal of Alloys and Compounds,* vol. 481, pp. 270-273, Jul 2009.

[117] L. Harris and J. Piper, "Optical and electrical properties of bismuth deposits," *Journal of the Optical Society of America,* vol. 53, pp. 1271-1275, 1963.

[118] W. S. Boyle and A. D. Brailsford, "Far infrared studies of bismuth," *Physical Review,* vol. 120, pp. 1943-1949, 1960.

[119] V. A. Podolskiy, L. V. Alekseyev, and E. E. Narimanov, "Strongly anisotropic media: the THz perspectives of left-handed materials," *Journal of Modern Optics,* vol. 52, pp. 2343-2349, Nov 2005.

[120] A. Hassani, A. Dupuis, and M. Skorobogatiy, "Porous polymer fibers for low-loss terahertz guiding," *Optics Express,* vol. 16, pp. 6340-6351, Apr 2008.

[121] A. Leung, P. M. Shankar, and R. Mutharasan, "A review of fiber-optic biosensors," *Sensors and Actuators B-Chemical*, vol. 125, pp. 688-703, Aug 2007.

[122] J. Q. Zhang and D. Grischkowsky, "Waveguide terahertz time-domain spectroscopy of nanometer water layers," *Optics Letters*, vol. 29, pp. 1617-1619, Jul 2004.

[123] L. Duvillaret, F. Garet, and J. L. Coutaz, "A reliable method for extraction of material parameters in terahertz time-domain spectroscopy," *Ieee Journal of Selected Topics in Quantum Electronics*, vol. 2, pp. 739-746, Sep 1996.

[124] (2004) Textbook of veterinary physiological chemistry. *Scitech Book News*. n/a-n/a. Available: http://search.proquest.com/docview/200033967?accountid=40695

[125] W. Shu, J. Liu, H. Ji, and M. Lu, "Core structure of the outer membrane lipoprotein from Escherichia coli at 1.9 A resolution," *Journal of Molecular Biology*, vol. 299, pp. 1101-1112, Jun 2000.

[126] A. Bykhovski and B. Gelmont, "Influence of Environment on Terahertz Spectra of Biological Molecules," *Journal of Physical Chemistry B*, vol. 114, pp. 12349-12357, Sep 2010.

[127] M. van Exter, C. Fattinger, and D. Grischkowsky, "Terahertz time-domain spectroscopy of water vapor," *Optics Letters*, vol. 14, pp. 1128-30, 1989.

[128] R. A. Cheville and D. Grischkowsky, "Far-infrared foreign and self-broadened rotational linewidths of high-temperature water vapor," *Journal of the Optical Society of America B-Optical Physics*, vol. 16, pp. 317-322, Feb 1999.

[129] J. E. K. Laurens and K. E. Oughstun, *Electromagnetic impulse response of triply-distilled water*. New York: Kluwer Academic/Plenum Publ, 1999.

[130] J. R. Birch, J. D. Dromey, and J. Lesurf, "The optical constants of some common low-loss polymers between 4 and 40 cm-1," *Infrared Physics*, vol. 21, pp. 225-8, 1981.

[131] R. Mossadegh, J. S. Sanghera, D. Schaafsma, B. J. Cole, V. Q. Nguyen, R. E. Miklos, and I. D. Aggarwal, "Fabrication of single-mode chalcogenide optical fiber," *Journal of Lightwave Technology*, vol. 16, pp. 214-17, 1998.

[132] V. S. Shiryaev, J. L. Adam, X. H. Zhang, C. Boussard-Pledel, J. Lucas, and M. F. Churbanov, "Infrared fibers based on Te-As-Se glass system with low optical losses," *Journal of Non-Crystalline Solids*, vol. 336, pp. 113-119, May 2004.

[133] G. E. Snopatin, V. S. Shiryaev, V. G. Plotnichenko, E. M. Dianov, and M. F. Churbanov, "High-purity chalcogenide glasses for fiber optics," *Inorganic Materials*, vol. 45, pp. 1439-1460, Dec 2009.

[134] M. F. Churbanov, G. E. Snopatin, V. S. Shiryaev, V. G. Plotnichenko, and E. M. Dianov, "Recent advances in preparation of high-purity glasses based on arsenic chalcogenides for fiber optics," *Journal of Non-Crystalline Solids*, vol. 357, pp. 2352-2357, Jun 2011.

[135] M. F. Churbanov, V. S. Shiryaev, S. V. Smetanin, V. G. Pimenov, V. G. Plotnichenko, and E. B. Kryukova, *The influence of oxygen, carbon and sulfur impurities on optical transparency of As2Se3 glass*. Pardubice: Univ Pardubice, 2002.

[136] A.-A. S. G. A. S. Amorphous Materials, " (Amorphous Materials Inc., 2009). Available: http://www.amorphousmaterials.com/amtir2.htm

[137] M. Vanexter, C. Fattinger, and D. Grischkowsky, "TERAHERTZ TIME-DOMAIN SPECTROSCOPY OF WATER-VAPOR," *Optics Letters*, vol. 14, pp. 1128-1130, Oct 1989.

[138] S. Y. Tochitsky, C. Sung, S. E. Trubnick, C. Joshi, and K. L. Vodopyanov, "High-power tunable, 0.5-3 THz radiation source based on nonlinear difference frequency mixing of CO2 laserlines," *Journal of the Optical Society of America B-Optical Physics*, vol. 24, pp. 2509-2516, Sep 2007.

[139] Y. Z. Lu, X. B. Wang, L. A. Miao, D. L. Zuo, and Z. H. Cheng, "Terahertz Generation in Nonlinear Crystals with Mid-Infrared CO2 Laser," *Chinese Physics Letters*, vol. 28, Mar 2011.